FINAL REPORT

Demonstration of Tungsten Nanocomposite Alternatives to Depleted Uranium in Anti-Armor Penetrators

ESTCP Project WP-200805

NOVEMBER 2014

Lee Magness
Brian Schuster
U.S Army Research Laboratory

Scott Weil
Curt Lavender
Battelle, Pacific Northwest National Laboratory

Distribution Statement A

This document has been cleared for public release

This report was prepared under contract to the Department of Defense Strategic Environmental Research and Development Program (SERDP). The publication of this report does not indicate endorsement by the Department of Defense, nor should the contents be construed as reflecting the official policy or position of the Department of Defense. Reference herein to any specific commercial product, process, or service by trade name, trademark, manufacturer, or otherwise, does not necessarily constitute or imply its endorsement, recommendation, or favoring by the Department of Defense.

REPORT DOCUMENTATION PAGE

Form Approved
OMB No. 0704-0188

Public reporting burden for this collection of information is estimated to average 1 hour per response, including the time for reviewing instructions, searching existing data sources, gathering and maintaining the data needed, and completing and reviewing this collection of information. Send comments regarding this burden estimate or any other aspect of this collection of information, including suggestions for reducing this burden to Department of Defense, Washington Headquarters Services, Directorate for Information Operations and Reports (0704-0188), 1215 Jefferson Davis Highway, Suite 1204, Arlington, VA 22202-4302. Respondents should be aware that notwithstanding any other provision of law, no person shall be subject to any penalty for failing to comply with a collection of information if it does not display a currently valid OMB control number. **PLEASE DO NOT RETURN YOUR FORM TO THE ABOVE ADDRESS.**

1. REPORT DATE *(DD-MM-YYYY)*
02-06-2014

2. REPORT TYPE
Final

3. DATES COVERED *(From - To)*
July 2008 to June 2014

4. TITLE AND SUBTITLE

Tungsten Nanocomposite Alternatives to Depleted Uranium in Anti-Armor Penetrators

5a. CONTRACT NUMBER

5b. GRANT NUMBER

5c. PROGRAM ELEMENT NUMBER

5d. PROJECT NUMBER
ESTCP WP-0805

5e. TASK NUMBER

5f. WORK UNIT NUMBER

6. AUTHOR(S)

Magness, Lee S, Jr. / Schuster, Brian (ARL)

Weil, Scott / Lavender, Curt (BPNW)

7. PERFORMING ORGANIZATION NAME(S) AND ADDRESS(ES)

Army Research Laboratory
Aberdeen Proving Ground
Aberdeen, MD 21005-5066

Battelle, Pacific Northwest National
Richland, WA 99352

8. PERFORMING ORGANIZATION REPORT NUMBER
Tracking # T14-311

9. SPONSORING / MONITORING AGENCY NAME(S) AND ADDRESS(ES)

Environmental Technology Security Certification Program

10. SPONSOR/MONITOR'S ACRONYM(S)

ESTCP

11. SPONSOR/MONITOR'S REPORT NUMBER(S)

12. DISTRIBUTION / AVAILABILITY STATEMENT

UNCLASSIFIED/UNLIMITED DISTRIBUTION
''Approved for public release; distribution is unlimited''

13. SUPPLEMENTARY NOTES

14. ABSTRACT

This ESTCP project sought to develop a nanocrystalline high density material would exhibit the shear failure and "self-sharpening" behavior of depleted uranium (DU), and demonstrate it as a viable replacement for the DU alloy penetrator core materials in kinetic energy projectiles. The project's approach was to attempt to develop nanocrystalline tungsten and tungsten composites of non-hazardous, environmentally-friendly elements, using synthesis processes to produce nanocrystalline powders. The powders were consolidated using solid state processes, such as solid state sintering or hot isostatic pressing. Two primary synthesis processes were studied initially in this ESTCP project, a freeze-dry process and a glycine nitrate process. The glycine nitrate process was eventually downselected based on its ability to produce cleaner powders with finer crystallites (approximately 30 nm). The remainder of the project was dedicated to developing consolidation methods that would achieve full theoretical density, without excessive growth of grain size. However, no process solution for meeting these dual (and competing) goals was ever achieved. One candidate material was produced in stock large enough to conduct a very limited quarter-scale test. While its performance was significantly better than the same material with a conventional grain size, it was well short of being viable as a material to replace DU. Consolidation processes which can achieve densities approaching theoretical full density, but which do not lead to excessive grain growth, are needed.

15. SUBJECT TERM
Tungsten composites, glycine nitrate combustion synthesis, ballistic impact, adiabatic shear

16. SECURITY CLASSIFICATION OF:			**17. LIMITATION OF ABSTRACT**	**18. NUMBER OF PAGES**	**19a. NAME OF RESPONSIBLE PERSON**
a. REPORT	**b. ABSTRACT**	**c. THIS PAGE**			**19b. TELEPHONE NUMBER** *(include area code)*
UL	U	U	U	73	

1 INTRODUCTION 10
1.1 BACKGROUND 10
1.2 OBJECTIVE OF THE DEMONSTRATION 13
1.3 REGULATORY DRIVERS 15

2 TECHNOLOGY 15
2.1 TECHNOLOGY DESCRIPTION 15
2.2 TECHNOLOGY DEVELOPMENT 21
2.3 ADVANTAGES AND LIMITATIONS OF THE TECHNOLOGY 25

3 PERFORMANCE OBJECTIVES 27

4 SITES/PLATFORM DESCRIPTION 29
4.1 TEST PLATFORMS/FACILITY 29
4.2 SITE-RELATED PERMITS AND REGULATIONS 29

5 TEST DESIGN 30
5.1 CONCEPTUAL EXPERIMENTAL DESIGN 30
5.1.1 SMALL CALIBER BALLISTIC SCREENING TESTS 32
5.1.2 ¼-SCALE BALLISTIC TESTS TO DETERMINE LIMIT VELOCITY 34
5.1.3 CORROSION TESTS 38
5.2 FIELD TESTING 39
5.3 MEASUREMENT/MONITORING PLAN 39
5.3.1 MEASUREMENT PLAN FOR BALLISTIC TESTING 39
5.3.2 MEASUREMENT PLAN FOR TOXICITY TESTING 39
5.4 LABORATORY MATERIAL TESTING 40

6 PERFORMANCE ASSESSMENT 40
6.1 CONSOLIDATION OF NANOCRYSTALLINE W-BASED MATERIALS 40
6.2 BALLISTIC TEST RESULTS 58
6.3 CORROSION TEST RESULTS 63
6.3.1 CORROSION TESTS 63
6.3.2 RESULTS AND DISCUSSION 64
6.3.3 CORROSION- SUMMARY AND CONCLUSIONS 69

7 COST ASSESSMENT 69

8 IMPLEMENTATION ISSUES 70

9 REFERENCES 71

10 APPENDICES 74
A. POINTS OF CONTACT 74

LIST OF TABLES

Table 1. Performance Objectives. 13
Table 2. Performance Objectives and Results. 27
Table 3. Demonstration Testing- Experimental Design of Ballistic Tests. 32
Table 4. Green and sintered* densities of compacts prepared using F-D and GNP powders. 41
Table 5. Results of powder reduction experiments. 43
Table 6. Partial set of characterization results for GNP and F-D tungsten alloy or composite powders…… 44
Table 7. Densities of W-based powder compacts before and after dilatometry testing. 50
Table 8. ¼-Scale Test Results 59
Table 9. 7.62mm Tests against 50.8mm Mild Steel 62
Table 10. Bulk and matrix compositions for all alloy formulations considered in this study. 64
Table 11. Cost Model for 1 Kilogram Penetrator Blanks. 70

LIST OF FIGURES

Figure 1. 30mm GAU-8 Round. (DU penetrator core encased in a full-bore aluminum alloy body with windscreen attachment). 14
Figure 2. Project Steps and Decision Points, for the proposed program on tungsten nanocomposite KE penetrator demonstration. 17
Figure 3. Schematic of the basic steps involved in the GNP approach[18]. 18
Figure 4. Flow diagrams for (a) the freeze drying and (b) glycine nitrate methods of synthesizing precursor powder used in nanocrystalline tungsten.**Error! Bookmark not defined.**
Figure 5. Example of high purity W powder prepared by reducing the GNP precursor in dry H2 at 650ºC for 4hrs. Note that most of the individual crystallites that make up this ~600nm long agglomerated powder particle are less than 50nm in size. 21
Figure 6. Cross-sectional micrograph of 90W-7Ni-3Fe, produced by sintering PNNL freeze-dried powders at 1200°C for 4hrs. 24
Figure 7. Limit Velocity versus Alloy Density (for L/D= 15 quarter-scale penetrators [65g]). .31
Figure 8. Small Caliber Test Projectile for Sub-Size Specimens. 33
Figure 9. Deformation and Failure Behavior of (a) Unalloyed Wrought Tungsten, (b) Conventional Tungsten Heavy Alloy, and (c) Uranium-3/4% Titanium Alloy.....34
Figure 10. A sample laboratory launch package, note this example is for a threaded penetrator rod and a smooth right circular cylinder rod will be used in these tests. 35
Figure 11. A Schematic of the Experimental Facility, with Smoothbore Gun Location, and Multiple Orthogonal Flash Radiographs to Record Test Data.....36
Figure 12. A Sample of the Pre-impact Radiographic Images. 36
Figure 13. A sample of the behind armor radiographic images. 37
Figure 14. Sample Limit Velocity Determination. 38
Figure 15. Sintered compacts prepared from (a) F-D W-7Fe-3Ni and (b) GNP W-only powders. Sintering was conducted by heating the green compacts in H2 at 2°C/min to 1000°C, holding at this soak temperature for 2hrs, and cooling at 2°C/min to room temperature. 42
Figure 16. Dilatometry results on a F-D W-1% Y_2O_3 powder prepared by reducing in H_2 at 650°C. 44
Figure 17. Measurements of as-pressed (green) densities as a function of compaction pressure and powder/die lubricant. Lube 1 = 0.5 wt% naphthalene added directly to the powder, Lube 2 = 0.5 wt% stearic acid added directly to the powder. The die lubricant employed was 5% solution of stearic acid dissolved in propanol. 47
Figure 18. Dilatometry results on a baseline pure-W nanocrystalline powder and three series of modified nano-W powders.....48
Figure 19. TEM images of a GNP-derived 0.3wt% Y_2O_3-W powder. The diffraction pattern shown is of the Y_2O_3 matrix seen in the second, bright field and third, dark field images. 49
Figure 20. Dilatometry results on a baseline pure-W nanocrystalline powder and three series of modified nano-W powders.....50
Figure 21. Cross-sectional scanning electron microscope images of: (a) 100% W, (b) W-0.05% Ni, (c) W-0.5% Ni, and (d) W-3% Ni. All specimens densified during dilatometry testing under flowing Ar-2.75% H_2 and a heating rate of 2°C/min. Each sample reached a final temperature of 1400°C. 51

Figure 22. Scanning electron microscope images of the fracture surfaces of: (a) and (b) a 100% W sintered specimen prepared from unmilled GNP powder and (c) and (d) a 100% W sintered specimen prepared from milled (de-agglomerated) GNP powder. Both specimens were sintered under the same conditions at 1400°C for 2hrs in flowing Ar-2.75% H_2. 52
Figure 23. Polished cross-sectional scanning electron microscope image of the specimen in Figures 22(c) and (d). The specimen was prepared by sintering de-agglomerated GNP W powder at 1400°C for 2hrs in flowing Ar-2.75% H_2. 53
Figure 24. As-HIPed cans GNP W-5Re-0.5Ni (top) and ARL-milled GNP 90-7Ni-3Fe (bottom) at 900°C (left) and 850°C (right). 54
Figure 25. The as-HIPed un-etched microstructure of the ARL-milled GNP 90W-7Ni-3Fe powder HIPed at 850°C (a) and 900°C (b), indicating the increased porosity observed with HIPing at 850°C. 55
Figure 26. As-etched micrographs of the ARL-milled GNP 90W-7Ni-3Fe powder HIPed at 850°C (a) and 900°C (b). The microstructure appears to have retained the morphology the milled powder and little difference in feature size is observed. 55
Figure 27. The as-HIPed un-etched microstructure of the HIPed W-5Re-0.5Ni GNP at 850°C (a) and 900°C (b), indicating the increased porosity observed with HIPing at 850°C. 56
Figure 28. As-etched micrographs of the ARL-milled GNP W-5Re-0.5Ni powder HIPed at 850°C (a) and 900°C (b). 56
Figure 29. Microstructure of the GNP-processed W-5Re alloys, ARL-milled and consolidated. 57
Figure 30. Flight X-ray Images (side view), showing the orientation of penetrator in the vertical plane (pitch) prior to target impact. 58
Figure 31. Flight X-ray Images (overhead view), showing the orientation of penetrator in the lateral plane (yaw) prior to target impact. 59
Figure 32. Sectioned RHA Plate, Shot 5072 60
Figure 33. Limit Velocity as a function of alloy density for 65g, L/D = 10 rods against the 76.2mm RHA Plate. 61
Figure 34. 7.62mm Tests (5.6mm dia. x 13.1mm long cylinders) vs. Mild Steel. 62
Figure 35. SEM micrograph of the typical two phase microstructure found in WHAs. The alloys were prepared to yield samples that were roughly 85% by volume of W (lighter phase). The bulk and matrix compositions (darker phase) for this study are listed in Table 10. 63
Figure 36. SEM micrographs of samples after immersion in phosphate buffered saline for 30 days. 65
Figure 37. Summary of ICP-OES measurements of concentrations of metals dissolved in PBS for (a) W-2Ni-1Co, (b) W-Ni-Fe alloys and (c) W-Ni-Fe-Co alloys. (d) and (e) compare W and Ni concentrations for all alloys in this study. 67
Figure 38. The relative composition of metals, (a) in solution measured for days 21-27 shown in weight %, the surface compositions of corroded samples measured by XPS expressed in atomic %. 67

LIST OF ACRONYMS

AFFRI - Armed Forces Radiobiology Research Institute
AGG - Accelerated Grain Growth
AMT- - Ammonium Metatungstate
APFSDS – Armor-Piercing Fin-Stabilized Discarding Sabot
ARDEC – Army Research, Development, and Engineering Center
ARL – Army Research Laboratory
ASB – Adiabatic Shear Band
BHN – Brinell Hardness Number
CHPPM - U.S. Army Center for Health. Promotion and Preventive Medicine
DSC – Differential Scanning Calorimetry
DU – Depleted Uranium
ERDC - Engineer Research and Development Center
GNP- Glycine Nitrate Process
GTP – Global Tungsten Products, Inc.
HIP – Hot Isostatic Pressing
KE – Kinetic Energy
NIST - National Institute for Standards and Testing
OSD - Office of the Secretary of Defense
PBS – Phosphate Buffered Saline
PM-MAS – Program Manager – Maneuver Armament Systems
PNNL – Pacific Northwest National Laboratory
PPC – Plasma Pressure Consolidation
RHA – Rolled Homogeneous Armor
SECNA – Secretary of the Navy
SHB – Split Hopkinson Bar
SPD – Severe Plastic Deformation
SSS - Solid State Sintering
TGA – Thermogravimetric Analysis
V_L – Limit Velocity
V_R – Residual Velocity
V_S – Striking Velocity
WHA – Tungsten Heavy Alloy
XRD – X-Ray Diffraction

ACKNOWLEDGMENTS

The authors wish to acknowledge the contributions of Mr. Brady Butler, ARL, in processing (de-agglomerating) several batches of GNP-produced alloy powders, and for sintering studies with several batches of the Battelle powders and Mr. Cyle Teal, ARL, for his assistance in the final editing of this document. The authors also wish to acknowledge the Environmental Security Technology Certification Program (ESTCP) Office for funding this research into tungsten-based alternatives to depleted uranium for penetrator applications.

EXECUTIVE SUMMARY

Depleted uranium (DU) alloys are utilized in many of the DoD's highest performance kinetic energy projectiles. DU offers significant advantages in terms of the ability to defeat more heavily armored targets and at greater ranges because its superior penetration performance linked to DU's susceptibility to shear failure and resulting "self-sharpening" penetration behavior. However, concerns about environmental and occupational hazards with DU, as well political issues associated with the use of DU on the battlefield, have prompted a long running interest in alternatives to DU. Conventional tungsten heavy alloys are the current alternative materials for this application, but concerns about the toxicity of nickel and cobalt components in these composites have recently been raised as well.

This ESTCP project sought to show that a nanocrystalline high density material would exhibit the shear failure and "self-sharpening" behavior of DU, and demonstrate that it was viable as a replacement for the DU alloy penetrator core materials in kinetic energy projectiles. The project's approach was to attempt to develop nanocrystalline tungsten and tungsten composites of non-hazardous, environmentally-friendly elements, using synthesis processes to produce nanocrystalline powders. The powders would then be consolidated using solid state processes, such as solid state sintering or hot isostatic pressing.

At the start of this project, the efficacy of high density nanocrystalline materials to develop the desired shear behavior had not yet been demonstrated, but the approach was being pursued in other programs using a differing processing, such as mechanical alloying or ball milling to produce nanocrystalline powders, followed by a similar solid state consolidation process. Synthesis processes offered a number of potential advantages over the milling approaches, in terms of producing more intimate intermixing of the tungsten and alloying additions, as well as likely being lower cost and more easily scalable to large scale production.

Two primary synthesis processes were studied initially in this ESTCP project, a freeze-dry process and a glycine nitrate process. The glycine nitrate process was eventually downselected based on its ability to produce cleaner powders with finer crystallites (approximately 30 nm). Meanwhile, about midway through the ESTCP project, the competing milling approach achieved the breakthrough of demonstrating that the shear failure and "self-sharpening" behavior could be developed in a nanocrystalline W composite. This outcome was seen as an encouraging development for the ESTCP project as it independently validated the project's basic nanocrystalline approach. The remainder of the project was dedicated to trying to develop consolidation methods that would achieve full theoretical density, without excessive growth of grain size. A variety of solid state consolidation techniques were applied, ranging from solid state sintering (temperature without pressure) to hot isostatic pressing (a combination of temperature and pressure applied to the metal powders encapsulated in an evacuated metal can). The variables of temperature, time and pressure were studied, using dilatometry to monitor consolidation, and metallographic examinations to measure grain size. Based on data in the literature regarding iron and other metal powders, as well as the later results for the milled tungsten composites mentioned above, the target grain size was 200 nanometers or below at full theoretical density. However, no process solution for meeting these dual (and competing) goals was ever achieved, despite the extensive studies of sintering and hot isostatic pressing processes, and with the application of a variety of sintering aids, grain boundary pinner additions, etc.

It is still believed that if consolidation routes to full theoretical density without excessive growth of grain size can be developed for the synthesis process-manufactured powders, these materials would be lower cost and more easily scaled into production. Unfortunately, no such consolidation process was discovered during the project. One candidate material was produced in stock large enough to conduct a very limited quarter-scale test. While its performance was significantly better than the same material with a conventional grain size, it still fell well short of being viable as a material to replace depleted uranium. Consolidation processes by which one can achieve densities approaching theoretical full density, but which do not lead to excessive grain growth, are needed.

An extensive literature survey and additional studies were conducted to examine toxicological effects of current tungsten heavy alloys, as well as tungsten-based materials that were candidates for nanocrystalline processing. The dramatic differences in the toxicological effects found for 97W-2Ni-1Fe and 91W-6Ni-3Co are explained by stark differences in the corrosion behavior of these metals. In both WHA materials, the preferential anodic dissolution of the binder phase is found. For 91W-6Ni-3Co, the *in-vivo* corrosion process is unimpeded and rats are exposed to ever increasing concentrations of W, Ni (a known carcinogen) and Co (a suspected carcinogen). For the 97W-2Ni-1Fe is associated with formation of a passive iron-oxide that effectively halts operation of the galvanic corrosion cell and dramatically limits the bioavailability of Ni. Similarly, limited corrosion was found for in-vivo implants of unalloyed tungsten, with no ill effects. These insights guided alloy selections for the nanocrystalline process development.

Several useful techniques and processes were developed as part of the ESTCP project. The GNP process developed during this project was matured as a method to reliably produce clean, very fine grain (less than 30 nm grain size) tungsten powders, which may have ballistic as well as other applications. An improved screening method examining the corrosion behavior of candidate W nanocomposites in a simulated physiological solution (and applicable to other materials) was developed to evaluate whether they are likely to have significant environmental or toxicity issues. In addition, a small caliber test was developed as a preliminary ballistic screening method for candidate materials. This test subjects a candidate material to the loading conditions it would experience in a real world ballistic application, conditions of high rate deformation under simultaneous high hydrostatic pressures. The small caliber test allows one to assess whether the candidate material exhibits the shear localization and “self-sharpening” behavior with just a small sample, to determine whether the expense and difficulty of producing larger scale samples should be pursued. This test was quite successful, readily distinguishing between shearing DU alloys and non-shearing conventional tungsten heavy alloys.

1 INTRODUCTION

1.1 BACKGROUND

Depleted uranium (DU) alloys offer several advantages as kinetic energy (KE) penetrator materials when compared to alloys or composites of the only other commercially viable high density materials, tungsten alloys and composites. DU delivers improved penetration performance, defeating armored targets at approximately 20% lower impact energies than other comparable non-DU projectiles. In addition, DU's pyrophoricity produces burning fragments upon impact with the target that can ignite flammable materials and cause secondary damage. However its deployment on the battlefield in the 1991 Gulf War and subsequently in the 1999 Kosovo Conflict has lead to increasing concerns from veterans, the public, and the international community about the environmental and health impacts of the material. While combat assessment studies conducted by the DoD and by non-DoD government agencies in the 1970s and 1980s concluded that the use of DU poses little additional short-term risk compared to the other dangers of combat, the political and post-combat environmental costs remain potentially very high. In addition, since these early studies there has been a lack of agreement among these and other institutions on how to assess the epidemiological risks attributable to DU's toxicity and radiological effects. As a result of these environmental and political concerns, several decisions have been made internally to the DoD, limiting the future development and deployment of DU-based munitions. In weapons systems of medium calibers (up to 60mm) and below, no future DU projectiles are being considered. This decision will typically result in a reduction of more than a kilometer in a medium caliber weapon's effective range if the DU material is replaced with the only currently available material with comparable density and mechanical properties, tungsten heavy alloys (WHAs). In large caliber weapon systems, e. g. tank cannons, the loss of performance associated with a switch away from DU is even more significant, a decrease in effective range in excess of two kilometers. The use of DU in large caliber projectiles was originally targeted to end in 2014 with the production of the latest 120mm tank round despite concerns about the loss of performance. However, the timing of this transition point was recently moved to 2019.

Due to these concerns, there has been continued interest in developing alternative high-density materials, particularly in light of recent advances in nanomaterials and metallurgical processing technology. In the DoD's 1992 road mapping study on a long-term strategy for KE penetrators, various candidate KE materials were compared with respect to four broad categories of merit: performance, supporting industrial manufacturing base, environmental and health factors, and life cycle costs. Numerous DoD reviews and road-mapping studies (1-3) conducted over the years on long-term strategies for KE penetrators have reached the same conclusion: only WHA and tungsten-based composites are viable alternatives to DU; displaying the required densities, availability, and acceptable cost. WHAs are actually tungsten particle-reinforced composites that are liquid-phase sintered using a small amount of nickel, cobalt, iron, and/or other matrix alloy components. These tungsten heavy alloys are commercially-available and widely employed in many modern medium and large caliber KE penetrators produced by foreign manufacturers, such as the German DM-43 and DM-53 rounds, and as well as in projectiles for select U.S. weapon systems (e.g. the 25mm M791 APDS ammunition among others). However due to their inferior penetration performance relative to DU, WHA projectiles require higher

impact velocity to achieve the same penetration depth for an equivalent mass and geometry, which can exceed the gun's and cartridge firing capability. Whereas a DU penetrator self-sharpens as it travels through armor, through a deformation process known as adiabatic shearing, conventional WHA penetrators tend to blunt on impact, forming a mushroom shaped head that inhibits penetration (4).

The current varieties of conventional WHA materials are not without environmental issues of their own. As part of the development of new munitions, the DoD conducts periodic reviews of any potential operational health risks and there have also been some recent concerns raised about the toxicity of WHAs. Historically, toxicology of tungsten has received far less attention than DU, but the prevailing opinion is that elemental tungsten or insoluble tungsten compounds are non-toxic (5). Recently, researchers at the Armed Forces Radiobiology Research Institute (AFRRI) demonstrated that implantation of weapons grade tungsten-nickel-cobalt (W-Ni-Co) into rats resulted in rhabdomyosarcomas (6). In a follow-on study, Roszell and co-workers confirmed tumor formation in rats implanted with this same tungsten-nickel-cobalt alloy, however, rats implanted with pure tungsten or with tungsten-nickel-iron (W-Ni-Fe) showed no overt adverse effects (7). Schuster and co-workers have demonstrated that this stark difference in the health effects of tungsten and WHAs is a strong function of their corrosion behavior (8, 9). Corrosion of tungsten-nickel-cobalt in rat muscle tissue is associated with massive dissolution of the nickel and cobalt rich matrix phase. In contrast, corrosion of tungsten-nickel-iron is associated with the formation of an iron-rich oxide that prevents further dissolution. As a result, rats implanted with tungsten-nickel-cobalt are exposed to ever increasing concentrations of tungsten, nickel and cobalt that eventually result in rhabdomyosarcomas (6, 7). Rats implanted with tungsten-nickel-iron pellets are effectively exposed to considerably lower concentrations of the alloy constituents and therefore no tumors or serious health effects are found (7).

Recent studies by Peuster et al. on tungsten metal coils implanted in the subclavian arteries of rabbits demonstrated elevated serum tungsten levels, but no signs of local or systemic toxicity after 4 months of exposure (10). Similarly, clinical follow-up studies on human patients implanted with tungsten coils to occlude unwanted vascular connections showed no evidence of systemic toxicity or significant local toxicity, although a local inflammatory response was observed in subsequent histopathological evaluations (10-12). Recent acceptance of a tungsten-iron-nickel-tin alloy (65W-10.4Fe-2.8Ni-21.8Sn) by the U.S. Department of the Interior for use as non-toxic shot in waterfowl hunting was based on oral dosage studies of the shot in mallard ducks. Ingestion of up to 1.2g of material did not cause any pathological effects over the 30 day exposure period (13, 14). Investigations on tungsten-bismuth-tin shot conducted by surgically implanting the material in the pectoralis muscle of mallards produced no local or systemic effects over an eight week period of study (15).

Unfortunately, though all conventional WHAs lack the "self-sharpening," adiabatic shear mechanism of DU alloys, the engineering properties, the combinations of strength, ductility, and toughness, of W-Ni-Co and tungsten-nickel-iron-cobalt (W-Ni-Fe-Co) WHAs are better overall than the W-Ni-Fe composites. These better properties permit the design of more efficient launch packages, the penetrator and the sabot which supports it in-bore, to better withstand the accelerations during launch from a cannon. As a result, the highest performance KE projectiles produced recently have utilized W-Ni-Co or W-Ni-Fe-Co WHAs. Eliminating the use of cobalt

and nickel as matrix components, or eliminating cobalt and reducing the dissolution of nickel in the matrix into the blood and tissues was also a goal of this project.

The ultimate goal of this work was to demonstrate that a nanocrystalline tungsten-based penetrator material could deliver penetration performance similar to that of DU alloys (which conventional WHAs do not), using a commercially viable synthesis route to produce the nanocrystalline powders, and also while eliminating the hazardous material issues noted for the conventional nickel-cobalt and nickel-iron-cobalt matrix WHAs. The basic approach taken in this demonstration was to develop nanocrystalline tungsten-based composites. Conventional WHAs are produced via liquid-phase sintering (LPS) of blended metal powders of tungsten, nickel and iron and or cobalt. No matter the starting powder size or grain size within the powders, the LPS process results in multiple micron or tens or microns grain sizes in the fully-dense sintered product. These larger grain size materials do not exhibit the plastic instability and localization behavior of DU alloys, but instead remain plastically stable, developing large mushroomed heads on WHA penetrators during the penetration process (4). While many metals and alloys are plastically stable in forms with conventional grain sizes, nanocrystalline-structured versions of these same metals and alloy systems often exhibit the plastic instability and localization behavior (16). It was believed that if a similar change in behavior could be developed in a nanocrystalline tungsten-based material that this would lead to the desired shear banding and self-sharpeneing behavior displayed by DU alloys.

More details on the basis for the pursuit of a nanocrystalline material will be given in Sections 2.1 and 2.2. The materials and processing technologies to produce nanocrystalline composites and alloys that were pursued in this demonstration here were low-cost nanocrystalline powder syntheses process and consolidation methods to produce tungsten nanocomposites retaining the crystallite size, phase dispersion, in the final consolidated penetrator material. In a powder synthesis process, pre-alloyed metal powders with nanocrystalline grains are produced via dissolution of metal salts in a solution, the solvent is then removed from spray droplets and the metals reduced to produce the pre-mixed, nanograin size powders. Both a freeze-drying and a glycine-nitrate process (GNP) synthesis route were explored. Ultimately the GNP process was chosen for this project. The GNP process starts with an aqueous metal nitrate-glycine solution. The solution dried by heating and eventually autoignites in a self-sustaining combustion reaction that produces the final powder product in a matter of a few seconds. The resulting GNP powder is an intimate and uniform mixture of sub-micron reinforcement and matrix particles that then can be consolidated, by hot isostatic pressing (HIP) or solid state sintering (SSS), to produce a final product which is hopefully fully dense and retains a nanocrystalline microstructure.

An alternative route to produce a bulk nanocrystalline WHA or W product is via mechanical alloying or milling of conventional grain size metal powders to produce nanocrystalline agglomerated powders, followed by solid state sintering (SSS) or Hot Isostatic Pressing (HIP) of the powders into a consolidated product. At the time of the submission of this ESTCP proposal, and during the first half of this ESTCP project, WHA composites and unalloyed W samples made by this alternative approach had not been successful. A powder synthesis route offered a potential method of producing a more intimate mix of the alloying elements in the nanocrystalline powders, which could aid in the consolidation of the final product. The mechanical alloying approach was also more expensive than the synthesis route of this ESTCP

project and would be more difficult to scale up to produce large quantities of the ball-milled or milled powders.

However, a major breakthrough via this competing mechanical alloying approach occurred midway through this ESTCP project, when a nanocrystalline W-based material produced in this manner succeeded in delivering DU-like penetration performance. Details of the process to produce the nanocrystalline metal powders and to consolidate the powders while retaining the desired microstructure and mechanical behavior are classified. This result was actually encouraging for the ESTCP project, since the efficacy of the basic nanocrystalline W-based approach had now been confirmed. Furthermore, the scale up and cost issues associated with the competing mechanical alloying approach still remained, and the powder synthesis route being pursued here offered a potentially lower cost method of producing the nanocrystalline powders.

1.2 OBJECTIVE OF THE DEMONSTRATION

As outlined in Table 1, the ultimate goals of this work were to demonstrate that a nanocrystalline tungsten-based penetrator material, one that removes the hazardous material issues noted above for both DU alloys and the current conventional nickel-cobalt and nickel-iron-cobalt matrix WHAs, can replace DU (which conventional WHAs cannot). Successful demonstration of a tungsten nanocomposite penetrator material would improve the performance of tungsten projectiles against armored targets and allow the DoD to replace DU anti-armor munitions with a non-toxic penetrator material. Successful deployment of tungsten nanocomposite munitions will facilitate the decommissioning of the DU production base over the next decade, realizing a conservative 40-to-60 percent life-cycle cost savings for DoD operation of the anti-armor munitions production base, as well as eliminate the political, economic, environmental, and health issues inherent with the use of DU materials.

Table 1. Performance Objectives.

Performance Objective	Data Requirements	Success Criteria
Quantitative Performance Objectives		
Ballistic Performance in 1/4 –Scale Testing - Penetration efficiency	• Limit Velocity determination • Test vs. MIL-SPEC armor steel • Customized tests	Improved performance of a tungsten-based projectile versus a conventional WHA of comparable density
Environmental and Health	• Examination of the long term corrosion behavior • ASTM F2129 • Immersion Experiments	Materials that utilize only non-toxic or non-hazardous constituents or that form a passive oxide that prevent massive dissolution and degradation of toxic constituents into the body

The materials and processing technologies needed to produce tungsten nanocomposite anti-armor penetrators were to be developed in a pilot scale, with the superior penetration performance of the materials demonstrated in sub-scale (nominally ¼-scale) ballistic tests.

The alloying components selected would minimize or eliminate long term environmental and health concerns associated with its use, avoiding compositions that are known to be carcinogenic (e.g. tungsten-nickel-cobalt). In conjunction with the material development work, we conducted preliminary risk assessments consistent with the “tiered approach” outlined by Kane and coworkers (17). Although none of these materials produced during the ESTCP project were

successful enough in the ¼-scale ballistic evaluation, preliminary risk assessments had also been planned, to measure the metal aerosol concentrations during the ballistic impacts of these alloys.

The manufacture of the material itself would be demonstrated via a high-volume, low-cost approach (i.e. technology transfer-ready) of synthesizing and safely consolidating tungsten nanocomposite powders to maximum overall density and will demonstrate the efficacy of these materials as potential replacements for depleted uranium (DU) in anti-armor penetrators. The project had been coordinated with Global Tungsten Products (GTP, formerly OSRAM Sylvania, a leading producer of tungsten-based projectiles, to assure rapid deployment of the technology into the existing production base.)

The potential applications of this nanocrystalline tungsten-based material include alternative projectile cores for several DU-based weapon systems, including the Air Force 30mm GAU-8 (or PGU-14) round fired by the A-10 aircraft, the 25mm PGU-20 round under development for the Joint Strike Fighter, or as long rod projectiles (also known as Armor-Piercing, Fin-Stabilized, Discarding Sabot (APFSDS) rounds) for the next-generation of medium caliber cannon weapon systems and future 120mm tank cannon kinetic energy projectiles (M829E4 or M829E5).

The scope of possible applications of the "self-sharpening" nanocrystalline tungsten-based material ultimately depends upon the engineering properties, yield strength, elongation, and toughness, obtained in the material. Low strength, ductility, and toughness materials can be incorporated into projectiles with fully-encased armor piercing core designs, such as the 30mm GAU-8 (PGU-14) ammunition for the A10 Tank Killer (see Figure **1**), or the 25mm PGU-20 ammunition for the Joint Strike Fighter. Higher strength, ductility, and toughness materials, however, are necessary for APFSDS or "long rod" ammunition. The long rod penetrator cores are subjected to high tensile and compressive loads during their launch from high-velocity gun systems. Examples include the M919 rounds fired from the 25mm Bradley gun system or M829A1, A2, and A3 rounds fired from 120mm tank guns.

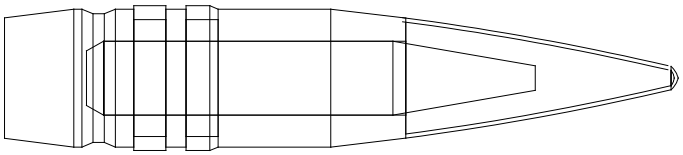

Figure 1. 30mm GAU-8 Round. (DU penetrator core encased in a full-bore aluminum alloy body with windscreen attachment).

The Program Manager- Maneuver Armament Systems (PM-MAS), in Picatinny Arsenal, New Jersey, is responsible for the production and fielding of all direct-fire weapon systems, including small arms, and medium through large caliber (tank gun-fired) munitions, for the Army and the other services, and have encouraged the development of DU alternatives, as well as cobalt-free WHA alternatives.

The Army Research, Development, and Engineering Center (ARDEC), also located at Picatinny Arsenal, (POC: Mr. Gary Fleming) has been intimately involved in the development of the testing and acceptance requirements in many government in-house mission and

Congressionally-directed efforts, including one with GTP, to develop alternative high-density materials for penetrator applications. Those same testing methods and acceptance requirements developed by ARL and ARDEC were also applied here, in coordination with ARDEC. As in the prior programs, ¼-scale ballistic tests were used to rank the performance of these candidate penetrator materials. Correlations have been established between the results of these laboratory ballistic tests and the performance of materials in various fielded systems.

The alternative materials being developed in the ARL and ARDEC programs, including one developed as part of the ARDEC-GTP Congressional Program, are currently being evaluated for the next generation of tank cannon weapons in testing for PM-MAS. ARDEC and PM-MAS are aware of the technology being developed in this ESTCP project and the materials being developed here were also candidates for these tank cannon systems. GTP was involved in the development of the ARDEC-GTP material being evaluated in the PM-MAS testing program and in this ESTCP project (primarily through providing clean metal powder stock).

1.3 REGULATORY DRIVERS

The need for alternative materials to replace DU in kinetic energy penetrator applications is prompted by several DoD decisions and guidelines. As mentioned earlier, the sustainability of the DU production base is in question, as stated in a letter, 19 April 2007, on the Bridging Strategy for Depleted Uranium Industrial Base and Heavy-Armor Defeat Capability, from the DA, Deputy Chief of Staff, emphasizing the urgency of demonstrating a commercially-viable, non-toxic anti-armor penetrator alternate to DU.

Tungsten heavy alloys are used as an alternative to DU in many current penetrator applications, though often a poorer performer than DU. Many of these systems employ tungsten-nickel-cobalt or tungsten-nickel-iron-cobalt WHAs, however the aforementioned studies of the carcinogenic potential of these WHAs has prompted the conduct of follow-up studies on the near- and long-term effects of all metal fragments retained in tissue injuries. The Office of the Secretary of Defense (OSD)/ Acquisition, Technology, and Logistics (ATL), OSD/Health Affairs, and the Secretary of the Navy (SECNA) have all released memos on tungsten alloy health effects. This includes a letter from the Under Secretary of Defense/(ATL), dated 1 Nov 2007, stating that “In light of our present knowledge of the potential health risks associated with tungsten/nickel/cobalt alloys, please have your acquisition managers and munitions developers and researchers consider alternative materials in developmental munitions programs.” Again, the tungsten nanocomposite systems recommended below for ballistic demonstration would not include cobalt as an alloying element.

2 TECHNOLOGY

2.1 TECHNOLOGY DESCRIPTION

This project sought to demonstrate that an environmentally and toxicologically acceptable nanocrystalline tungsten or tungsten-based composite of a useful density (approximately 17.0g/cc or greater) could be produced via synthesis processing routes, and that the material would exhibit the plastic instability and localization behavior, and also the penetration performance, of comparable DU alloys. Ultimately, although the efficacy of the nanocrystalline

approach to changing the behavior and improving the performance of W-based materials was later demonstrated in another program using a competing processing method, the production of a successful nanocrystalline W-based material via synthesis routes was not achieved in this project.

The overall framework of the project is shown in Figure **2**.

The basic goal was to significantly increase the material's strength and reduce its strain hardening and strain rate sensitivity through grain size refinement, and thus to drive shear localization mechanisms during high rate deformation of the material. Projectiles of this high-density material should then exhibit a "self-sharpening" shear failure behavior during ballistic impacts and performance similar to that of DU projectiles when penetrating armor (see Section 2.2 below for more detail). This project examined two different nano-size powder synthesis approaches as shown in Figure **2**). Both had been developed in prior work at Pacific Northwest National Laboratory (PNNL) for other metals and alloys, and have demonstrated scalability of both at the pilot-scale range (100 – 10,000 kg). Methods to consolidate these nano-powders to full density, while retaining the desired nano-structure and plastically unstable deformation behavior, were to be developed as part of this project. The ballistic performances of these materials were then to be demonstrated in ballistic testing using ¼-scale penetrator rods. Originally, initial evaluations of the dynamic mechanical behavior of small samples of candidate materials were to occur in split Hopkinson bar (SHB) compression tests. However, a more reliable testing method using of small caliber projectiles was developed during the project and was to be applied instead as a ballistic screening. The final demonstration of the desired final product was to be its performance in "quarter-scale" ballistic tests. The chemistry of the candidate alloys studied in this project were evaluated against the findings of current toxicology studies, including examinations of the behavior of the candidate materials in simulated biological fluid.

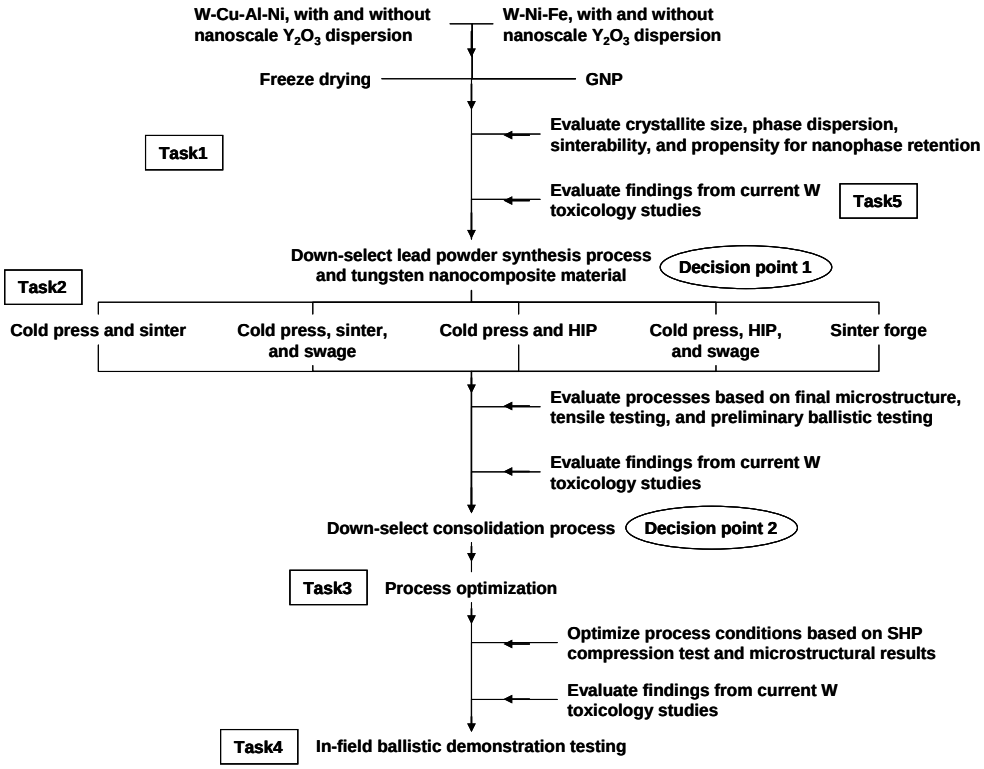

Figure 2. Project Steps and Decision Points, for the proposed program on tungsten nanocomposite KE penetrator demonstration.

The first of these two alternate nano-size powder synthesis approaches evaluated in this project was flash freeze-drying. This process produces an extremely fine, homogeneous powder, via the sublimation of water from a frozen mixture of dissolved precursor salts. The resulting material is calcined (producing NOx, which is recovered and re-used) to liberate various non-metal ligand species (e.g. nitrate groups, chelating agents, and/or ammonia complexes) and reduced to form a fine metal powder.

The second technique evaluated in this project, the glycine nitrate process (GNP), was developed to synthesize nanoscale composite and multi-component materials used at elevated temperatures (18). The GNP approach consists of the formation of an aqueous metal nitrate-glycine solution that is subsequently heated to dryness and eventual autoignition, at which point a self-sustaining combustion reaction takes place producing the final powder product in a matter of a few seconds (see Figure **3**).

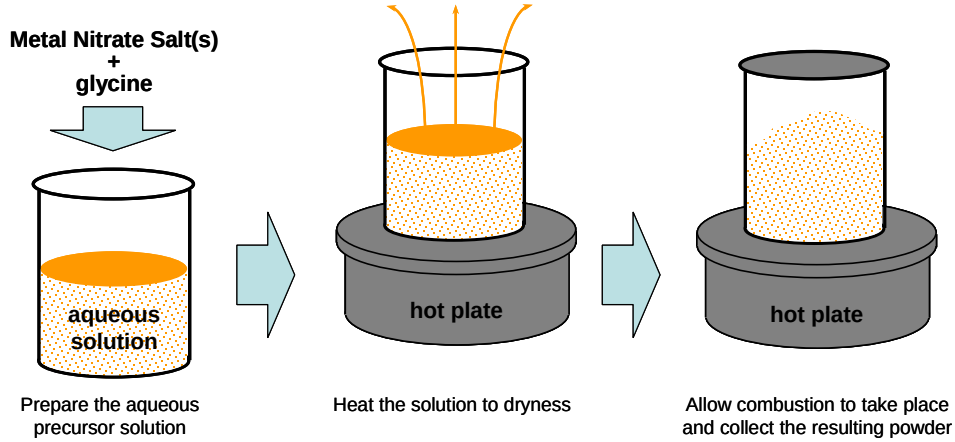

Figure 3. Schematic of the basic steps involved in the GNP approach[18].

In this process, the glycine serves two purposes: (1) it prevents precipitation of the metal salts as the water is evaporated, thereby ensuring that the metal ions remain molecularly mixed in solution up to the point of combustion or chemical conversion, and (2) it acts as the fuel for the combustion reaction by undergoing oxidation with the nitrate ions during heating. The resulting GNP powder is an intimate and uniform mixture of sub-micron reinforcement and matrix particles that subsequently can be consolidated into the final component.

The flash freeze-drying process is outlined in more detail in a flowchart in Figure 4(a). Extremely fine, homogeneous powders were produced via the sublimation of water from a frozen mixture of dissolved precursor salts (ammonium metatungstate [AMT] and metal nitrates). The resulting material was calcined and subsequently reduced to form the final nanograin powder. Solution freeze-point analysis was used to identify a suitable temperature range for droplet freezing (for AMT-only and AMT-Fe/Ni nitrate solutions) and subsequent drying by sublimation; namely < -30°C. Thermogravimetric analysis and differential scanning calorimetry (TGA/DSC) were used to identify an appropriate calcination temperature (found to be > 450°C) to form a phase pure oxide precursor for reduction. Subsequent X-ray diffraction (XRD) measurements indicated that the average crystallite size of the oxide is on the order of 20 - 30 nm when calcination is carried out at the minimum temperature. Hydrogen reduction of the oxide powder was initially conducted at 750°C, producing an agglomerated phase pure metal powder with an average constituent grain size of 50 – 60nm.The steps of the glycine nitrate process (GNP) are shown in the flowchart in final composition of the powder.

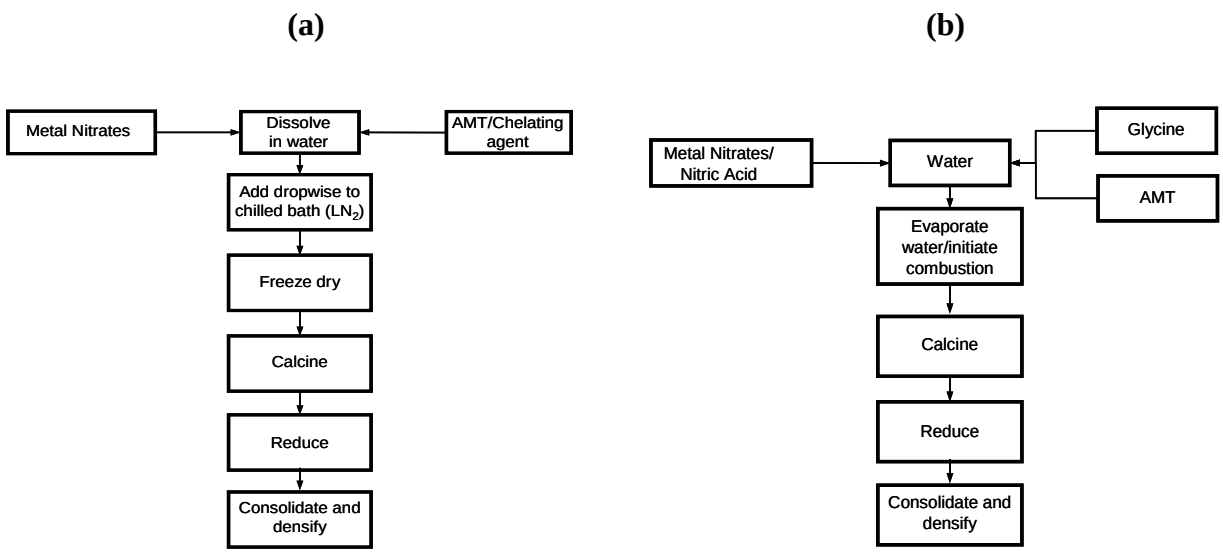

Figure 4. Flow diagrams for (a) the freeze drying and (b) glycine nitrate methods of synthesizing precursor powder used in nanocrystalline tungsten.

(b). After combustion formation, the precursor powder is directly reduced in hydrogen gas to form an agglomerated reduced metal powder with an average crystallite size of ~ 30 -35 nm in size.

In both freeze drying and GNP, once the metal powder is formed, it would be subsequently compacted by isostatic pressing and sintered, hot pressed, or hot isostatically pressed at temperatures ranging from 1000 - 1600°C, depending on the synthesis process employed and the final composition of the powder.

Thus both methods of synthesizing nanocrystalline tungsten-based powder for use in developing a high-performance tungsten-based anti-armor penetrator, the flash freeze-drying process and the glycine nitrate process (GNP), were demonstrated in this project. In the 2nd quarter of FY09, GNP was down-selected as the lead process for synthesizing material used in the next phases of work on this project, namely developing an appropriate method of powder consolidation and conducting mechanical and ballistic testing on the resulting compacts. The process was chosen for three reasons: (1) it employs fewer processing steps, (2) it consistently converts completely from the oxide state to the metal state during low-temperature reduction (by comparison under the same reducing conditions, the freeze-dried material often yields a mixture of oxide and metal powders, the ratio which appears to be sensitive to batch size and H_2 flow rate), and (3) the average crystallite size of the metal powder produced is generally smaller than that obtained by the freeze-drying process, which increases the likelihood that the desired tungsten penetrator microstructure (i.e. high density and nanosize grain structure) can be achieved.

The conditions needed to best consolidate the GNP-produced powder, into a high density, nanograin body for the penetrator core material, were studied for the duration of the project, but ultimately no satisfactory process was developed. Initial consolidation work indicated that only 70 – 80% of theoretical density could be achieved with high-purity tungsten GNP powder via a simple press (uniaxial compaction) and sinter process (pre-sinter density: ~50% of theoretical; sinter conditions: heat at 2ºC/min in dry H_2 to 1000ºC, hold at 1000ºC for 2hrs, and cool to room temperature at 2ºC/min). However it was noted that the average grain size of this version of sintered GNP tungsten is ~300nm, suggesting that, with process optimization, further refinement of the microstructure and improvement in the properties could be achieved. A number of possible processing options to try to increase material density without inducing a concurrent increase in grain size, were explored including:

(1) Promoting increased green density of the original powder compact (which was ~50% of theoretical density) by several approaches: (a) incorporating a powder and/or die lubricant to reduce sources of friction that tend to inhibit powder particle sliding and high powder packing densities, (b) employing higher compaction pressure either during initial uniaxial compaction or during a subsequent cold or hot isostatic compaction step to reduce the size of intraparticle pores, and (c) utilizing shearing forces during compaction to cause particle rearrangement and higher powder packing to take place.

(2) Identifying alternative sintering conditions – higher sintered densities can often be achieved by: (a) increasing the time and temperature at which sintering takes place, (b) increasing the rate of heating to avoid pre-sinter "deadening" of the material, (c) modifying the gas atmosphere (e.g. PO_2) under which sintering occurs, and (d) actively compressing the powder compact during heat treatment via hot pressing or hot isostatic pressing. The key is to avoid accelerated grain growth (AGG), a phenomenon that often accommodates increased sintering activity in nanocrystalline materials and leads to a non-nanograin microstructure in the final as-sintered body.

(3) Incorporating sintering aids – controlled additions of certain elements, element combinations, and/or compounds can enhance the mechanisms responsible for tungsten sintering and thereby promote increased material density. Categories of sintering aids include: (a) those that increase the rate of solid-state tungsten diffusion (e.g. Co, Fe, and Ni), (b) those that form a liquid phase that may or may not enhance tungsten diffusion, but through capillary force cause the constituent particles in the compact to draw together and thereby form a high density body, (c) those that induce a reaction with the tungsten (or with the surface oxide on individual particles), and (d) those that minimize excessive grain boundary motion and therefore AGG during sintering.

(4) Further reducing crystallite and/or agglomerate size. As shown in Figure **5**, the GNP synthesized tungsten powders consist of micron and sub-micron size agglomerates that in turn are made up of nanosize crystallites (or grains). The individual crystallite size depends on a number of factors, but in the GNP process one of the most important is the temperature at which reduction takes place.

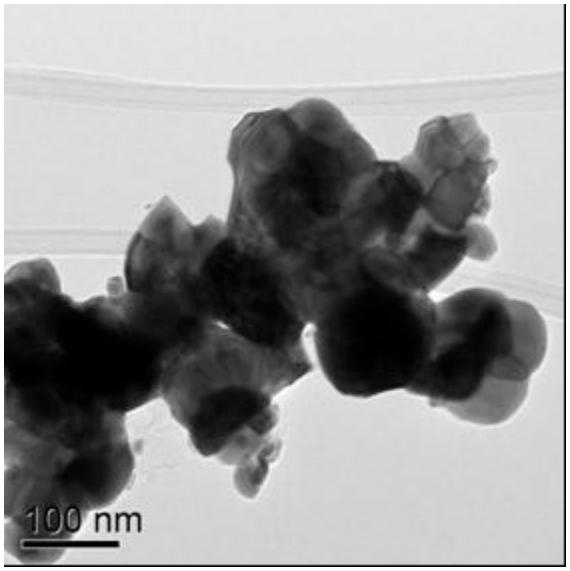

Figure 4. Example of high purity W powder prepared by reducing the GNP precursor in dry H2 at 650ºC for 4hrs. Note that most of the individual crystallites that make up this ~600nm long agglomerated powder particle are less than 50nm in size.

A number of similar and different processing options were explored for the tungsten alloy nanocomposite candidates, rather than the high purity W, again with the goal of increasing material density without excessive growth in grain size. Increased density benefits ballistic performance by allowing a projectile to bring a greater quantity of kinetic energy to bear upon a smaller presented area of the impacted target. An exact value for the maximum grain size required for the tungsten or tungsten composite to exhibit the desired ballistic behavior was not known, and certainly varies with the type of tungsten-based material being studied, but was generally believed to be less than 300 nm (19).

2.2 TECHNOLOGY DEVELOPMENT

Since the 1990's, it has been known that the superior performance of DU alloys in kinetic energy projectile applications is linked to DU's failure behavior (adiabatic shear failure) under the high rates of deformation occurring in ballistic impacts (20). A long rod projectile of high density penetrator core material defeats an armored target by burrowing a cavity through the armor plate. In the process, the long rod itself is eroded in length, by inverting or back-extruding against the penetrator-target interface as the interface moves through the armor. Both the inverting penetrator core and the armor material in the path of the moving penetrator-target interface are being deformed at very high rates (10^5 to 10^6 sec^{-1}). High hydrostatic pressures (exceeding 5 or 6 GPa) are also developed on the head of the eroding long-rod penetrator at the penetrator-target interface. This high hydrostatic pressure environment effectively suppresses fracture failures in the penetrator material. However, the high-rate plastic deformation can become unstable, if thermal-softening due to the heat generated by plastic work overcomes a material's work-hardening mechanisms. The instability can lead to plastic localizations, i.e. adiabatic shear bands (ASB) (21). Unlike fractures, ASBs are failure mechanisms that can operate in the environment of high hydrostatic pressures. ASB failures enable the projectile to discard failed penetrator material from its mushroomed or inverted head more quickly, therefore

reducing the size of the cavity it creates in the armor and improving the efficiency with which the penetrator can burrow through armor. Because the DU alloys used in current US kinetic energy projectiles are much more susceptible to adiabatic shear failure than conventional WHAs, DU projectiles develop smaller back-extruded heads (self-sharpen) while burrowing through armors and are more efficient at penetrating and perforating armored targets than conventional WHA projectiles.

Since WHAs are multi-phase composites, prior research and development efforts to improve their penetration performance have focused on compositional and microstructural changes to each phase to affect their plastic stability and localization (adiabatic shear susceptibility) and thus their penetration efficiency (22). For example, improvements in the mass-specific limit velocity have been achieved when the Ni-Fe or Ni-Co matrix in conventional WHA was replaced with one with greater shear susceptibility. However there are limits on the maximum amount of tungsten that can be incorporated into these composites before interfering with the required self-sharpening behavior. Without the development of higher density shearing matrix alloys, the relatively "low" tungsten content in these materials will limit the maximum density of the overall composite and therefore ultimately the penetration performance achievable in these materials. By contrast, replacing the Ni-based matrix with one even more resistant to shear localization, or eliminating the matrix altogether (an all tungsten material of conventional grain size) will cause the penetrator to mushroom even more extremely that for the W-Ni-Fe or W-Ni-Co composites. The penetrator creates an even larger diameter penetration cavity, and penetrates even less efficiently than the conventional WHAs.

Other prior efforts, that are direct precursors to the work in this ESTCP project, have attempted to modify the tungsten phase. By mechanical deformation, grain size refinement, the addition of dispersoids, etc. these efforts sought to increase the strength of the tungsten phase, and reduce its strain hardening and strain rate sensitivity, such that the tungsten phase exhibits or drives the shear localization mechanism. The primary advantage of this approach is the potential for higher composite density, since a minimum amount of matrix alloy is not required to develop the desired shear failure response. The use of grain size refinement to beneficially modify the mechanical properties and increase susceptibility to shear failure (as measured in split Hopkinson bar [SHB] compression tests) has been demonstrated for ball-milled and HIP-consolidated nanocrystalline iron powders (19). While the production of nanocrystalline or nanoparticulate elemental tungsten powders has been achieved (23, 24), the retention of nano-sized grains when these powders are consolidated to near-theoretical density had not yet been demonstrated at the start of this ESTCP project. However other efforts have shown that the susceptibility to shear localization (again, as recorded in SHB compression tests) can be increased through severe plastic deformation of bulk specimens of unalloyed tungsten, a process that yields nano-sized grains within the material (25). Unfortunately these efforts have not yet produced samples large enough to use in ballistic tests and thereby verify the self-sharpening behavior under a ballistic environment.

In the late 1990's however, samples of a tungsten nanocomposite material were produced in sufficient size for ¼-scale ballistic testing in a joint NIST/ARL/ARDEC effort (26). The material was prepared by hot isostatic pressing (HIPing) of a ball-milled blend of tungsten, Ni, and pre-alloyed Cu-Al matrix alloy powder to form a high-density compact that had an average grain size of 230nm. Although achieving a net density of only 15 g/cc, this nanocomposite material

demonstrated greatly improved penetration performance, exhibiting an approximately 50 m/s lower limit velocity against the RHA reference target (when corrected for its lower alloy density) than conventional WHA penetrators. Given that the performance differential between equi-density DU alloy and conventional WHAs is approximately 100 m/s, the W-Cu-Al-Ni nanocomposite material reduced this gap by approximately 50% (26). In addition, results from metallographic analysis suggested that processing improvements can likely enhance binder homogeneity and reduced grain growth, which would lead to further improvements in ballistic performance. However, it was unclear whether to what degree the improved performance of this nanocomposite was due to the refinement of the tungsten grains, since a large volume of this composite was the nanocrystalline matrix. If the shear localization and "self-sharpening" behavior of the W-Ni, Cu and Al composite was driven primarily by the matrix phase, and not the tungsten phase, then this behavior might not occur in composites with the higher tungsten contents needed to achieve overall densities of 17 g/cc or greater. So the efficacy of the overall nanocrystalline approach to developing the desired DU-like behavior had not yet been demonstrated at the start of the ESTCP project. The ball-milled material produced in the NIST/ARL/ARDEC effort suggested promise however, though its processing technique is difficult to scale to large-volume production and would present challenges in densifying the nanoscale materials without resorting to high-cost, low-throughput processing techniques.

Over the past several years, researchers at Pacific Northwest National Laboratory (PNNL) have been developing two alternate nano-size powder synthesis approaches, freeze drying and glycine nitrate process (GNP), demonstrating the scalability of both at the pilot-scale range (100 – 10,000 kg). Flash freeze-drying was originally used to produce an extremely fine 90W-7Ni-3Fe precursor powder. Results from subsequent studies showed that fully dense 90W-7Ni-3Fe components comprised of submicron tungsten reinforcement particles could be readily fabricated from the freeze-dried powders via conventional sintering practice when the powder is chemically reduced under the proper conditions prior to compaction (27). As others have noted, excellent compositional and phase uniformity in freeze dried powders can be achieved when the rates of solution freezing and water sublimation are high. Shown in Figure 6 is a cross-sectional micrograph of a near full density specimen prepared using this approach. Average grain size was approximately 1 micron. On this prior project, PNNL worked with a commercial sub-contractor to develop a pilot-scale version of the freeze-dry powder production process, successfully synthesizing 100 kg batches of tungsten-based powder and converting this into high-density, sintered product, thereby demonstrating its scalability and its potential readiness for use in fabricating ¼- and full-scale tungsten nanocomposite penetrators.

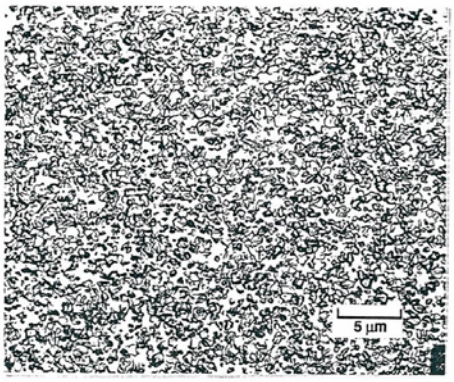

Figure 5. Cross-sectional micrograph of 90W-7Ni-3Fe, produced by sintering PNNL freeze-dried powders at 1200°C for 4hrs.

The second technique, the GNP, was developed to synthesize nanoscale composite and multi-component materials used at elevated temperatures (18). This powder synthesis approach has been demonstrated with a number of metal powder systems including: iron-based, nickel-based, copper-tungsten based, and copper-ceria based. Through proper stoichiometric control of the reactants, a fully reduced metallic (Fe) or partially or fully oxidized (FeO, Fe_2O_3 or Fe_3O_4) ceramic powder, or variations in-between, can be produced. PNNL has licensed the GNP technology to Praxair Specialty Ceramics for use in commercially synthesizing ceramic powders employed in solid oxide fuel cells and gas separation membranes and currently purchases kilogram-size batches of these powders from PSC for their fuel cell projects. The license does not preclude the use of the process for the production of tungsten nanocomposite powders.

The role of nanocrystalline microstructures in inducing the desired shear localization behavior in both nano-scale tungsten and tungsten nanocomposites and in improving the ballistic performance of the tungsten nanocomposites has been demonstrated and reviewed in the series of DoD sponsored publications referenced above (19, 20, 23-26). Internal nano W efforts have been funded within ARL for over five years including efforts to consolidate nanoparticulate W powders via Plasma Pressure Consolidation (PPC) and other efforts to develop nanocrystalline tungsten from conventional grain size bar stock via severe plastic deformation (SPD) processing (Equal Channel Angular Extrusion). The Johns Hopkins University participated in these efforts demonstrating the development of shear localizations in Hopkinson bar compression tests of SPD-processed tungsten (25). The small combined effort by ARL, ARDEC and NIST demonstrated an improved ballistic performance of mechanically ball-milled tungsten nanocomposites in ¼-scale ballistic tests, albeit at a lower alloy density. ARDEC currently administers a Congressional program with the OSRAM Sylvania Corporation program pursuing this approach.

The development and demonstration of the freeze-drying and glycine-nitrate processes in producing nanoscale powders has been previously reported in the following:

- G. D. White and W. E. Gurwell, “Freeze-Dried Processing of Tungsten Heavy Alloys,” in Advances in Powder Metallurgy, MPIF, Princeton, NJ (1989) 355.

- C. A. Lavender and W. E. Gurwell, “Freeze-Dried Tungsten Alloy Components,” Battelle Columbus Laboratory Report, September 1991.

- L. R. Pederson, L. A. Chick and G. J. Exarhos, U.S. Patent No. 5,114,702, "Method of Making Metal Oxide Ceramic Powders by Using a Combustible Amino Acid Compound" (May 19, 1992).

- L. A. Chick, G. D. Maupin, and L. R. Pederson, “Glycine-Nitrate Synthesis of a Ceramic-Metal Composite,” Nanostr. Mater., 4 (1994) 603.

- L. A. Chick, L. R. Pederson, G. D. Maupin, J. L. Bates, and G. J. Exarhos, “Glycine-Nitrate Combustion Synthesis of Oxide Ceramic Powders,” Mater. Lett., 10 (1990) 6.

- K. S. Weil and J. S. Hardy, “Use of Combustion Synthesis in Preparing Ceramic-Matrix and Metal-Matrix Composite Powders,” Cer. Eng. and Sci. Proc., 25 (2004) 159.

- K. S. Weil and J. S. Hardy, “A Model Cerium Oxide Matrix Composite Reinforced with a Homogeneous Dispersion of Silver Particulate - Prepared Using the Glycine-Nitrate Process,” Cer. Trans., 165 (2005) 23.

As discussed in the section above, commercial scalability has been demonstrated in both powder synthesis processes. In addition, the cold pressing, sintering, swaging, HIPing, and/or powder forging steps that are being investigated as low-cost methods of consolidating the nanocomposite powder into demonstration penetrators for ballistic testing all are well-proven, well-understood powder metallurgy processes that have been employed in fabricating moderate-to-large size components (>10 in^3) at commercial production scale.

2.3 ADVANTAGES AND LIMITATIONS OF THE TECHNOLOGY

Because of the “self-sharpening” behavior of the DU alloys used in current US kinetic energy projectiles, they are much more efficient in penetrating and perforating armored targets than the currently used, conventional WHA alternative materials. Depending on the application, DU projectiles offer greatly increased effective ranges against particular threat armor targets, as much as two kilometer increases in the effective ranges of tank gun ammunition than rounds substituting conventional WHA penetrator materials. A tungsten nanocomposite with comparable behavior and performance could offer this significant advantage, while avoiding potentially high political and post-combat environmental costs associated with DU. The magnitude of the costs associated with the use of DU are difficult to accurately estimate because of the lack of agreement among DoD, non-DoD government, and other institutions on how to assess the epidemiological risks attributable to DU’s toxicity and radiological effects, but they are potentially very high.

As mentioned above, concerns have also been raised about the toxicity of conventional WHAs, particularly those incorporating cobalt as a matrix alloy component. Although the toxicology of tungsten has received far less study than that of DU, unalloyed tungsten has shown no adverses health effects when embedded as pellets in rats, over the entire 24-month

implanation time (7). Studies of the toxicity of soluable and insoluable tungsten compounds have not shown a definitive problem linked to tungsten (28,29). Where there has been an issue with W-Ni-Co, i.e. tumor formation, it has been primarily been associated with the corrosion-driven bio-availability of Ni and Co in rats implanted with W-Ni-Co alloy pellets (8,9, 30). The objectives of this demonstration are to confirm the materials and processing technologies needed to produce tungsten nanocomposite anti-armor penetrators that display superior penetration performance relative to conventional tungsten heavy alloy penetrators, while at the same time eliminating matrix alloying elements that are known or suspected to be toxic. In this way, the risk of either perceived or actual environmental or toxicity hazards with their use would be minimized. Successful demonstration of a tungsten nanocomposite penetrator material that can replace DU and provide effective ranges against armored targets will allow the DoD to field anti-armor munitions using a non-toxic penetrator material. Successful deployment of tungsten nanocomposite munitions will facilitate the decommissioning of the DU production base over the next decade, realizing a conservative 40-to-60 percent life-cycle cost savings for DoD operation of the anti-armor munitions production base, as well as eliminate the political, economic, environmental, and health issues associated with the use of DU materials.

Tungsten nanocomposite material technology also has, or may have, several limitations or disadvantages relative to conventional WHA materials. Many conventional WHAs that do not employ cobalt as an alloying addition have been developed and deployed in the field for more than thirty years. While the ballistic performances of these WHAs fall short of that of DU, these are materials are well established commercial products, being produced in large quantities. Metal powder blending, liquid-phase sintering, and post-sinter heat-treatments and cold-working processing methods have been developed which produce products with good engineering properties (strength, ductility, and toughness). And as mentioned, to date studies at the U.S. Army Center for Health. Promotion and Preventive Medicine (CHPPM) and AFFRI have found that implanted pellets of either unalloyed tungsten or conventional tungsten-nickel-iron WHA appear to be cause no tumors in the animal subjects (7). In general, the engineering properties of the tungsten-nickel-iron WHA materials are usually only slightly inferior to those of the tungsten-nickel-cobalt WHAs.

Although it is anticipated that the tungsten nanocomposite materials developed by this technology will exhibit substantially improved ballistic behavior and performance relative to conventional WHAs, and their compressive strengths will likely be higher, the engineering properties of ductility and toughness are likely to be significantly poorer than for either conventional tungsten-nickel-cobalt or tungsten-nickel-iron WHAs. The fundamental reason is that the reduction or saturation of the strain-hardening and strain-rate hardening mechanisms in the new material via grain size reduction, in order to promote plastic instability and shear localization under high loading rates, will also likely limit the ability of a material to deform under more moderate loading rates. The limited ductility and toughness of the nanocrystalline materials will pose technical challenges in developing fully capable munitions for modern weapon systems. Similar challenges of poorer mechanical properties at moderate strain rates have also been seen with other alternatives to DU being developed in the ARL, ARDEC and Congressional programs. Jacketing of the penetrator core and re-engineered sabot designs are already being examined in these programs to help mitigate these potential problems.

In addition, the costs of the tungsten nanocomposite materials are likely to be significantly higher than conventional tungsten-nickel-iron WHAs or DU alloys. The costs of the nanoscale powder production by GNP and the consolidation of the metal powders are expected to exceed that of liquid-phase sintered WHAs. The cost differential between the two depends on the specifications of the initial nanocrystalline powder and of the subsequent consolidated product. Current guidelines based on the synthesis of nanocrystalline GNP powders in 10 kg batch sizes for use in solid oxide fuel stacks suggest an increase in cost of 2 to 8 times that of conventionally processed powder. Further increases in cost will occur if a more expensive solid-state consolidation technique, such as Hot Isostatic Pressing (HIP), is required.

3 PERFORMANCE OBJECTIVES

There were two major performance objectives of this demonstration, see Table 2 below. The first was to validate that the materials and processing technologies developed would produce tungsten nanocomposite anti-armor penetrators that display superior penetration performance relative to conventional WHA penetrators. This was to be demonstrated through quarter-scale ballistic testing of the material. The second objective was the elimination of matrix alloying elements in the W-based materials that are known or suspected to be toxic.

Table 2. Performance Objectives and Results.

Performance Objective	Data Requirements	Success Criteria	Result
Quantitative Performance Objectives			
Ballistic Performance in 1/4 – Scale Testing - Penetration efficiency	• Limit Velocity determination • Test vs. MIL-SPEC armor steel • Customized tests	Demonstrate improved performance versus a conventional WHA of comparable density by a lower limit velocity against RHA target	In very limited testing, best candidate material produced performed no better than conventional WHA.
Environmental and Health	• Examination of the long term corrosion behavior • ASTM F2129 • Immersion Experiments	Materials that utilize only non-toxic or non-hazardous constituents or that form a passive oxide that prevent massive dissolution and degradation of toxic constituents into the body	A test was developed examining the corrosion behavior of candidate W-Ni-Co alloys and W-Ni-Fe alloys in phosphate buffered saline, a simulated physiological solution. The differences seen in these tests correlate with observations in *in-vivo* tests of the same alloys.

The demonstration of the ballistic performance of the nanocomposite material was to occur in prototype testing, using nominal ¼-scale penetrator rods (65g rods with a length-to-diameter ratio of 10 or 15). The consolidated material would be produced as bar stock and machined into a sufficient quantity of penetrators for a proper statistical analysis. Testing would be conducted at the Army Research Laboratory's (ARL) range facilities against known steel reference targets (rolled homogeneous armor (RHA) plate). The results could then be compared to those collected

previously at the ARL on both DU and conventional tungsten heavy alloy (WHA) materials in penetrators of the same scale and geometry (4, 20). A limit velocity (V_L), the velocity at which these projectiles are able to just perforate the reference RHA target, would be determined for each of the PNNL materials to confirm the ballistic improvement. Metallographic examinations of recovered residual penetrators would be used to verify the desired self-sharpening adiabatic shear behavior of these alloys in ballistic environments. Technical success was to be measured by comparing the limit velocities and penetration depths of the ¼-scale tungsten nanocomposite penetrators with the two baseline materials (DU and conventional WHA). As a preliminary screening test, small caliber tests, using small samples of the candidate nanocrystalline materials, were also planned, to confirm the basic shear localization and "self-sharpening" behavior prior to manufacture of the ¼-scale rods. The planned tests in small caliber later proved to be moot however, since unfortunately no sufficiently large samples of the synthesis-processed nanocrystalline material were produced during this project. Only one sample material of sufficient quality was produced in this project, and the bar stock was dedicated to use in the critical ¼-scale test. Its performance was not as hoped however, performing no better than conventional WHAs of the same density. The details of the planned small caliber and ¼-scale testing procedures are given in Section 5. As mentioned earlier, the efficacy of a nanocrystalline approach to develop a shear localizing and "self-sharpening" behavior was in fact demonstrated about a year into this project, in a parallel program using a different manufacturing route. Those details are restricted but could be provided in a classified addendum to this report.

The second objective of this project (see Table 2, Environmental and Health above) included monitoring of the progress on the health and environmental studies of W-based materials. As needed, samples of the nanocrystalline materials were to be submitted to ongoing toxicology tests in support of the current project.

In a preliminary investigation, we also attempted to verify that the material compositions being considered in this study would be viable, environmentally friendly alternatives to DU, ones that avoid the catastrophic health effects observed during animal studies involving embedded fragments of tungsten-nickel-cobalt. ARL currently is currently working with the US Army Public Health Command, formerly the U.S. Army Center for Health Promotion and Preventive Medicine (CHPPM) and the University of Texas – El Paso, to examine and perform metallurgical analysis on the metal pellets from the CHPPM *in-vivo* study of the health effects of embedded tungsten heavy alloys fragments in Fisher 344 rats. The tungsten nanocomposites in this program were to be added to the health and environmental study efforts, and should the materials prove promising in the ballistic trials would be included in further embedded fragment tests at CHPPM.

We have also continued work examining the toxicity issues associated with current and possible future tungsten composites. We initiated a parametric study of the effect of Fe concentration on the corrosion behavior of WHAs. Kalinich and coworkers had demonstrated that intramuscularly embedded fragments of 91.1 weight % (wt%) tungsten – 6.0 wt% nickel – 2.9 wt% cobalt (91W-6Ni-3Co) resulted in aggressive rhabdomyosarcomas in rats (6). Roszell and coworkers later confirmed this result but showed that Fisher 344 rats implanted with commercial-purity tungsten (pure W) and 97.1 wt% tungsten – 1.7 wt% nickel – 1.2 wt% iron (97W-2Ni-1Fe) showed no overt adverse effects (7). Schuster and coworkers proposed that the dramatic difference in the toxicological effects can be explained by stark differences in the

corrosion behavior of these materials (8,9). Both WHA materials (97W-2Ni-1Fe and 91W-6Ni-3Co) showed preferential anodic dissolution of the binder phase. For 91W-6Ni-3Co, this corrosion process was unimpeded and rats were exposed to ever-increasing concentrations of W, and suspected carcinogens Ni and Co. In contrast, *in-vivo* corrosion of 97W-2Ni-1Fe was associated with formation of a passive iron-oxide that effectively halted operation of the galvanic corrosion cell and dramatically limited the bioavailability of hazardous metal cations. Hence, no overt adverse health effects were found. Pure W exhibited only limited pitting and corrosion. No overt adverse health effects have been reported associated with implantation of pure W in laboratory rats or rabbits.

In the parametric study initiated here, we adapted an ASTM standard (31) for evaluation of medical implant materials (ASTM 2129 - Standard Test Method for Conducting Cyclic Potentiodynamic Polarization Measurements to Determine the Corrosion Susceptibility of Small Implant Devices) in order to predict the *in-vivo* corrosion behavior any possible serious adverse health effects associated with embedded fragments of these materials. To guide the alloy development in this study, we investigated the corrosion behavior of the candidate materials, as well as the alloys used in the prior Fisher 344 rat studies, in a simulated physiological solution, as a method to evaluate potential toxicity. The results are detailed in Section 5, but the test method was considered successful as a Tier 1 screening test as the results found in this corrosion test correlated with the results of the Fisher 344 rat studies. In all, nine candidate WHA compositions for the nanocrystalline process, including alloys of W-Ni-Co, W-Ni-Fe and W-Ni-Fe-Co were fabricated as laboratory surrogates for munitions materials.

4 SITES/PLATFORM DESCRIPTION

4.1 TEST PLATFORMS/FACILITY

The small caliber and the ¼-scale ballistic tests were conducted at the ARL's indoor firing range, EF110 facility. None of the candidate nanocrystalline W-based materials produced in this project were of sufficient quality or scale to perform all of the planned tests. Thus, ballistic limit velocities for the tungsten nanocomposites were determined by a few critical ballistic tests instead of the methodologies described in detail in Section 5 Test Design.

4.2 SITE-RELATED PERMITS AND REGULATIONS

The EF 110 Test Facility is one of ARL's fully-enclosed indoor ranges, where approximately 2000 firings are conducted every year, of weapons and projectiles ranging from small arms (5.56mm rifle) of up to 40mm gun systems and projectiles. The range is equipped with a negative-pressure air handling system, to capture propellant gases and any aerosols generated during high-velocity ballistic impacts, which is then exhausted through three sets of air filtration systems, the last being HEPA filtration. Discharges through the range air handling systems are monitored by the ARL Safety Office and the Occupational Health Office located at Aberdeen Proving Ground. The range is operated under both Army and ARL Standard Operating Procedures (SOPs), and all personnel are trained in the handling of ammunition and explosives, all relevant SOPs, and are required to utilize proper Personal Protective Equipment (PPE) when working in the range.

5 TEST DESIGN

5.1 CONCEPTUAL EXPERIMENTAL DESIGN

The use of ¼-scale projectiles have been demonstrated in extensive testing and ballistic modeling as an acceptable means of measuring and comparing the penetration efficiency of experimental long-rod penetrator materials in the Army's various KE penetrator development programs. These projectiles will be machined from the consolidated nanocomposite material. Ballistic tests will be conducted at the ARL KE firing range against a 76.2 mm thickness of rolled homogeneous armor (RHA) plate (Military Specification 12560-H, Brinell hardness of BHN 286-321) at normal incidence to determine the ballistic limit velocity. This is the minimum velocity at which any penetrator can just perforate a given target and is one of the accepted figures of merit in making comparisons between candidate KE penetrator materials. The performance of the nanocomposite material (of given density) can be judged relative to DU and conventional tungsten heavy alloy penetrator materials by its density and its position on the limit velocity versus density plot shown in Figure 7. Note on this plot that better performing materials lie lower on the plot, having a lower limit velocity (requiring less velocity and energy) than comparable poorer performing penetrators of the same mass (65 g) and geometry (same dimensions at the same material density). Note that the DU data points (in red) lie well below those of the conventional WHAs (in black), and the still poorer performing extreme mushrooming materials such as unalloyed W and tungsten-tantalum lie above the conventional WHA performance trendline. The goal of this effort is to produce a tungsten-based composite whose performance approaches or lies within the yellow box shown in Figure 7. Standard post-ballistic test evaluations would also include recovery of the residual (behind-armor) penetrator in a soft recovery package on complete perforation tests, and sectioning of the RHA target on partial penetration tests, for metallographic examination and verification of the desired shear localization behavior. Because the security classification guide classifies the performance and the processing required to develop that performance based on the level of performance, the distribution level assigned to the data would be determined based on the levels of performance achieved in the tests. Similarly, certain critical processing details had been withheld during the quarterly progress reports until that determination could be made.

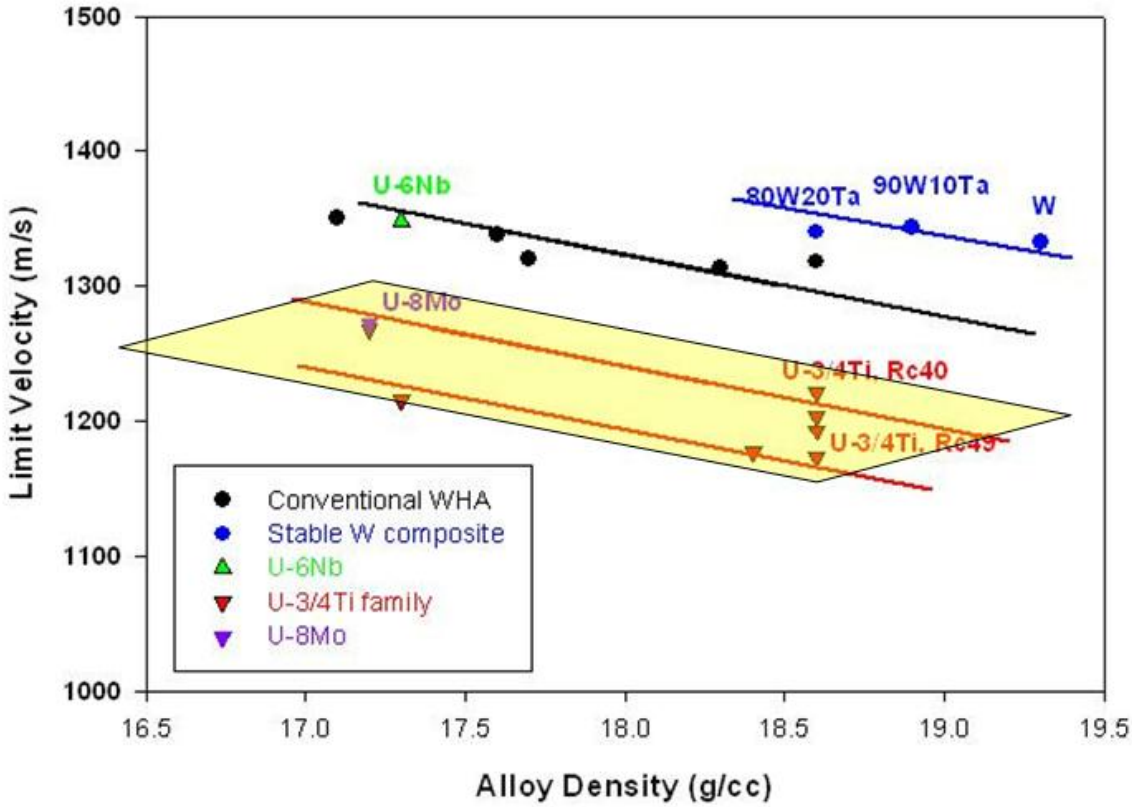

Figure 6. Limit Velocity versus Alloy Density (for L/D = 15 quarter-scale penetrators [65g]).

The results of the ¼-scale ballistic testing of the candidate nanocrystalline tungsten or tungsten composite were to be the critical determination of the potential utility of the material. Pre-demonstration tests using small caliber sized test specimens were also planned, since with just a few of these tests, using very small samples (of a mass of less than 4 grams) of the candidate materials, the material's basic behavior could be assessed. The small caliber test was to serve as a pre-screen for selection of the best candidate to be tested in the ¼-scale ballistic tests. The ¼-scale ballistic test samples are significantly larger (65 grams each) and dimensionally have a much higher aspect ratio (length-to-diameter ratios of 10 or 15). Making a sufficient number of ¼-scale penetrators to generate a statistically significant result would require a much greater quantity of the pre-cursor metal powders and the consolidation of much larger pre-forms to produce bar stock sufficient to manufacture the penetrators.

Initial corrosion screening of candidate materials, as an initial toxicity screen, can also be accomplished with smaller scale specimens, and are discussed below. The schedule for these efforts was part of the overall project and is included in the Schedule of Activities Gantt chart below.

Table 3. Demonstration Testing- Experimental Design of Ballistic Tests.

Demonstration Testing – Experimental Design of Ballistic Tests								
Testing Phase	**12/10**	**6/11**	**12/11**	**6/12**	**12/12**	**6/13**	**12/13**	**3/14**
1st tier Initial Toxicity Screening								
Pre-Demonstration Testing								
Machine subscale penetrators of baseline penetrator materials								
Conduct subscale ballistic testing of baseline materials								
Machine subscale penetrators of candidate penetrator materials								
Conduct subscale ballistic testing								
Examine recovered residual penetrators, downselect candidate for ¼-scale tests (evidence of shear localization?)								
¼-Scale Ballistic Tests								
Machine blank ¼ scale sabots								
Manufacture ¼ scale penetrator bar stock								
Customize ¼ scale sabots to dimensions of 65g rods, machine 1/4scale rods of downselected material								
Conduct ¼ scale ballistic tests								
Determine limit velocity, examine sections targets, evaluate performance relative to DU and WHA							Δ	

5.1.1 SMALL CALIBER BALLISTIC SCREENING TESTS

It was anticipated that, during the development of candidate tungsten nanocomposite penetrator materials, there would likely be difficulties early on in either producing consolidate bar stock of sufficient size from which to machine the ¼-scale, 65 g ballistic test specimens (long rod penetrators.) It was also possible or even likely that initial candidate materials will lack sufficient ductility and toughness, or will contain small defects in early lots of production, that the material may not survive even the very gentle and primarily compressive loads of the push-launching method used in the ¼-scale tests (see Section 5.1.2 for more detail).

Once a preferred method of powder consolidation had been developed, preliminary ballistic testing were to be conducted during the optimization phase of the project, using a modified

small caliber test projectile, shown in Figure **8** below, and was to replace the SHB testing originally planned as a pre-screen.

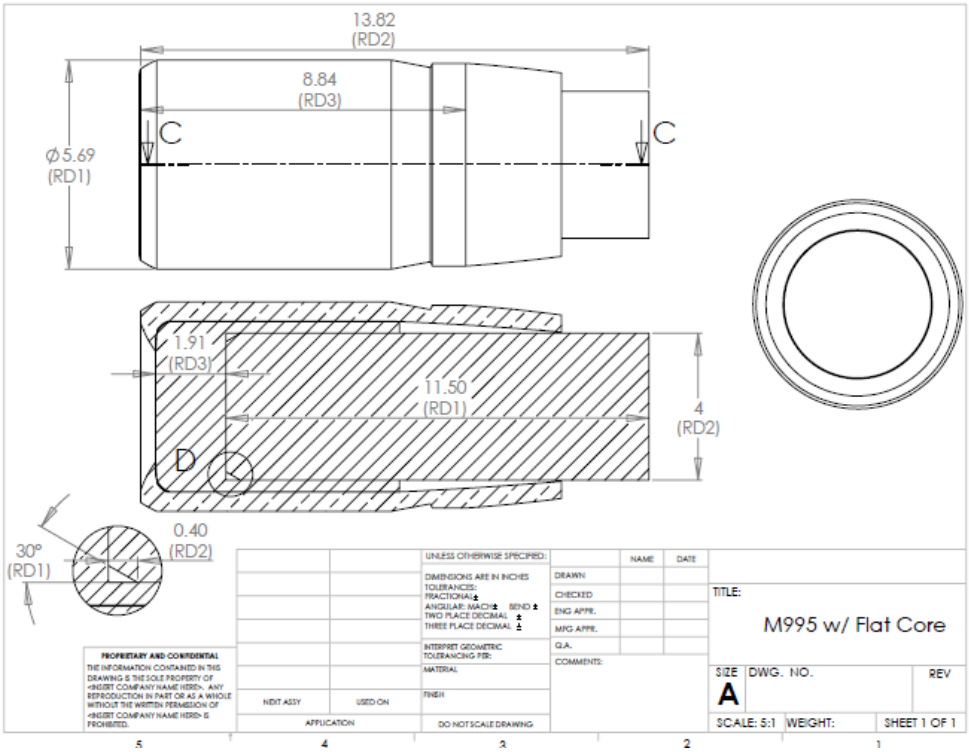

Figure 7. Small Caliber Test Projectile for Sub-Size Specimens.

These projectiles, based on a small caliber projectile design, are built to be fired from a standard 5.56mm M16A2 rifle, at velocities of up to 1000 m/s. Spin of the projectile, imparted by the rifling of the M16 barrel will gyroscopically stabilize the projectile in flight. Candidate tungsten nanocomposite materials would be tested side-by-side with identical small caliber projectiles incorporating conventional WHA penetrator cores and DU penetrator cores (baseline comparison tests). All of the projectiles were to be fired into thick (50.8mm or 2-inch) mild steel target plates at the same impact velocities (the velocities determined via the same flash x-ray system to be used for the later ¼-scale tests, as described in Section 5.1.2 below). The mild steel targets would then be sectioned in half, using wire electric discharge machining (EDM), so that the depths of penetration achieved by the candidate tungsten nanocomposite materials, and the results (penetration depths and behavior of the material evidenced in the residual penetrator cores, see Figure 9, compared to that of the baseline WHA and DU materials). Unlike the limit velocity comparisons in Figure **7**, (where a lower limit velocity indicates a greater penetration efficiency, i.e. requires less energy to perforate the fixed armor plate), instead, for these fixed impact velocities, greater penetration performance is indicated by the achievement of greater penetration depth. Besides allowing one to measure penetration depth (from the plate's original front surface), the sectioning of the mild steel targets also allows one to characterize the deformation and failure behavior of the penetrator material itself, by examining the residual length of penetrator embedded in the steel plate. Examples of the three proto-typically observed behaviors (4) are shown in Figure 9.

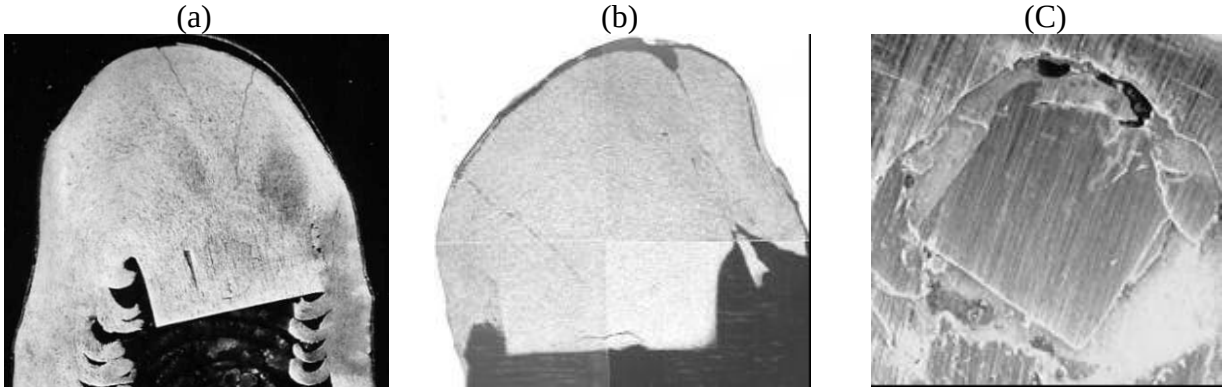

Figure 8. Deformation and Failure Behavior of (a) Unalloyed Wrought Tungsten, (b) Conventional Tungsten Heavy Alloy, and (c) Uranium-3/4% Titanium Alloy.

Comparing the appearance of the three different penetrator materials in Figure 9, one immediately notes the ASB failure behavior of the DU alloy that enables the projectile to discard failed penetrator material. This results in the pointed or chiseled nose appearance of the head of the residual DU projectile in Figure 9(c). Since material was discarded from its nascent mushroomed or back-extruding head more quickly, the size of the cavity it creates in the armor was therefore reduced and the penetrator's efficiency in burrowing through armor improved. Both the unalloyed tungsten, Figure 9(a), and the conventional WHA, Figure 9(b), projectiles developed large mushroomed heads as the eroding penetrator material was back-extruded from the moving penetrator-target interface. As a result, the penetration tunnels displaced by these projectiles are larger in diameter than the DU projectiles (even when the original penetrator rods had the same mass, dimension and density). The presence of a large mushroomed head on the residual penetrator of the tungsten nanocomposite can be taken as a sure sign that the desired adiabatic-shearing or "self-sharpening" was not achieved, and will also be associated with a penetration cavity that is larger diameter but shallower in depth. The residual penetrators recovered from tests of the candidate material or materials in the ¼-scale demonstration tests described in the next section could also be examined in the same manner.

5.1.2 ¼-SCALE BALLISTIC TESTS TO DETERMINE LIMIT VELOCITY

A limit velocity is defined as the velocity at which a given projectile will just perforate a given armor. By using a standardized projectile mass, 65 g, and a standardized projectile geometry, rod with a length-to-diameter ratio (L/D) of 10 or 15, and determining the velocity at which they will just perforate a standardized armor plate, 76.2mm or 3–inch Rolled Homogeneous Armor (RHA), the relative performance of different penetrator materials (of differing densities and mechanical properties) has been established. This has been shown graphically in Figure **7** above. Each limit velocity is determined by varying the impact velocity and, if the projectile perforates the target, measuring its residual velocity, in order to gradually narrow in on the threshold or limit velocity. The orientation of the projectile with respect to its trajectory, its pitch in the vertical plane and yaw in the horizontal plane, are carefully controlled not to exceed one degree in either plane (which would slightly reduce its performance). The numerical value of the limit velocity is determined from a least squares fit to the impact velocity-residual velocity data pairs.

The candidate penetrator materials were to be machined into 65 g projectiles, right circular cylinders with a hemispherical or ball nose, and an overall length-to-diameter ratio of either 10 or 15 (databases of penetrator materials produced under the same constraints of fixed 65 g mass and fixed overall L/D exist for both L/D ratios). These penetrator cores would be fired from a laboratory gun system at ARL (37). This system consists of a 38mm bore diameter and a 40mm breech system. The barrel is a 10 feet (3 meters) long, thick walled, smooth bore barrel. This system allows for very controlled launch velocities and relatively gentle launch (compared to the more rapid accelerations applied by the higher propellant gas pressures and shorter gun barrel lengths of fielded weapon systems). The penetrator is assembled in a four-piece plastic sabot which wraps around the penetrator core and supports it in bore. The penetrator rod and the sabot are push-launched from behind, by a .3" (7mm) thick steel pusher disk embedded in a polypropulux obturator. The obturator traps the gases behind the launch package and accelerates the entire launch package down the barrel of the gun. A sample launch package is shown in Figure **10**.

Figure 9. A sample laboratory launch package, note this example is for a threaded penetrator rod and a smooth right circular cylinder rod will be used in these tests.

The muzzle end of the gun is located approximately 2-3 meters from the target. Upon exit from the muzzle, the air entering the 45 degree "scoops" machined into the front of the four sabot petals causes the four petals to separate and lift away from the penetrator core, with very little disturbance to the motion of the core itself. At this short flight distance, no method of flight stabilization, i.e. fins, drag flares, or gyroscopic spin is required to keep the axis of the projectile aligned with its trajectory.

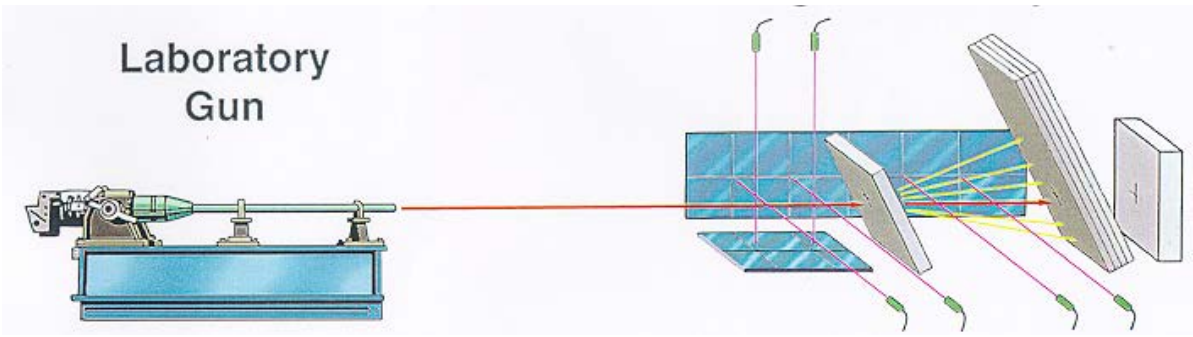

Figure 10. A Schematic of the Experimental Facility, with Smoothbore Gun Location, and Multiple Orthogonal Flash Radiographs to Record Test Data.

The range facility shown schematically in Figure **11** is instrumented with multiple flash x-ray imaging tubes, mounted perpendicular to two orthogonal film planes (38). Images of the penetrator in flight are projected onto both the horizontal and vertical x-ray film planes. Each pair of orthogonal images is projected onto the film simultaneously, capturing the projectile's apparent position in space at that instant. Figure **12** shows the two images of the penetrator in one film plane, taken at different times while the projectile is in free flight toward the target.

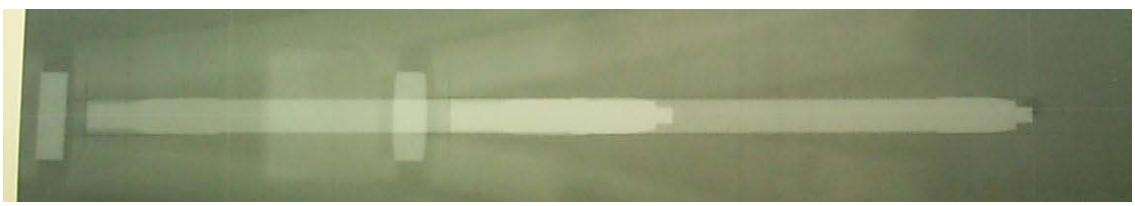

Figure 11. A Sample of the Pre-impact Radiographic Images.

The perpendicular distances between the x-ray tube heads and the x-ray film planes are measured and known prior to ballistic testing. Reference fiducial wires, drawn across the plane of the x-rays allow one to determine the amount of projection of the x-ray images (shadows) of the projectile in flight in each plane. Solving for the amount of projection in both orthogonal planes simultaneously allows one to accurately determine the actual projectile's position in space (from which it cast the shadows at the measured positions on the films). By using the projectile's position in space at the times each pair of orthogonal x-ray tubes are flashed and the preset time delays between each set of orthogonal imaging, the impact velocity is determined accurately from the radiographs. The reference fiducial wires are also used to determine the orientation of the penetrator, its pitch in the vertical plane and yaw in the horizontal plane, prior to impact with the target. A combined (summed) pitch and yaw components exceeding 1.5 degrees (total yaw) unfavorably influence (reduce) the performance of the projectile and the data from these tests will be discarded from the statistical analysis to determine a limit velocity.

In addition to the impact conditions, radiographs are used to record the effects of the penetrator and target debris after the target is perforated. Usually only two images of the penetrator exiting the rear of the target and any behind armor debris, taken with some pre-set time delay between the images and only in one plane of view, are recorded. These can be used to determine the velocity, mass and angle of departure (from the original shotline) of the residual

penetrator pieces, and of the target debris exiting the back of the armor. A sample radiograph showing the two images of the behind armor debris is shown in Figure **13**.

Figure 12. A sample of the behind armor radiographic images.

The limit velocity, the velocity at which the penetrator will just perforate the armor, is determined from the impact and residual velocity data pairs. Several shots are fired at varying degrees of overmatch (striking velocity), and the residual velocities are recorded. These data are then fit to an empirical fitting curve to determine the limit velocity.

The ballistic limit or limit velocity, V_L, for the new candidate material is determined from a fit of the striking velocity, V_S, and residual velocity, V_R, data pairs collected in the tests by means of the flash x-ray techniques. The V_S and V_R data pairs are least squares fitted to an equation of the form:

$$V_R = A({V_S}^P - {V_L}^P)^{\frac{1}{P}},$$

where A and P are empirical constants (39).

A plot illustrating this procedure is shown below in Figure **14**. The point at which the fitted curve intersects the impact velocity axis is defined as the limit velocity.

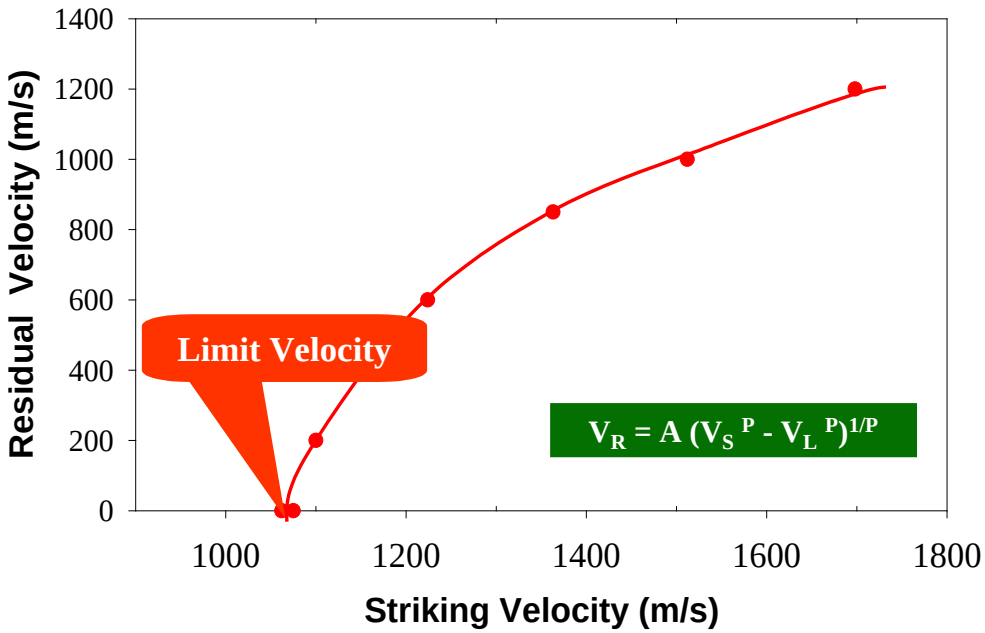

Figure 13. Sample Limit Velocity Determination.

The relative ballistic performance of the new candidate material can then be compared to the baseline conventional WHA and DU materials by plotting its limit velocity against the alloy's density in the graph shown in Figure 7. Again, the lower the data point appears on the plot, the better the material's relative performance.

The residual penetrators recovered from these ¼-scale tests were also to be examined in the same manner as described above for the small-caliber pre-demonstration testing. Again, the presence of a large mushroomed head on the residual penetrator of the tungsten nanocomposite can be taken as a sure sign that the desired adiabatic-shearing or "self-sharpening" was not achieved, and will also be associated with a penetration cavity that is larger diameter but shallower in depth. On the other hand, the presence of a pointed or shear-chiseled nose on the residual penetrator, with penetration tunnels having very roughened walls, created by the irregular shear band discard of failed material from the head of the penetrator, is a positive indicator, and should be further confirmed by the achievement of a lower limit velocity against this fixed (3-inch RHA) target plate.

5.1.3 CORROSION TESTS

We proposed that the dramatic difference in the toxicological effects found for 97W-2Ni-1Fe and 91W-6Ni-3Co in the studies cited in Section 3 can be explained by stark differences in the corrosion behavior of these metals. In both WHA materials, the preferential anodic dissolution of the binder phase is found. For 91W-6Ni-3Co, the *in-vivo* corrosion process is unimpeded and rats are exposed to ever increasing concentrations of W, Ni (a known carcinogen) and Co (a suspected carcinogen). For the 97W-2Ni-1Fe is associated with formation of a passive iron-oxide that effectively halts operation of the galvanic corrosion cell and dramatically limits the bioavailability of Ni. Hence, no overt adverse health effects were found (7).

In the parametric study initiated here, we adapted an ASTM standard for evaluation of medical implant materials (ASTM 2129 - Standard Test Method for Conducting Cyclic Potentiodynamic Polarization Measurements to Determine the Corrosion Susceptibility of Small Implant Devices) in order to predict the *in-vivo* corrosion behavior and whether there was a possibility of serious adverse health effects associated with embedded fragments of these materials. To guide the alloy development in this study, we investigated the corrosion behavior of the candidate materials, as well as the alloys used in the prior Fisher 344 rat studies, in a simulated physiological solution, as a method to evaluate potential toxicity. The results are detailed in Section 6, but in summary the test method was considered successful as a Tier 1 screening test. In particular, the results found in this corrosion test correlated with the results of the Fisher 344 rat studies. In all, nine candidate WHA compositions for the nanocrystalline process, including alloys of W-Ni-Co, W-Ni-Fe and W-Ni-Fe-Co were fabricated as laboratory surrogates for munitions materials.

Similar corrosion experiments were to be performed on the candidate tungsten nanocomposite penetrator materials. We were to compare the corrosion behavior of the nanocomposites to the coarse grained WHA surrogates. Limited corrosion may indicate that these candidate materials are viable replacement materials that will have limited environmental or health effects. Caution must be used as these experiments are not a proven method to be used as a tiered approach to toxicity testing. However, these results can leverage ongoing environment, safety, and occupational health research being conducted at a number of laboratories by a number of researchers including AFRRI, CHPPM, ERDC, and internationally (6, 7, 15, 17, 35-39).

5.2 FIELD TESTING

No field testing of the tungsten nanocomposite material was planned. The use of ¼-scale projectiles have been demonstrated in extensive testing and ballistic modeling as an acceptable means of measuring and comparing the penetration efficiency of experimental long-rod penetrator materials in the Army's various KE penetrator development programs.

5.3 MEASUREMENT/MONITORING PLAN

5.3.1 MEASUREMENT PLAN FOR BALLISTIC TESTING

The measurement techniques for determining striking velocity, projectile orientation, and residual velocity are described in detail in Section 5.1.2 above, as well as the method of analysis to determine the limit velocity. The relative performance of the tungsten nanocomposite can then be assessed by plotting its limit velocity – alloy density data point on the graph shown in Figure **7**. Better performance is indicated by data points that appear lower (at lower limit velocities) and further to the right (at higher alloy densities).

5.3.2 MEASUREMENT PLAN FOR TOXICITY TESTING

Some preliminary measurement techniques for toxicology testing are outlined above in Section 5.1.3. Additionally, Kane and coworkers have suggested that a complete tiered approach to toxicity testing could include a range of experiments and data collection ranging from a paper study on the health effects, cell line cytotoxicity testing, all the way up to an embedded fragment

study of the long term health effects. Many of these are outside the scope of this demonstration plan, however if the candidate materials are found to be prone to corrosion, they may be referred to Tier 2 protocols including short and long term *in-vivo* testing in a rodent model (17).

5.4 LABORATORY MATERIAL TESTING

All of the testing to be conducted in this Demonstration Plan will consist of laboratory tests, as summarized in Table 2 above.

6 PERFORMANCE ASSESSMENT

6.1 CONSOLIDATION OF NANOCRYSTALLINE W-BASED MATERIALS

Two approaches to synthesize nanograin tungsten and tungsten heavy alloy powders were validated initially for use in developing a high-performance tungsten-based anti-armor penetrator. The first of these, the flash freeze-drying process outlined in Figure 4(a) produced an extremely fine, homogeneous powder via the sublimation of water from a frozen mixture of dissolved precursor salts (ammonium metatungstate [AMT] and metal nitrates). The resulting material was calcined and subsequently reduced to form the final nanograin powder. Solution freeze-point analysis was used to identify a suitable temperature range for droplet freezing (for AMT-only and AMT-Fe/Ni nitrate solutions) and subsequent drying by sublimation; namely < -30°C. Thermogravimetric analysis and differential scanning calorimetry (TGA/DSC) were used to identify an appropriate calcination temperature (found to be $\geq$ 450°C) to form a phase pure oxide precursor for reduction. Subsequent X-ray diffraction (XRD) measurements indicated that the average crystallite size of the oxide is on the order of 20 - 30 nm when calcination is carried out at the minimum temperature. Hydrogen reduction of the oxide powder was initially conducted at 750°C, producing an agglomerated phase pure metal powder with an average constituent grain size of 50 – 60nm.

The second technique, the glycine nitrate process (GNP), consists of two basic steps as shown in Figure 4(b): (1) the formation of an aqueous metal nitrate-glycine solution that (2) is heated to dryness and eventual autoignition, at which point a self-sustaining combustion reaction takes place producing the final powder product in a matter of a few seconds. In this process, the glycine serves two purposes: it prevents precipitation of the metal salts as the water is evaporated, thereby ensuring that the metal ions remain molecularly mixed in solution up to the point of combustion or chemical conversion, and it acts as the fuel for the combustion reaction by undergoing oxidation with the nitrate ions during heating. The post-combustion processing steps (i.e. calcination and hydrogen reduction) are similar to those employed in freeze drying. Again combined DSC/TGA indicated that powder calcination should be conducted at temperatures in excess of 450°C. The subsequent reduction of calcined GNP powder at 750°C produced phase pure agglomerated tungsten with grain sizes averaging ~30nm.

Preliminary sintering experiments were conducted on both sets of powder by compacting dry powder in a ¼” diameter die at 150 ksi and heating the resulting green compacts at 2°C/min to 1000°C, holding at this soak temperature for 2hrs, and cooling at 2°C/min to room temperature, all under flowing H_2 gas. The green and as-sintered densities of these materials are summarized in Table 4. Note that the GNP powder used here was composed solely of tungsten whereas the

freeze dry (F-D) powder additionally contained iron and nickel, elements typically used to improve the densification of tungsten via a liquid phase sintering mechanism. Shown in Figure **15**(a) and (b) are scanning electron microscope images of sintered materials prepared from these powders.

Two preliminary conclusions were drawn from this data set:

(1) The F-D W-Fe-Ni material nearly achieves the desired final density ($\geq$ 17.41 g/cc) for the penetrator application. However the addition of Fe-Ni in the freeze-dried powder also appears to promote grain growth to nearly 1 micron (the target grain size is $\leq$ 200nm.). This is often seen when sintering is conducted at higher temperatures such as 1250°C (the typical sintering temperature for a W-7Fe-3Ni material due to the formation of a liquid Fe-Ni rich phase that enhances densification). Tungsten dissolves into the Fe-Ni liquid, which greatly increases the diffusional transport of this element and leads to subsequent grain coarsening via an Oswalt ripening mechanism. However at 1000°C, liquid formation is not expected, and yet the grain size increased from ~60nm in the original powder to over 800nm in the final densified compact.

(2) The GNP powder produces a much finer grained sintered compact, on the order of 300nm, which nearly met our target. However the final density of the material was significantly lower than desired. It should be noted that the green density (density before sintering) of all these compacts is rather low for a powder metallurgy (P/M) product; i.e. <50% of theoretical density (TD), whereas commercial P/M compacts are often pressed to 70+% TD prior to sintering. It was felt that increasing green density would increase final density, and a suitable sintering aid might enhance densification at temperatures below 1000°C.

Table 4. Green and sintered* densities of compacts prepared using F-D and GNP powders.

Process	Composition	Green Density (g/cc)	Sintered* Density
F-D	W-7Fe-3Ni	9.20	16.27
F-D	W-7Fe-3Ni	9.14	15.70
F-D	W-7Fe-3Ni	9.01	15.18
GNP	W	9.60	15.80
GNP	W	7.95	13.45

*Sintering was conducted by heating the green compacts in H_2 at 2°C/min to 1000°C, holding at this soak temperature for 2hrs, and cooling at 2°C/min to room temperature.

(a) (b)

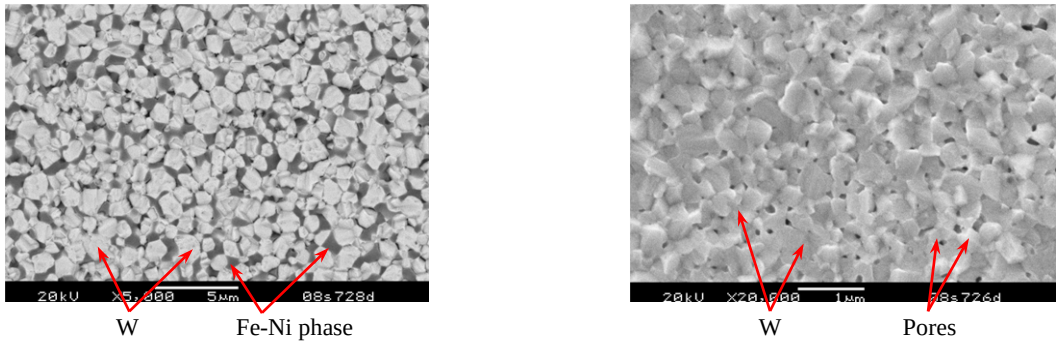

Figure 14. Sintered compacts prepared from (a) F-D W-7Fe-3Ni and (b) GNP W-only powders. Sintering was conducted by heating the green compacts in H2 at 2°C/min to 1000°C, holding at this soak temperature for 2hrs, and cooling at 2°C/min to room temperature.

The rest of the work focused on finding powder synthesis strategies needed to meet our sintered density and average grain size targets. Possible options included: (1) modifying the reduction conditions to produce metal powders with even finer grain sizes and thus enhanced sinterability, (2) identifying a sub-1000°C liquid phase sintering aid (potentially one that minimizes tungsten solubility and thereby mitigates a source of tungsten grain growth), (3) alternatively identifying a non-liquid phase sub-1000°C sintering aid, and (4) incorporating a non-soluble nanometric dispersoid (such as a stable oxide) that minimizes excessive grain boundary motion and therefore grain growth during sintering. In addition, there are compact processing options that we considered as well, including: (5) a post-sinter hot isostatic pressing step to increase compact density, (6) pre- or post-sinter swaging of the compacts to improve density, and (7) incorporation of a shear processing (e.g. rod rolling or extrusion) to increase density and/or modify the microstructure of the material. It was hypothesized that liquid phase sintering [Option (2)] would offer the best opportunity to simultaneously achieve both high density and sub-200nm grain size, presuming an appropriate liquid composition could be determined. In addition, Options (1) and (4) could be readily tested using either F-D or GNP processed powders. A series of four compositional families were chosen for synthesis by both precursor processing methods:

(1) W only – chosen to serve as a baseline against which the effects of sinter aid and dispersoid addition would be measured. It also used to examine the effects of oxide reduction process variables on powder crystallite size.

(2) W-Ag-Cu – while not ideal from a cost standpoint, the Ag-Cu system contains a eutectic composition that forms at $x_{Cu} \sim 0.39$, $T_{eut} = 780°C$. Also, neither silver nor copper exhibits substantial solubility for tungsten. Thus the addition of Ag-Cu can be used to test Option (2) above.

(3) W-Ag-Cu-Ni – the addition of nickel allows some tungsten solubility in the Ag-Cu liquid to occur, offering an opportunity to determine whether a small amount of tungsten solubility promotes additional densification and/or affects the final average grain size within the densified compact.

(4) W-Y_2O_3 – to measure the effect of a non-soluble, non-reactive nanosize oxide on the sintering properties of nanocrystalline tungsten power.

Prior to synthesizing the above materials, a series of experiments was conducted to determine the optimal conditions for powder reduction. GNP and F-D W-only powders were employed and reduction was carried out under the conditions listed in Table 5. Subsequent XRD characterization was conducted to verify that phase-pure metal powder was produced and to determine the average size of the crystallites that constitute the powder. There are several variables that significantly influence both phase purity and crystallite size: (1) the reduction temperature, (2) the original precursor synthesis process employed, (3) the mass flow rate of H_2 across the powder bed, and (4) the powder batch size. Heating rate and soak time also exhibit some effect, although the extent is generally smaller. A minimum reduction temperature of 550°C can be employed to fully covert the oxide precursor to metal in small (3g) batches, however the resulting powder is pyrophoric. Initial attempts to passivate the powder using CO_2 (prior to exposing the powder to the ambient atmosphere) were unsuccessful. To produce small metal powder batches however, a reduction temperature of 650°C (and soak time of 4hrs) was sufficient to yield a stable tungsten powder with crystallites on the order of ~30nm in size. Note that complete conversion from oxide precursor to metal powder at these conditions was consistently achieved with the GNP powder, but not with the F-D material. Reduction of the F-D powder appears to be sensitive to batch size and H_2 flow rate. The reason for this is not known, but may be due to the fact that the GNP precursor is a mixture of WO_2 and WO_3, whereas the F-D material is solely WO_3.

Table 5. Results of powder reduction experiments.

Process	Soak Temperature (°C)	Soak Time (hrs)	Heating Rate (°C/min)	H_2 Flow Rate (cc/min)	Batch Size (g)	Phase(s) Found	Avg GS in W (nm)
F-D	550	4	2	150	3	Likely W*	N/A
F-D	650	2	2	150	3	W	25
F-D	650	2	2	150	5	W/WO_2	N/A
F-D	650	2	2	300	5	W	23
F-D	650	4	50	1000 (est)	5	W	28
F-D	650	4	50	1000 (est)	10	W/WO_2	N/A
F-D	650	4	2	150	3	W	29
F-D	750	2	2	150	3	W	59
F-D	750	4	2	150	3	W	67
GNP	550	4	2	150	3	Likely W*	N/A
GNP	650	2	2	150	3	W	15
GNP	650	4	50	1000 (est)	10	W	26
GNP	750	2	2	150	3	W	30

*The material re-oxidized at room temperature when the furnace was opened.

Powder lots of the above materials (i.e. W-only, W-Ag-Cu, W-Ag-Cu-Ni, and W-Y_2O_3) were prepared by both the F-D and GNP processes and calcined for 2hrs at 450°C. 5 - 10g batches of powder were reduced by heating in 250cc/min flowing H_2 at 650°C for 4 hrs (a heating rate of 50°C/min was employed). XRD results for those powders that have been characterized to date are given in Table 6. Select batches were tested (or are currently undergoing testing) in a dilatometer to determine sintering behavior as a function of temperature. The first such test was conducted on F-D tungsten powder containing 1 w/o Y_2O_3. The average starting grain size of the tungsten powder was 28.2nm (that of the Y_2O_3 could not be determined by XRD). As shown in Figure **16** below, the material begins to densify at ~815°C.

Table 6. Partial set of characterization results for GNP and F-D tungsten alloy or composite powders.

Process	Target Composition	Soak Temperature (°C)	Soak Time (hrs)	Heating Rate (°C/min)	Batch Size (g)	Phase(s) Found	Avg Grain Size in W (nm)
F-D	W-1% Y_2O_3	650	4	20	5	W	28
F-D	W-4Ag-1.4Cu	650	4	2	3	W	29
GNP	W-4% Y_2O_3	650	4	50	10	W	27
GNP	W-4Ag-1.4Cu	650	4	50	10	W	28

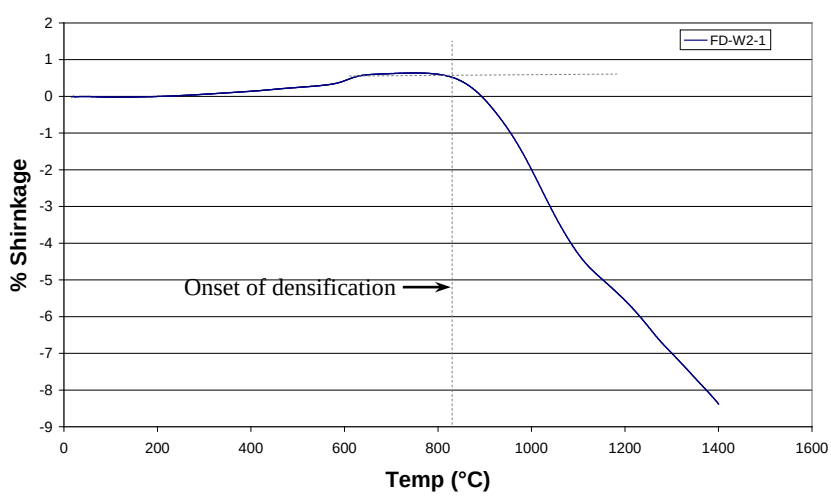

Figure 15. Dilatometry results on a F-D W-1% Y_2O_3 powder prepared by reducing in H_2 at 650°C.

Although both methods of synthesizing nanocrystalline tungsten-based powder, the flash freeze-drying process and the glycine nitrate process (GNP) had been demonstrated, we eventually down-selected GNP as the lead process for synthesizing material for the rest of the work on this project, namely developing an appropriate method of powder consolidation and conducting mechanical testing on the resulting compacts. GNP was chosen for three reasons: (1)

it employs fewer processing steps, (2) it consistently converts completely from the oxide state to the metal state during low-temperature reduction (by comparison under the same reducing conditions, the freeze-dried material often yields a mixture of oxide and metal powders, the ratio which appears to be sensitive to batch size and H_2 flow rate), and (3) the average crystallite size of the metal powder produced is generally smaller than that obtained by the freeze-drying process, which increased the likelihood that the desired tungsten penetrator microstructure (i.e. high density and nanosize grain structure) can be achieved. The remainder of the work in the project sought to identify the conditions needed to consolidate the GNP-produced powder into a high density, nanograin body to serve as the basis for the penetrator.

This initial consolidation work indicated that only 70 – 80% of theoretical density could be achieved with high-purity tungsten GNP powder via a simple press (uniaxial compaction) and sinter process (pre-sinter density: ~50% of theoretical; sinter conditions: heat at 2 ºC/min in dry H_2 to 1000ºC, hold at 1000ºC for 2 hrs, and cool to room temperature at 2ºC/min). However it was noted that the average grain size of this version of sintered GNP tungsten is ~300nm, only slightly above the maximum desired for the application, suggesting that with process optimization the target material microstructure and properties could be achieved. There were a number of possible processing options that potentially could lead to increased material density without inducing a concurrent increase in grain size, including:

(1) Promoting increased green density –increase the density of the original powder compact (which was ~50% of theoretical density) by several approaches: (a) incorporating a powder and/or die lubricant to reduce sources of friction that tend to inhibit powder particle sliding and high powder packing densities, (b) employing higher compaction pressure either during initial uniaxial compaction or during a subsequent cold or hot isostatic compaction step to reduce the size of intraparticle pores, and (c) utilizing shearing forces during compaction to cause particle rearrangement and higher powder packing to take place.

(2) Identifying alternative sintering conditions – higher sintered densities can often be achieved by: (a) increasing the time and temperature at which sintering takes place, (b) increasing the rate of heating to avoid pre-sinter “deadening” of the material, (c) modifying the gas atmosphere (e.g. p) under which sintering occurs, and (d) actively compressing the powder compact during heat treatment via hot pressing or hot isostatic pressing. The key is to avoid accelerated grain growth (AGG), a phenomenon that often accommodates increased sintering activity in nanocrystalline materials and leads to a non-nanograin microstructure in the final as-sintered body.

(3) Continuing the incorporation of sintering aids – controlled additions of certain elements, element combinations, and/or compounds can enhance the mechanisms responsible for tungsten sintering and thereby promote increased material density. Categories of sintering aids include: (a) those that increase the rate of solid-state tungsten diffusion (e.g. Co, Fe, and Ni), (b) those that form a liquid phase that may or may not enhance tungsten diffusion, but through capillary force cause the constituent particles in the compact to draw together and thereby form a high density body, (c) those that induce a reaction with the tungsten (or with the surface

oxide on individual particles), and (d) those that minimize excessive grain boundary motion and therefore AGG during sintering.

(4) Further reducing crystallite and/or agglomerate size, since as shown earlier in Figure **5**, the GNP tungsten powders consist of micron and sub-micron size agglomerates that in turn are made up of nanosize crystallites (or grains). The individual crystallite size depends on a number of factors, but in the GNP process one of the most important is the temperature at which reduction takes place. For example, when hydrogen reduction of a pure tungsten GNP precursor powder is carried out at 750ºC (2 hrs), the average crystallite size formed has consistently been ~60nm in size. This can be halved by lowering the reduction temperature to 650ºC.

There is a limit as to how far this crystallite size reduction strategy could be extended. For example when reduction is conducted at 550ºC, the resulting powder is extremely fine scale and active, so much so that it undergoes spontaneous oxidation (or burn-back) when exposed to ambient atmosphere. Methods to passivate the surface of the powder to mitigate the burn-back phenomenon, were also explored. This included exposing the powder to a finite amount of oxygen or carbon dioxide prior to open air exposure (e.g. by slowly introducing Ar/1% O_2 into the furnace, once the powder bed has been cooled under H_2 gas flow). To reduce powder agglomeration, wet milling the powder in an attrition or ball mill for a relatively short period of time (~20 min), again typically under a protective or passivating atmosphere, was also explored.

Each of the above consolidation strategies was examined. Dilatometry was the primary characterization technique employed to identify which approaches lead to high-density, nanograin tungsten. This technique measures the change in a material's volume as a function of temperature or other external variable. In the case of a sub-dense powder compact, as adjacent powder particles begin to rearrange and sinter, a calibrated push rod in the dilatometer tracks the resulting reduction in compact length allowing an equivalent reduction in volume to be calculated. In this way the sintering behavior of a modified powder or compact can be compared to that of the original baseline material to determine whether the densification phenomenon is aided or hindered by the particular modification under investigation. In cases where the effects of applied pressure during sintering are being considered, an instrumented HIP was employed in approximately the same fashion as the dilatometer to identify promising consolidation conditions.

Summarized in Figure **17** are the results from the powder and die lubrication study. Two different compaction pressures and five different lubrication conditions were tested: $P_{compaction}$ = 350MPa or 1050MPa; no lubrication employed, 0.5wt% naphthalene added to the W powder and employed with or without an additional die lubricant, and 0.5wt% stearic acid added to the W powder and employed with or without an additional die lubricant. The powder lubricants were added by first dissolving the naphthalene or stearic acid in an organic solvent, adding the W powder, and mixing the resulting slurry to dryness as the solvent evaporated. The die lubricant employed was a 5% solution of stearic acid dissolved in propanol. The die platens and inner wall of the die were brushed with the solution and allowed to dry prior to compaction. As observed in Figure **17**, the magnitude of compaction pressure has the largest effect on green density. With no

lubricants employed, the average green density of the tungsten compact increases from 9.71 g/cc (50.1% of theoretical) to 13.31 g/cc (68.8% dense) when the compaction pressure is tripled, a 37% improvement. It is also noted that the addition of naphthalene had little effect on green density, whereas at the lower compaction pressure, the addition of stearic acid lead to a small increase in density. The use of a die lubricant exhibited a slightly stronger effect, leading to increases in green density that range from 15.3 – 29.9% at the lower compaction pressure and 3.2 – 11.8% at the higher pressure.

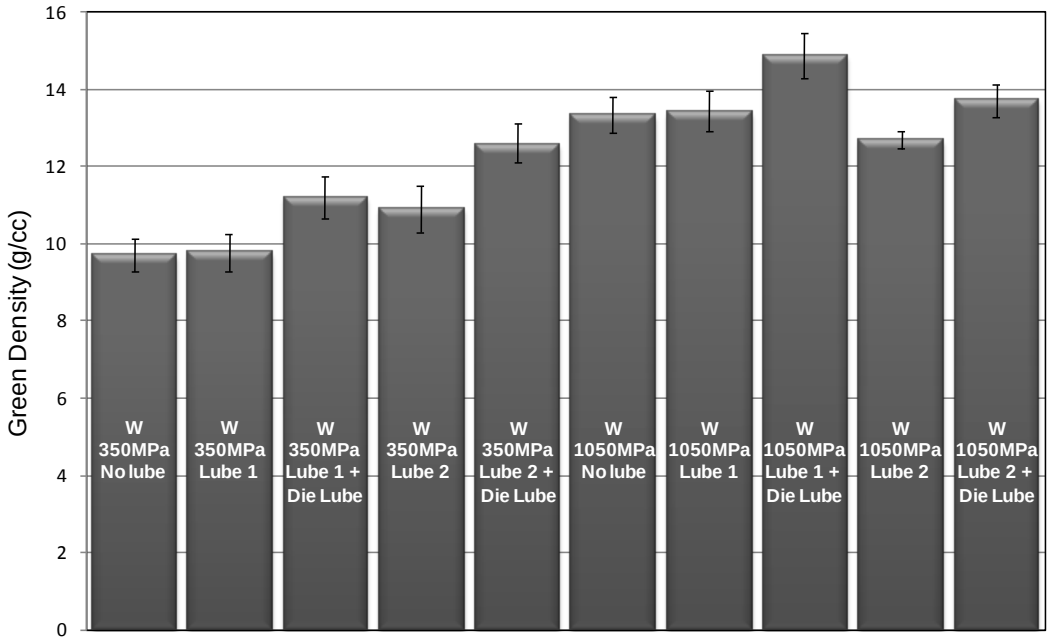

Figure 16. Measurements of as-pressed (green) densities as a function of compaction pressure and powder/die lubricant. Lube 1 = 0.5 wt% naphthalene added directly to the powder, Lube 2 = 0.5 wt% stearic acid added directly to the powder. The die lubricant employed was 5% solution of stearic acid dissolved in propanol.

The study of sintering aid additions was also completed. Shown in Figure **18** is a baseline dilatometry curve for a baseline pure-W powder (with an average particle size of 28.9nm) and a partial set of dilatometry curves for three different families of modified GNP W powder: (a) a Y_2O_3-modified series, (b) a Ag-Cu-modified series, and (c) a Ni-modified series. Nickel is a well known solid-state sintering aid for tungsten that enhances diffusion along the surfaces of individual W particles. Y_2O_3 is being considered as a potential grain growth inhibitor (i.e. grain boundary pinning agent). The eutectic Ag-Cu composition is a possible liquid-phase sintering aid. From the data in Figure **18**, it is noted that with the exception of the 0.05% Ni addition, all of the modified powders exhibit a lower onset temperature (i.e. temperature at which sintering initiates) than pure W. These results suggest that through proper compositional modification, the sintering temperature for nanocrystalline tungsten can be reduced with no measurable loss in densification behavior, which should reduce the potential for AGG. In addition at temperatures above the onset for sintering, the Ni- and Ag-Cu-modified powders exhibit significantly more extensive densification than the baseline powder. Thus both modifications were seen as potential means of increasing the density of sintered nanograin tungsten bodies.

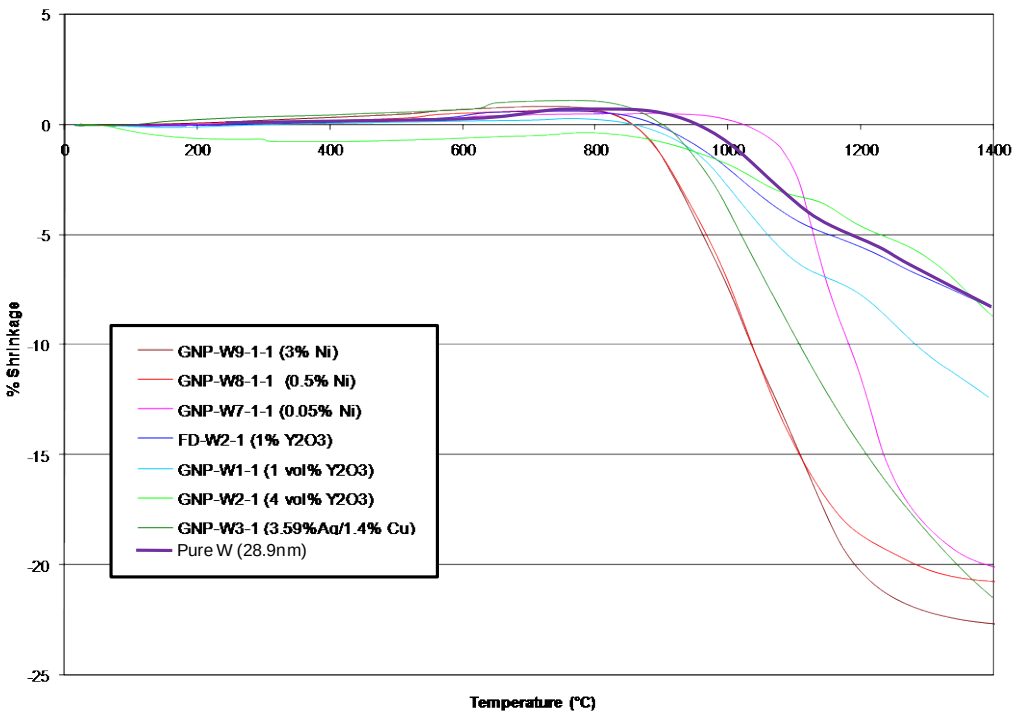

Figure 17. Dilatometry results on a baseline pure-W nanocrystalline powder and three series of modified nano-W powders.

The yttria additions appeared to have small-to-no effect on the sintering behavior of nanocrystalline tungsten. The key metric for this modifier is whether Y_2O_3 dispersions would stabilize the original size of the nanometric grains during densification. TEM analysis of the Y_2O_3 modified powders suggest that this may be challenging to achieve. Shown in Figure **19** are TEM micrographs of a 0.3wt% Y_2O_3-W powder synthesized by reducing a GNP-prepared powder in dry H_2 at 600°C for 2 hrs. Rather than observing nanocrystalline W particles that are uniformly coated with even finer scale dispersion of yttria particles, the yttria was instead found in micron-scale mixed phase agglomerates. These agglomerates tended to be composed of 10 – 50nm size W particles encapsulated within a Y_2O_3 matrix made up of sintered nanometer size crystallites. It is suspected that this microstructure originates from the way in which the GNP precursor powder forms from the initial aqueous solution of ammonium metatungstate, yttrium nitrate, nitric acid, and glycine. In preparing lab-size batches of material, the solution is boiled to drive off the water, after which the glycine and other constituents begin to react and form an oxide-based powder. However, we suspect that phase separation occurs between the drying and combustion steps or during combustion (since this step takes place over a period of several minutes and not instantaneously as might be desired).

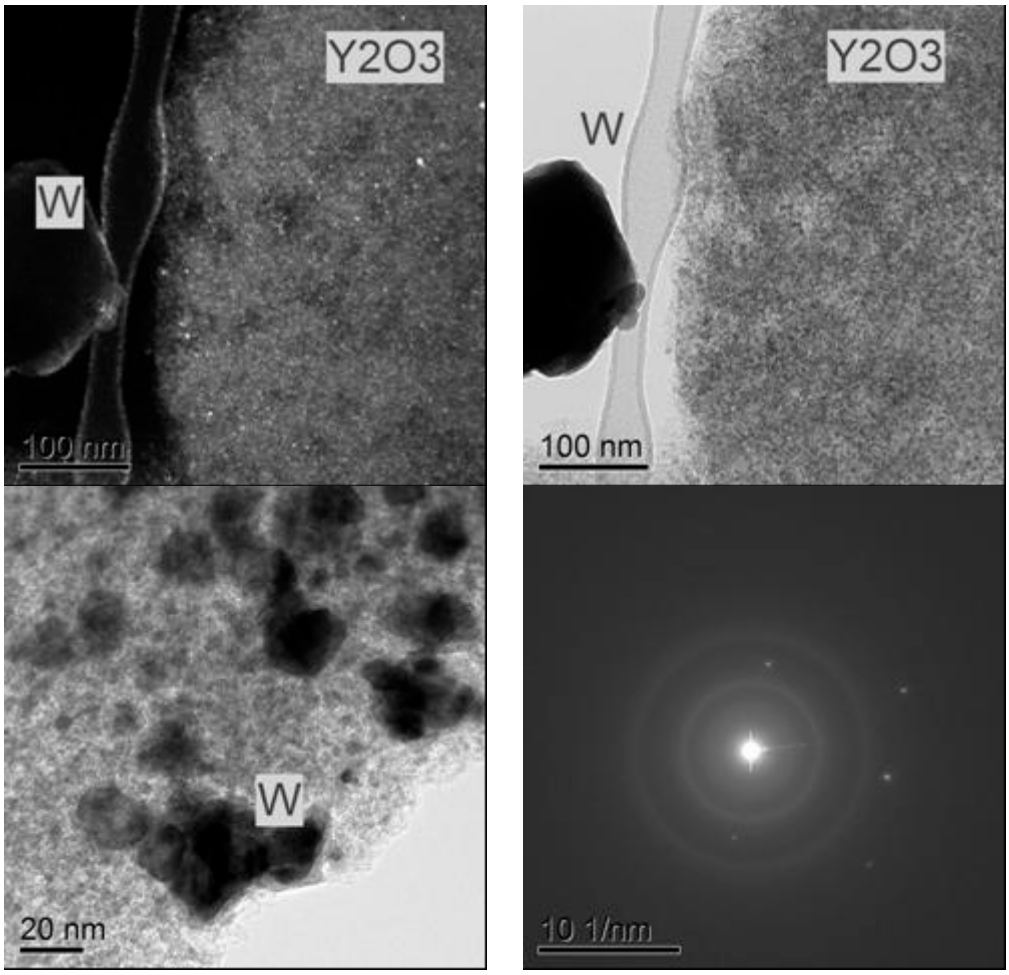

Figure 18. TEM images of a GNP-derived 0.3wt% Y_2O_3-W powder. The diffraction pattern shown is of the Y_2O_3 matrix seen in the second, bright field and third, dark field images.

The above work with high-purity tungsten powder produced by the glycine nitrateprocess (GNP) indicated that only 70 to 80% of theoretical density could be achieved via simple press-and-sinter consolidation processes. The series of W-Ni sintering experiments demonstrated conclusively that as little as 0.05% Ni offers a significant improvement in the sintering of tungsten at temperatures below 1400°C. Shown in Figure **20** are dilatometer results that compare the sinterabilities of W-Ni powders prepared by GNP with that of the baseline GNP W-only powder. The amount of nickel added ranged from 0.05% to 3%. Sintering shrinkages greater than 20% correspond to final densities above 95% of theoretical.

Green compact densities were measured by a geometric method and as-sintered densities were measured via the Archimedes method at the completion of dilatometry testing. During testing, each compact was heated in Ar/2.75% H_2 at 2°C/min to a maximum test temperature of 1400°C, and then allowed to furnace cool. As shown in Table 7, extremely high tungsten densities can be achieved with very small Ni additions. Also seen in Table 7 are results from a series of W-Re experiments that were conducted. Note that the addition of rhenium also leads to

improved density relative to the baseline material, although not to the degree that the nickel sintering aid does.

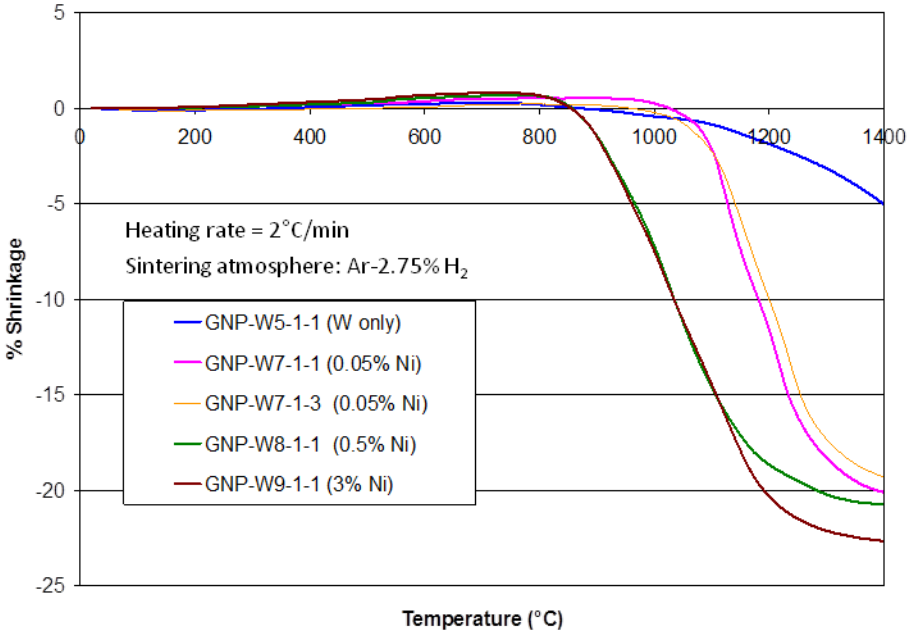

Figure 19. Dilatometry results on a baseline pure-W nanocrystalline powder and three series of modified nano-W powders.

Table 7. Densities of W-based powder compacts before and after dilatometry testing.

Name	Description	Density(g/cm3)	Green Density (%)	Density(g/cm3) after shrinkage test	Sintered Density (%)
W5-1-1	W only GNP powder (59919-56-1A)	9.0	46.3	10.4	53.8
W5-1-2	W only GNP powder (59919-56-1A)	8.8	45.7		
W5-1-3	W only GNP powder (59919-56-1A)	8.9	46.3		
W7-1-1	99.95 wt% W and 0.05 wt % Ni (59919-64-1A)	9.4	49.4	18.9	97.8
W7-1-2	99.95 wt% W and 0.05 wt % Ni (59919-64-1A)	9.4	48.7		
W7-1-3	99.95 wt% W and 0.05 wt % Ni (59919-64-1A)	9.4	48.4	18.8	97.3
W7-1-4	99.95 wt% W and 0.05 wt % Ni (59919-64-1A)	9.4	48.9		
W8-1-1	99.5 wt% W and 0.5 wt % Ni (59919-68-1A)	9.1	47.4	19.0	98.5
W8-1-2	99.5 wt% W and 0.5 wt % Ni (59919-68-1A)	9.1	47.2		
W8-1-3	99.5 wt% W and 0.5 wt % Ni (59919-68-1A)	9.2	48.3		
W9-1-1	97 wt% W and 3 wt % Ni (59919-68-1A)	8.0	42.2	18.4	95.2
W9-1-2	97 wt% W and 3 wt % Ni (59919-68-1A)	8.3	43.3		
W9-1-3	97 wt% W and 3 wt % Ni (59919-68-1A)	8.1	42.4		
W10-1-1	96 mol % W and 4 mol % Re	7.9	40.0		
W10-1-2	96 mol % W and 4 mol % Re	7.7	38.4	15.1	78.2
W10-1-3	96 mol % W and 4 mol % Re	7.8	39.3		
W11-1-1	92 mol % W and 8 mol % Re	8.2	41.9		
W11-1-2	92 mol % W and 8 mol % Re	8.2	41.5	14.7	76.4
W11-1-3	92 mol % W and 8 mol % Re	8.0	41.0		
W12-1-1	96 mol % W and 4 mol % Re	8.4	43.2	14.4	74.4

Uniaxial Press : 3000 psi
CIP: 40,000psi
Sintering atmosphere Ar-2.75% H_2

The densified compacts were polished and etched for microstructural analysis and grain size measurements. The microstructural analysis indicates that under the heat treatment conditions experienced in the dilatometer, significant grain growth occurred in all of the samples (the

starting crystallite size of the powders used in these experiments averaged 28.2nm in diameter). It is important to note that the heating rate employed for dilatometry (which is required for proper instrument operation) is over an order of magnitude slower than what would be used in typical fabrication practice. From the series of micrographs in Figure **21**, it can be observed that under identical heating conditions, the grain size of the tungsten decreases with increasing nickel content. Although this is counterintuitive to general expectations (i.e. typically grain size increases with greater amounts of a liquid phase sintering aid), the underlying reason for this appears to be the formation of intergranular Ni_2W precipitates in specimens containing 0.5% and 3% Ni. Stable particles of this type tend to pin grain boundaries, thereby reducing the amount of grain coalescence and therefore average grain size. This is essentially the same effect, albeit at finer scale, that we had hoped to exploit with the addition of well-dispersed nanoscale Y_2O_3.

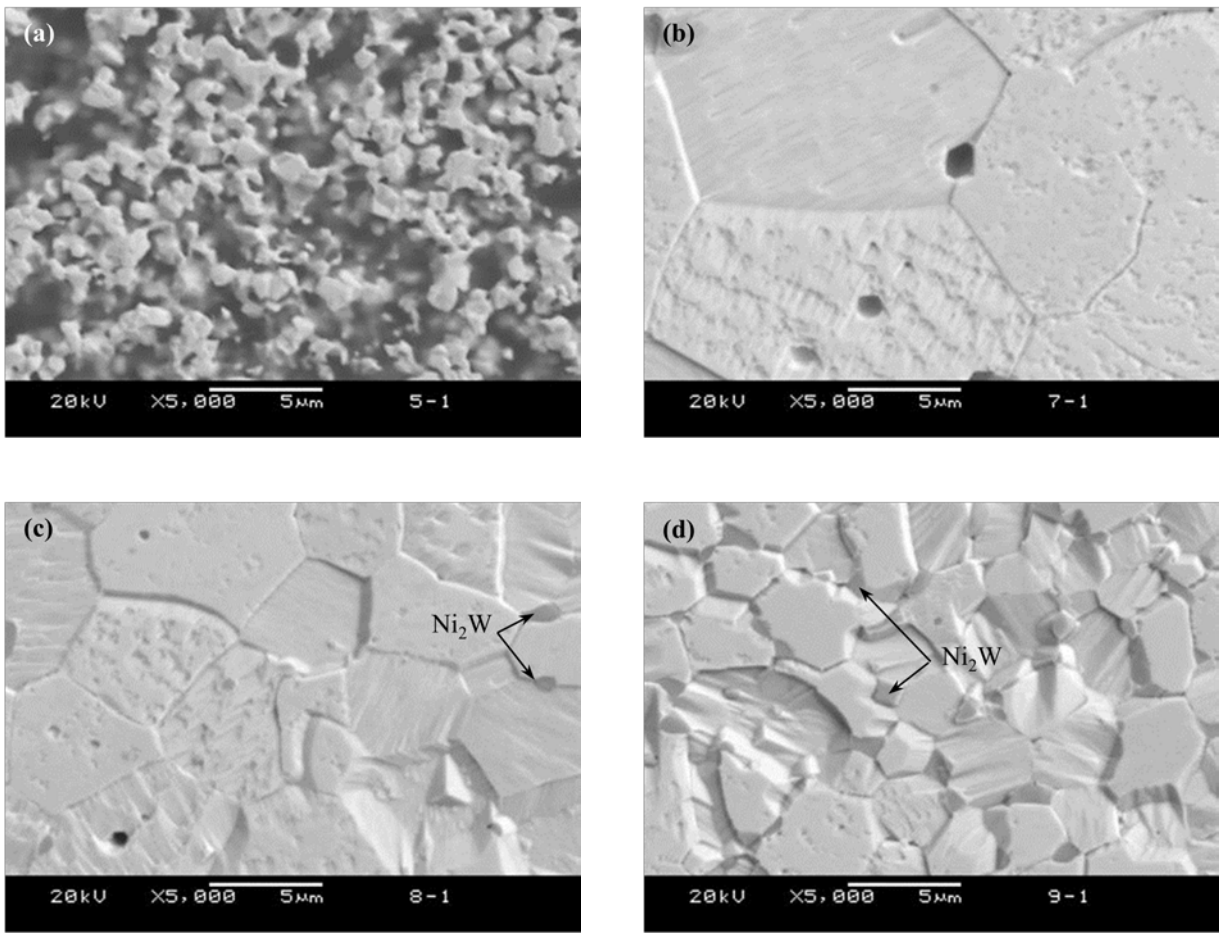

Figure 20. Cross-sectional scanning electron microscope images of: (a) 100% W, (b) W-0.05% Ni, (c) W-0.5% Ni, and (d) W-3% Ni. All specimens densified during dilatometry testing under flowing Ar-2.75% H_2 and a heating rate of 2°C/min. Each sample reached a final temperature of 1400°C.

Separately, work on pure tungsten in a related ARL program (40) has shown the value of incorporating a powder de-agglomeration step into the synthesis process. 45g of high purity W

GNP powder was de-agglomerated at ARL by attrition milling. The resulting powder was then cold pressed into pellets and sintered in flowing hydrogen at either 1400 or 1600°C for 2hrs. Shown in Figure **22** are micrographs that compare the fracture surfaces of the GNP material in the agglomerated versus de-agglomerated condition after cold pressing and sintering at 1400°C. Density measurements indicate that both samples sintered to > 90% density. Note that the specimen produced from the de-agglomerated powder (Figure **22**(c) and (d)) exhibits grains that measure on the order of 200nm in size, meeting the desired target for this characteristic (though still short of the density goal). This work was then repeated and a series of milling experiments conducted to optimize the de-agglomeration process. A preponderance of nanoscale intergranular porosity was noted in polished cross-sectional micrographs of the specimens of the type shown in Figure **23**) however, enough to suggest that the material might display poor ductility. For this reason, we also examined possible methods of reducing/eliminating this porosity, including post-sinter hot isostatic pressing of uncanned specimens at moderate temperatures (on the order of 800°C to mitigate the potential for grain growth), hot swaging of the bars, and/or incorporating a small amount Ni or Re as a sintering aid in the starting W powder.

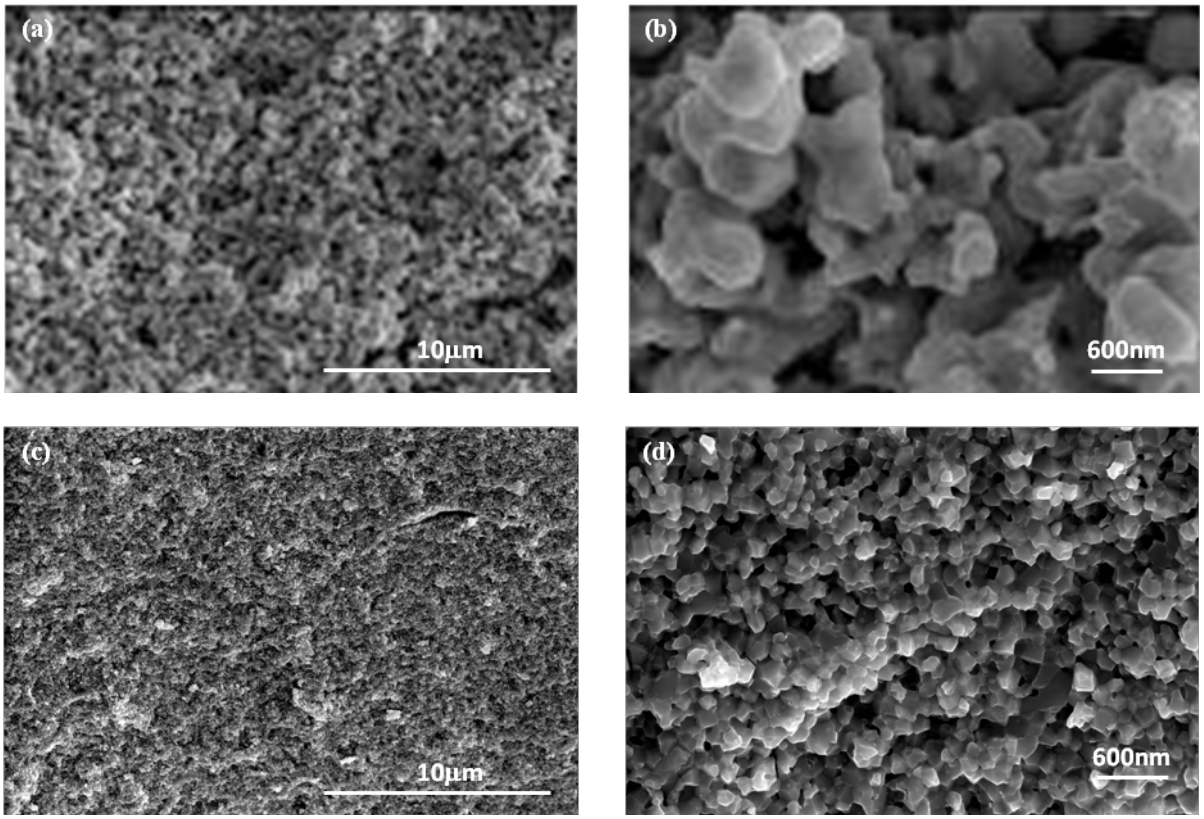

Figure 21. Scanning electron microscope images of the fracture surfaces of: (a) and (b) a 100% W sintered specimen prepared from unmilled GNP powder and (c) and (d) a 100% W sintered specimen prepared from milled (de-agglomerated) GNP powder. Both specimens were sintered under the same conditions at 1400°C for 2hrs in flowing Ar-2.75% H_2.

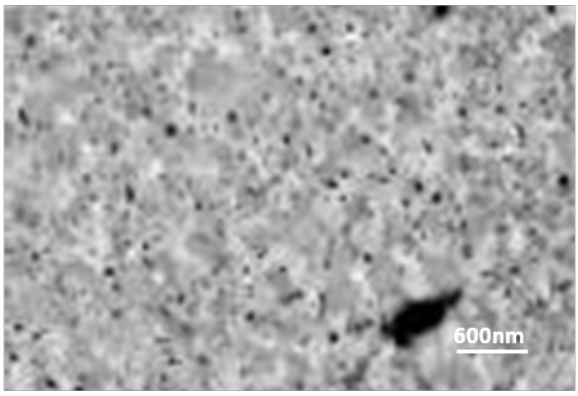

Figure 22. Polished cross-sectional scanning electron microscope image of the specimen in Figures 22(c) and (d). The specimen was prepared by sintering de-agglomerated GNP W powder at 1400°C for 2hrs in flowing Ar-2.75% H_2.

The previous efforts showed that conventional powder metallurgy press and sinter methods required temperatures for full densification that would excessively coarsen the microstructure. Therefore, some trials using Hot Isostatic Pressing (HIP) were conducted to produce small samples that might demonstrate that densifying by HIP, at low temperature and high pressure, might retain the fine microstructure.

PNNL synthesized W-based nanoscale powder in preparation for scale up in a HIP consolidation process. 500g of W-7Fe-3Ni and 500g of pure W were sent to ARL for milling (de-agglomeration by wet milling then spray drying). The powder composition was the 90W-7Ni-3Fe ratio processed from the modified GNP method. Two hot isostatic pressing (HIP) runs were performed at Bodycote at 850^{oC} and $900^{o}C$ using two powder types. The powders that were pressed were 1) 90W7Ni3Fe GNP powder that had been milled by ARL and 2) an as-GNP processed powder that was W-5Re-0.5Ni. The powders were loaded into 3/8" diameter stainless steel tubes and electron beam welded closed using solid ends plugs. Given the low density of the powder in the HIP can (approximately 10% of TD) and the corresponding large amount of deformation expected in the can and welds, the HIP cycle was modified to fully heat the samples to the HIP temperature prior to applying pressure. After HIPing the cans were collapsed and appeared to be intact indicating no leakage during the cycle. The post HIP cans are shown in Figure **24**.

Microstructural characterization of the HIPed samples was performed by scanning electron microscopy and is illustrated by the series of micrographs in Figure **25** through Figure **28**. Figure **25**(a) and Figure **25**(b) are the as polished views of the ARL –milled GNP powders consolidated at $850^{o}C$ and $900^{o}C$, respectively, and show that at the $850^{o}C$ HIP there is some evidence of porosity whereas at $900^{o}C$ little or no evidence of porosity was observed.

Figure **26**(a) and Figure **26**(b), are the as-etched micrographs of the ARL-milled GNP powder consolidated at $850^{o}C$ and $900^{o}C$ and show that the microstructure is typical of a heavily milled powder that has not undergone extensive recrystallization or grain growth during consolidation; the microstructure appears to have retained the as-worked morphology of the milled powder. The grain size of the HIPed milled/GNP powder is difficult to determine given the irregular shape however feature of the structure are less than 100 nm and overall the structure

is very fine. Microhardness testing of the samples was performed and the milled/GNP powder HIP at 850°C and 900°C was 1010HV (65 HRC) and 1350 HV (>HRC scale), respectively. The higher hardness observed in the 900°C HIP was likely due to the complete densification and lack of porosity.

The second powder consolidated by HIPing was the W-5Re-0.5Ni using GNP powder that was not milled and was canned and HIPed after hydrogen reduction. Figure **27**(a) and Figure **27**(b) are the as polished views of the W-5Re-0.5Ni GNP powders consolidated at 850°C and 900°C, respectively, and show that as with milled 90-7Ni-3Fe GNP powder at the 850°C HIP there is some porosity whereas at 900°C little or no evidence of porosity. The as-etched micrographs of the HIPed W-5Re-0.5Ni, given here in Figure **28**(a) and Figure **28**(b), indicate a significantly different microstructure than for the milled W-Ni-Fe powders. For the un-milled W-5Re-0.5Ni powder the grain size is very fine and a large percentage of the grains appear to be less 200 nm and are relatively equiaxed. Microhardness testing was performed on the W-5Re-0.5Ni sample HIP at 850°C and 900°C and found to be 700HV (58HRC) and 1020 HV (66HRC), respectively. As with milled/GNP powder the densification at 850°C appears to be incomplete and may have resulted in the lower hardness for 850°C HIPed samples.

Figure 23. As-HIPed cans GNP W-5Re-0.5Ni (top) and ARL-milled GNP 90-7Ni-3Fe (bottom) at 900°C (left) and 850°C (right).

(a) (b)

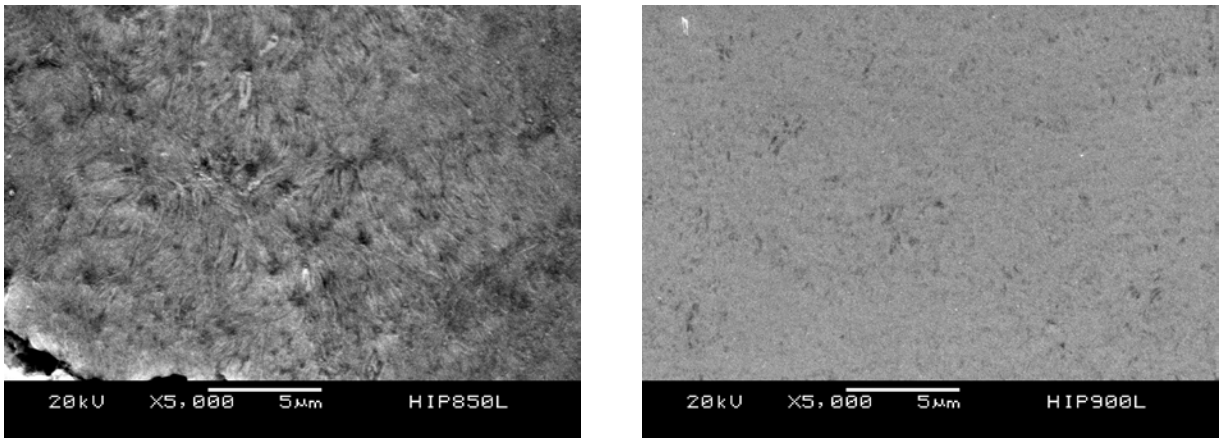

Figure 24. The as-HIPed un-etched microstructure of the ARL-milled GNP 90W-7Ni-3Fe powder HIPed at 850°C (a) and 900°C (b), indicating the increased porosity observed with HIPing at 850°C.

(a) (b)

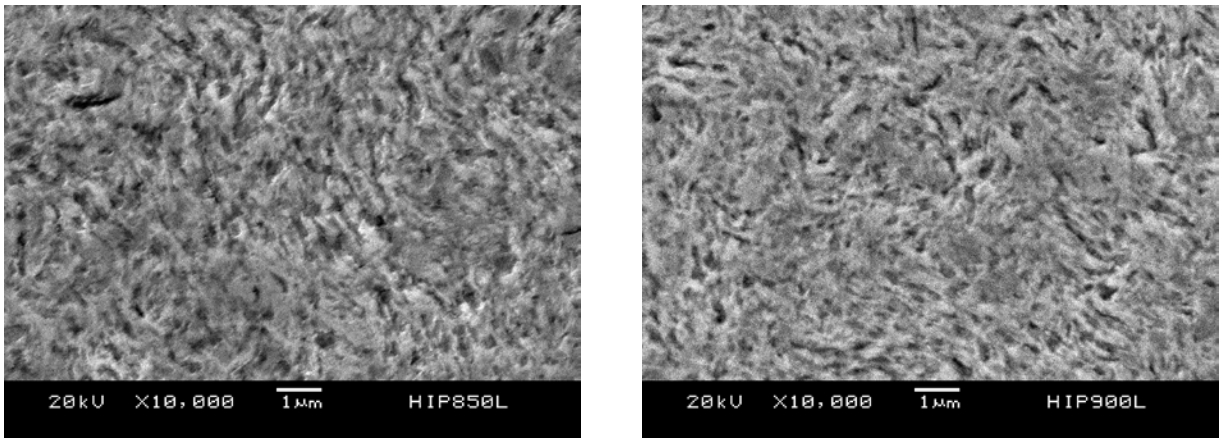

Figure 25. As-etched micrographs of the ARL-milled GNP 90W-7Ni-3Fe powder HIPed at 850°C (a) and 900°C (b). The microstructure appears to have retained the morphology the milled powder and little difference in feature size is observed.

(a) (b)

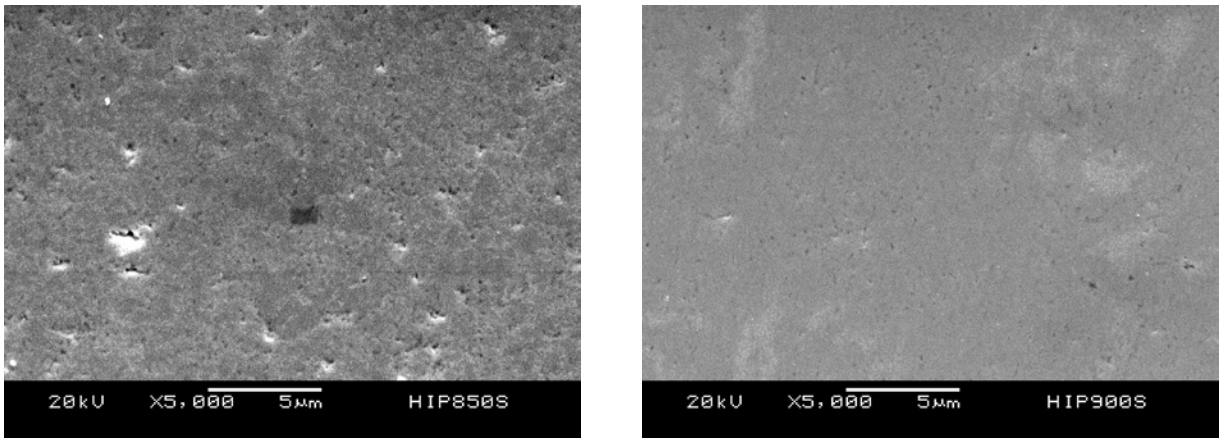

Figure 26. The as-HIPed un-etched microstructure of the HIPed W-5Re-0.5Ni GNP at 850°C (a) and 900°C (b), indicating the increased porosity observed with HIPing at 850°C.

(a) (b)

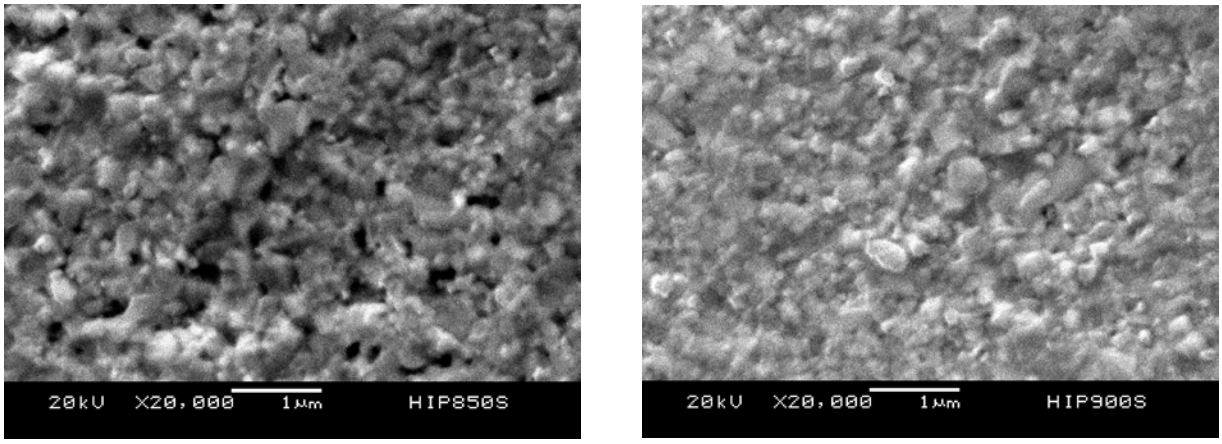

Figure 27. As-etched micrographs of the ARL-milled GNP W-5Re-0.5Ni powder HIPed at 850°C (a) and 900°C (b).

900°C HIPing appears to be the minimum temperature for HIPing as indicated by the residual porosities and the maximum hardnesses achieved in small specimens. Vickers hardnesses in excess of 1000 were measured for the materials consolidated by 900°C HIP were the maximum measured was the 7NI-3Fe produced by GNP and re-processed by ARL. The ARL re-processed 7Ni-3Fe and the 4.5Re-0.5Ni alloys have similar hardnesses but dramatically different microstructures. The scale up of HIP process to produce larger samples, for the ¼-scale ballistic tests or even the small caliber ballistic tests has been difficult and might be attributed to the low tapped density of the fine structured powder. The low tap density produced extreme buckling of

the HIP cans in order to eliminate the void volume, and the resulting densified products extracted from the cans were very small in size and irregular in shape.

At this stage of the project ARL's separate in-house mission program had made significant progress and had successfully consolidated unalloyed nanocrystalline tungsten powders to over 95% theoretical density while retaining nanocrystalline grain size. This was done in samples large enough for quarter-scale testing (65 gram mass long rods). Although the material was extremely brittle, a limited number of ¼-scale tests could be conducted and though short of the needed ballistic performance, the ballistic results showed significant improvement. The material exhibited the desired penetration behavior and delivered a significant improvement in ballistic performance (distribution of the details of the processing history and ballistic results are limited [restricted]). The team decided that, for this next, and last lot, of nanocrystalline powders to be produced using the Battelle combustion synthesis process, the HIPing route would be abandoned, and the ARL consolidation process would be used.

For this last effort, pre-alloyed W-Re powders, produced by the Battelle combustion synthesis process were processed and consolidated at ARL. It was hoped that the pre-alloying of the nano-tungsten powders with rhenium, using the glycine-nitrate process would improve the ductility of the consolidated product, while retaining nano grain size. Although the quantities of W-Re powders produced via GNP were thought to be sufficient for the manufacture of several quarter-scale specimens (65 gram mass long rods), in the end only one sample of bar stock (sufficient in size for ¼-scale tests) was produced at the end of the entire milling, drying, and consolidation processes. The ¼-scale rod, with a length-to-diameter ratio (L/D) of 10, was labeled as sample SST-207-P1. The mass of the rod was 64.41 grams.

Samples were taken for density and hardness measurements and microstructural examination from the original bar stock during the machining operation. The measured hardness of the alloy was Hv 838. The microstructure of the consolidated bar stock is shown in Figure **29**.

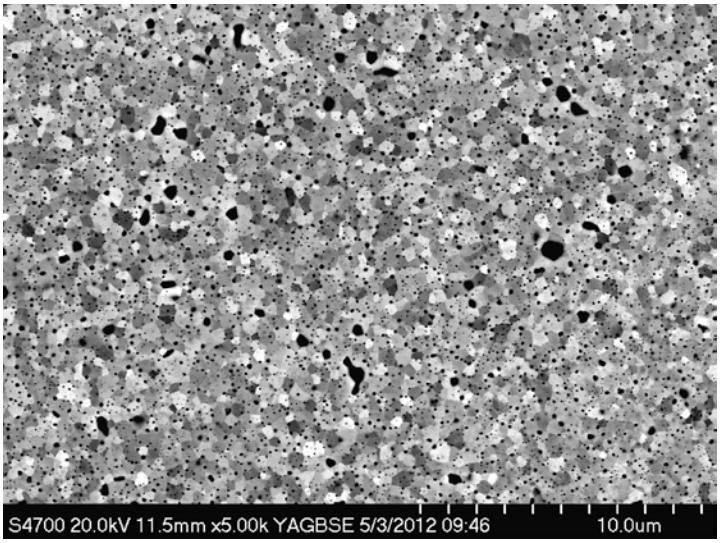

Figure 28. Microstructure of the GNP-processed W-5Re alloys, ARL-milled and consolidated.

The average grain size in the ARL-processed GNP powder W-Re revealed in Figure **29** was sub-micron, but considerably larger than the 200-300 nanometer target. The W-Re powders proved to be more difficult to consolidate the unalloyed W nanocrystalline powders used previously by ARL. Changes to the sintering process required to densify the GNP pre-alloyed W-Re powder are believed to have led to the greater grain growth.

Both SEM images also reveal residual porosity in the consolidated material. The theoretical density of the W-5Re alloy is 19.3g/cc. The actual measured density was 18.61 g/cc, or 96.4% of the theoretical value. This is equivalent to the density of a 97% tungsten WHA (nickel-iron matrix composite). To provide a direct one-to-one comparison of the performance of the ESTCP material and conventional WHAs, side-by-side tests were also conducted using ¼-scale, L/D = 10 rods of a 97%WHA (Teledyne Firth-Sterling's X-9C alloy, 97W-2.1Ni-0.7Co), against the same 76.2mm RHA plate stock.

6.2 BALLISTIC TEST RESULTS

The test firing of the ESTCP material, shot # 5072, was conducted in ARL's EF110E facility, using a 40mm laboratory gun and the simple push-launch laboratory projectile assembly (the package of the 4-petal plastic sabot, steel pusher disc, and plastic obturating plug described in Section 5). The propelling charge was selected to produce a velocity of approximately 1420 m/s. The launch was successful, as shown in the flight x-ray images in Figure **30** and Figure **31** below.

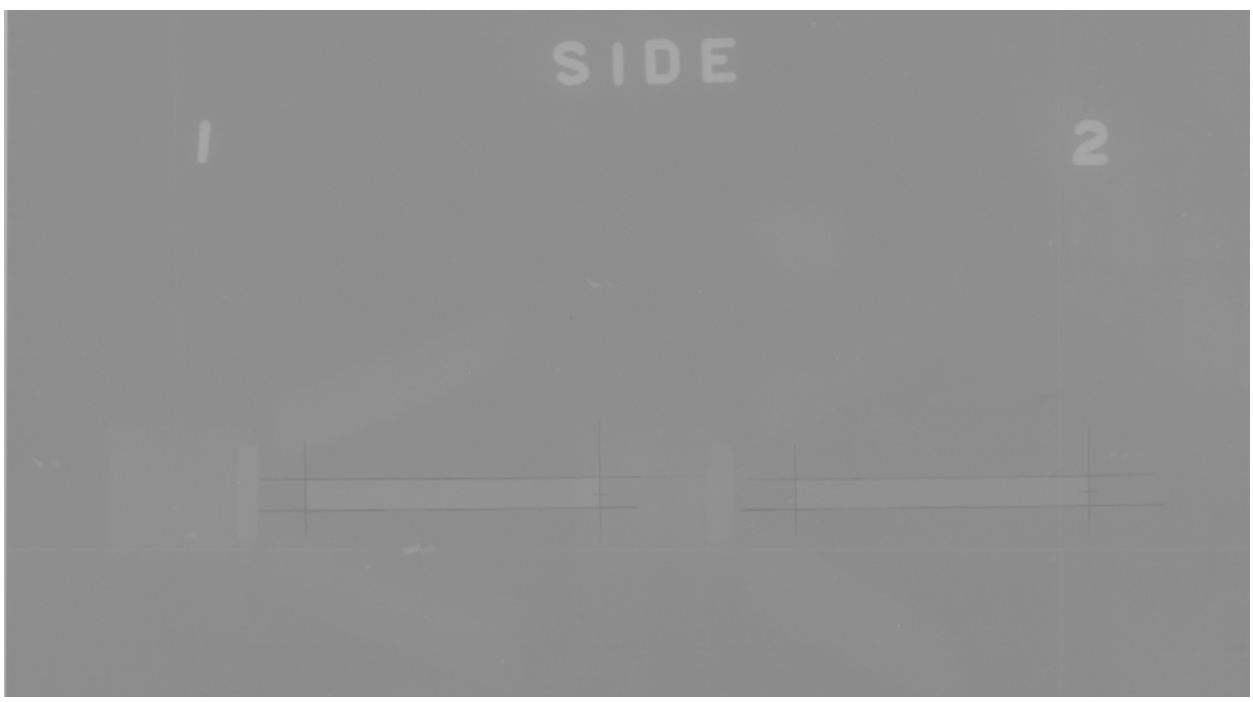

Figure 29. Flight X-ray Images (side view), showing the orientation of penetrator in the vertical plane (pitch) prior to target impact.

Figure 30. Flight X-ray Images (overhead view), showing the orientation of penetrator in the lateral plane (yaw) prior to target impact.

The results are summarized in Table **8**. The W-Re alloy rod stuck the reference 76.2mm RHA target at a velocity of 1417 m/s, with very acceptable low pitch and yaw values (a combined total yaw of only 0.43 degrees). The projectile nearly perforated the plate, producing a large bulge rising 9mm above the plane of the rear of the plate. How close the material came to defeating the target becomes still clearer upon examination of a crossection of the target plate (Figure **32**). The bottom of the penetration tunnel is very near the original rear surface plane of the plate, and a plug of the steel in the process of focusing and shearing free of the bulged rear target face. Again for comparison, tests were also conducted against the same RHA plates with the X-9C alloy WHA projectiles. The results are also listed in Table **8**. Note that the limit velocity for this conventional WHA with the same density as the GNP-synthesized nano W-Re alloy (at 18.6 g/cc), lying between 1410 m/s and 1442 m/s, or very near the expected value of approximately 1420 m/s.

Table 8. ¼-Scale Test Results

Shot #	Pitch	Yaw	Total Yaw	Mass	Velocity	Residual Velocity	Comment
	(deg)	(deg)	(deg)	(g)	(m/s)	(m/s)	
GNP Nano W-Re Penetrator Test L/D=10 Rod vs 76.2mm RHA at 0 Degrees							
5072	0.32	0.28	0.43	64.41	1417	0, PP	9mm bulge
X-9C Tests L/D=10 Rods vs 76.2mm RHA at 0 Degrees							
5057	-0.4	0.74	0.85	65.34	1334	0, PP	2mm bulge
5058	0.20	0.01	0.20	65.37	1501	666	CP
5059	2.18	0.04	2.18	65.37	1465	275	CP
5073	-0.83	-0.48	0.95	65.34	1461	381	CP
5077	1.03	0.09	1.03	64.93	1442	531	CP
5079	0.17	-0.19	0.25	65.07	1404	0, PP	9mm
5080	0.78	0.03	0.78	65.02	1410	0,PP	11mm

Figure 31. Sectioned RHA Plate, Shot 5072

Both the size of the bulge in the plate and the beginning of the shearing of a plug suggest that Shot 5072 was very close to the limit velocity against this plate. At 1417 m/s however, this result is not significantly different from the 1420 m/s limit velocity obtained for conventional WHAs of the same density. Thus, this material did not offer any significant improvement in performance over the conventional WHA materials.

The relative performance of the material is shown graphically in Figure **33** below. Note that although the performance is no better than conventional WHAs, the fact that it is comparable to equal density WHAs means that it is superior to the more stably deforming materials such as the tungsten-tantalum composite, or unalloyed tungsten with conventional larger grain sizes (5 microns or more). It is clear that the finer grain size of the GNP-synthesized, milled and sintered W-5Re powder material did improve the performance of tungsten somewhat, but not enough to exceed that of conventional WHAs.

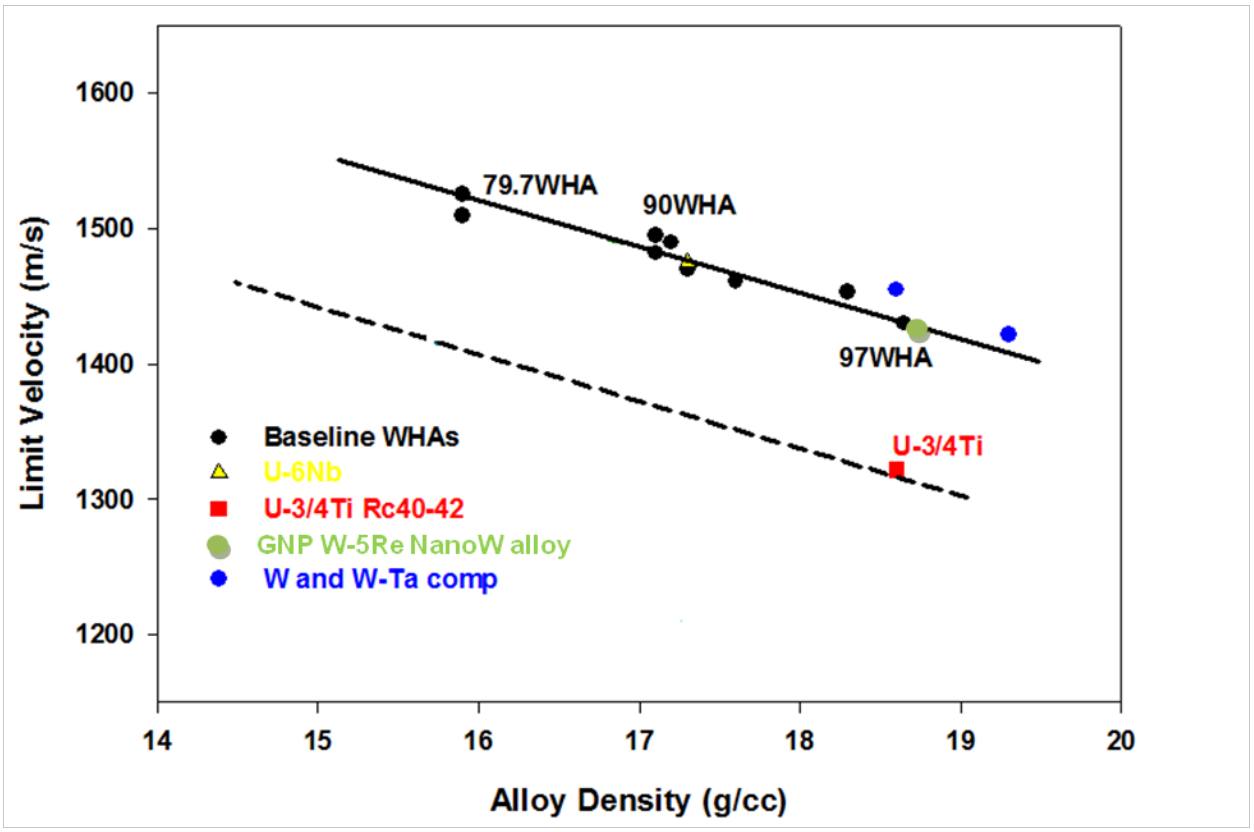

Figure 32. Limit Velocity as a function of alloy density for 65g, L/D = 10 rods against the 76.2mm RHA Plate.

As a preliminary screening test, small caliber tests, using small samples of the candidate nanocrystalline materials, had also been planned but ultimately only one bar of material considered of sufficient quality was produced via the synthesis process, and that rod was utilized for the ¼-scale test described above instead. However, some baseline testing was conducted to determine whether the small caliber test method would be effective as a preliminary screen of candidate penetrator materials. Because the small cal test applies a ballistic loading state, i.e. high rate deformation under conditions of high hydrostatic pressures, it was felt that it would be a better screen of candidate materials than the SHB testing originally planned in the proposal, provided that the test results could be shown to have the necessary fidelity.

Although no samples of a sufficiently nanocrystalline GNP-synthesized tungsten material were of sufficient size and quality to conduct even the small caliber tests, the baseline tests of a depleted uranium alloy, a 97% tungsten content - tungsten heavy alloy, and a 91% tungsten content - tungsten heavy alloy, were conducted. The projectiles were the 7.62mm small caliber test projectiles shown in Figure **8**, fired into 50.8mm (2”) mild steel plate a 7.62mm Mann barrel at velocities of up to 1000 m/s. Spin was imparted to the projectiles by rifling of the barrels to gyroscopically stabilize the projectiles in flight and keep the axis of the projectile well aligned with its trajectory at the instant of target impact. The velocities and the orientations of the projectiles just prior to target impact were recorded by means of flash x-ray instrumentation. After each test, the depth of penetration achieved by each projectile was determined by half-sectioning of the mild steel target via wire electric discharge machining (EDM).

The data from this set of 7.62mm tests are summarized in Table **9** below. The control of projectile alignment using the small caliber projectile was excellent, as mis-alignment of the projectiles (recorded as the total yaw) rarely exceeded three degrees. The tests results also demonstrate that the small caliber test is an effective screening method for candidate materials. When the measured penetration depths are plotted as a function of projectile velocity (Figure **34**), the data clearly distinguish between the performance of the equal density DU and 97% tungsten heavy alloys, as well as between the 97% W and 91% W materials.

Table 9. 7.62mm Tests against 50.8mm Mild Steel

Penetrator Material	Gamma (degrees)	Velocity (ft/s)	Penetration (mm)
97W	3.33	3723	15
97W	1.80	3726	15.2
97W	1.26	3516	14.2
97W	1.53	3191	12.2
97W	0.07	2652	9.1
91W	1.23	3492	12.7
91W	0.47	3096	11.2
91W	0.29	2721	9.1
DU	2.60	3482	15.2
DU	0.43	3108	14
DU	0.43	3108	12.95
DU	3.22	3044	13.2
DU	2.59	2696	10.67
91W	1.54	3782	15.2

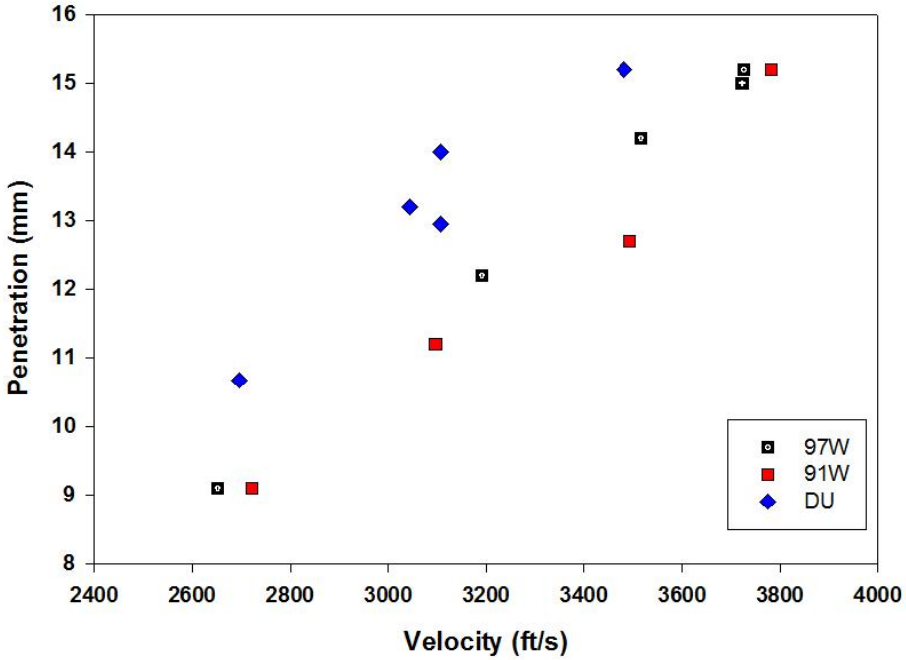

Figure 33. 7.62mm Tests (5.6mm dia. x 13.1mm long cylinders) vs. Mild Steel.

While no lots of GNP-produced nanocrystalline powders were successfully consolidated into samples for this test, the utility of the small caliber test method was demonstrated in this study.

6.3 CORROSION TEST RESULTS

6.3.1 CORROSION TESTS

As stated above, we adapted an ASTM standard for evaluation of medical implant materials (ASTM 2129) for this parametric study, investigating the corrosion behavior of the candidate materials, as well as the alloys used in the prior Fisher 344 rat studies, in a simulated physiological solution, as a method to evaluate potential toxicity as an embedded fragment.

The WHA formulations were liquid phase sintered 38 (8) alloys procured from a commercial tungsten vendor. Bulk compositions were selected to yield samples that were ~85% by volume of pure W particles, with the balance of the material consisting of a solid solution alloy matrix. For the W-Ni-Fe system, ratios of Ni to Fe were varied from 7:3 to 9:1. W-Ni-Co alloys were prepared with a 2:1 ratio of Ni to Co. For the W-Ni-Fe-Co system, alloys were produced with iron concentrations varying from half to twice that found in a commercially available alloy. An example of the typical two phase WHA microstructure is shown in Figure 35. The predominant phases in these materials are pure W particles, surrounded by a solid solution alloy matrix. These matrix alloys are nearly saturated in tungsten, and the associated matrix compositions for each alloy are listed in Table **10**. The alloy designated in this study as W-2Ni-1Co has a composition that is comparable to the 91W-6Ni-3Co alloy used in the prior implantation studies (7, 42). The W-7Ni-3Fe presented here is comparable to the 97W-2Ni-1Fe used in Roszell's study (7).

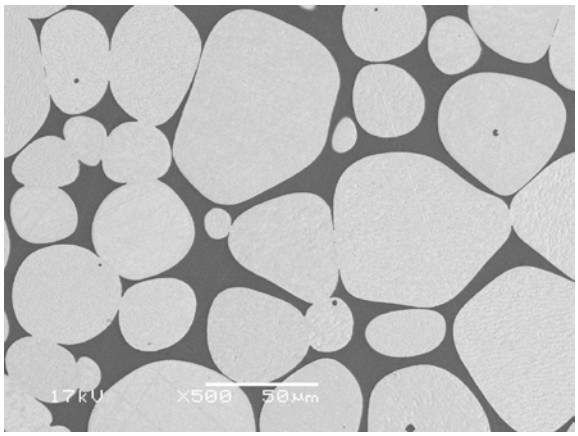

Figure 34. SEM micrograph of the typical two phase microstructure found in WHAs. The alloys were prepared to yield samples that were roughly 85% by volume of W (lighter phase). The bulk and matrix compositions (darker phase) for this study are listed in Table 10.

Table 10. Bulk and matrix compositions for all alloy formulations considered in this study.

Alloy Designations		Composition (wt %)	Matrix Composition (wt. %)
W-5Ni-2Fe-3Co	ARL-1	92.0 W-4.0 Ni-1.7 Fe-2.3 Co	34.3 W-32.7 Ni-14.0 Fe-19.0 Co
W-5Ni-4Fe-3Co	ARL-2	91.7 W-3.4 Ni-2.9 Fe-2.0 Co	28.3 W-29.5 Ni-25.2 Fe-17.1 Co
W-5Ni-1Fe-3Co	ARL-3	92.2 W-4.4 Ni-0.9 Fe-2.5 Co	37.5 W-34.8 Ni-7.4 Fe-20.2 Co
W-9Ni-1Fe	ARL-4	92.1 W-7.1 Ni-0.8 Fe	37.0 W-56.7 Ni-6.3 Fe
W-4Ni-1Fe	ARL-5	92.0 W-6.4 Ni-1.6 Fe	33.5 W-53.2 Ni-13.3 Fe
[1]W-7Ni-3Fe	ARL-6	91.8 W-7.6 Ni-2.5 Fe	30.0 W-49.0 Ni-21.0 Fe
[2]W-2Ni-1Co	ARL-9	92.4 W-5.1Ni-2.5Co	40.75 W-39.5 Ni-19.75 Co

Notes:
[1]Composition comparable to 97W-2Ni-1Fe studied by Roszell and coworkers [2].
[2]Composition comparable to 91W-6Ni-3Co from Roszell [2] and Kalinich [1].

Each alloy was cut into a cylindrical coupon 2.5mm thick and 10mm in diameter and polished with sandpaper to 1200 grit. The samples were then weighed and sonicated in 100% ethanol for five minutes, rinsed with 70% ethanol, immersed in 50% nitric acid/50% water for three minutes, rinsed with deionized water, rinsed with 70% ethanol, and then left to air dry. This final specimen preparation scheme matches that employed by Kalinich and coworkers before implantation. Prior to immersion, the initial microstructures and morphology were examined with a JEOL® 6460 Scanning Electron Microscope (SEM) and the surfaces compositions were analyzed with a Kratos Ultra X-ray Photoelectron Spectroscopy (XPS) system. The samples were then each individually placed in 125ml Nalgene bottles with 100ml of phosphate buffered saline (PBS) at a pH of 7.4. Each bottle was sealed and placed in a VWR Precision Analog Heated Water Bath from Thermo Scientific at a temperature of 37 +/- 2°C. No agitation was provided other than the heat currents from the water bath. The solutions were analyzed via Inductively Couple Plasma Optical Emission Spectrometry (ICP-OES) to find the concentration of metal ions that leached out during the experiment. New PBS solution was provided every 6 or 7 days. At the completion of the immersion tests, samples were removed from solution and rinsed with de-ionized water and 100% ethanol and then placed in a vacuum desiccator to prevent further oxidation. The corroded samples were analyzed with the SEM and with XPS to document the post-immersion surface morphology and composition.

6.3.2 RESULTS AND DISCUSSION

Figure **36** shows SEM micrographs of all WHA samples following corrosion in PBS. The associated ICP-OES measurements of the dissolved metals are displayed in Figure **37**. The relative composition of the metals in solution for days 21 to 27 are plotted in Figure **38**(a). The relative surface compositions were measured with XPS and are shown in Figure **38**(b).

W-2Ni-1Co sample showed complete loss of the matrix near the surface (Figure **36**(a)); however, the extent of dissolution through the depth has not been measured. Total concentrations of metals in solution decreased with time (Figure **37**(a)). The average of the normalized concentrations in solution (Figure **38**(a)) suggest a dissolved composition that is 41.1 wt.% W, 39.6 wt.% Ni and 19.3wt.% Co. These values are in close agreement with the matrix composition listed for W-2Ni-1Co in Table **10**. This suggests that preferential anodic dissolution of the matrix phase dominates the corrosion behavior in PBS. This mechanism is similar to that

found during *in-vivo* corrosion of 91W-6Ni-3Co (8). Corrosion of W-2Ni-1Co was associated with the highest concentrations of dissolved Ni (Figure **37**(e)). The surface composition measured by XPS was similar to that of the dissolved metals (Figure **38**(b)).

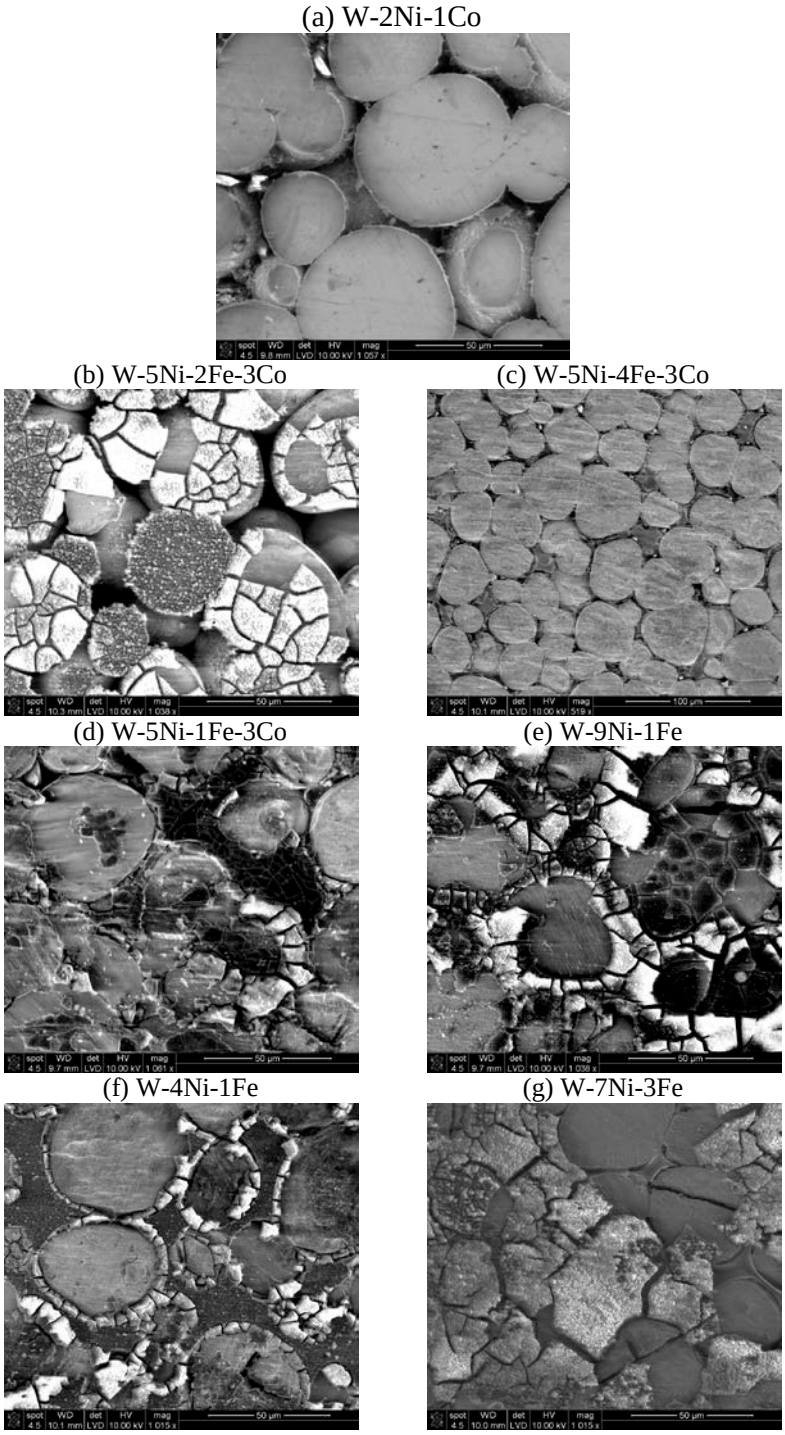

Figure 35. SEM micrographs of samples after immersion in phosphate buffered saline for 30 days.

(a)

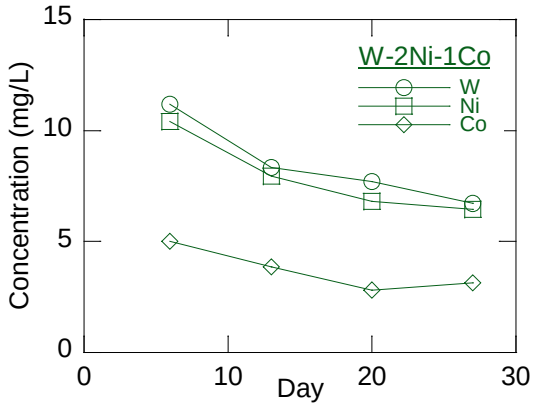
W-2Ni-1Co
W
Ni
Co
Concentration (mg/L)
Day
0
5
10
15
0
10
20
30

(b)

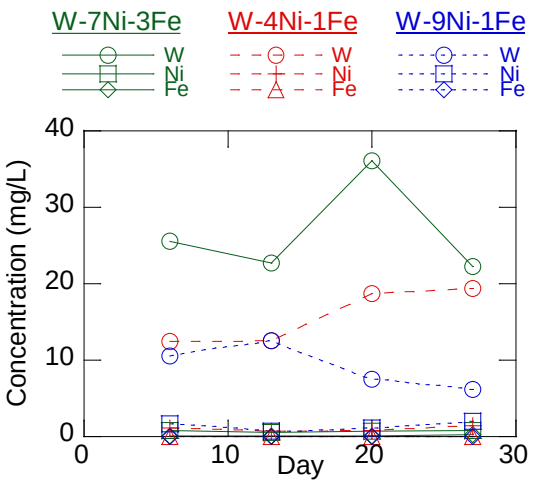
W-7Ni-3Fe
W-4Ni-1Fe
W-9Ni-1Fe
W
Ni
Fe
Concentration (mg/L)
Day
0
10
20
30
40
0
10
20
30

(c)

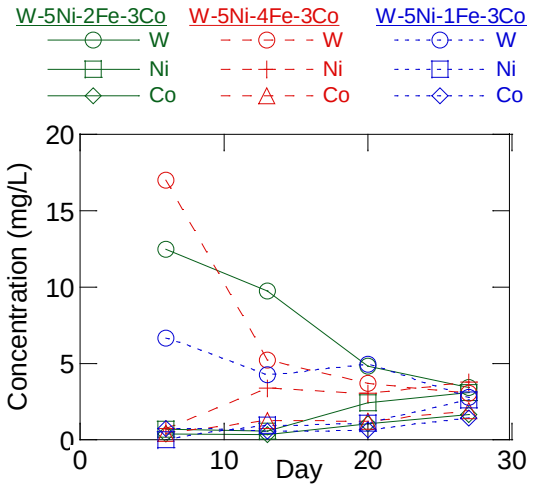
W-5Ni-2Fe-3Co
W-5Ni-4Fe-3Co
W-5Ni-1Fe-3Co
W
Ni
Co
Concentration (mg/L)
Day
0
5
10
15
20
0
10
20
30

(d)

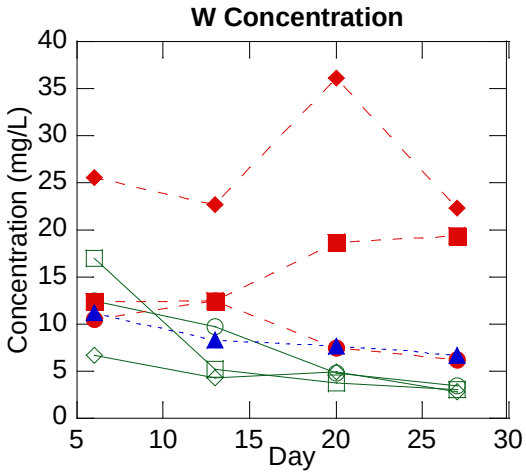
W Concentration
Concentration (mg/L)
Day
0
5
10
15
20
25
30
35
40
5
10
15
20
25
30

(e)

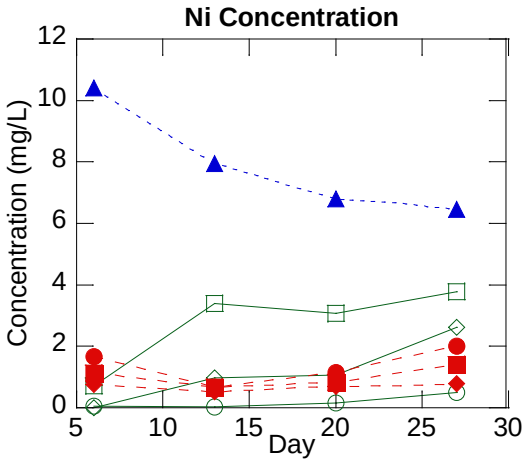
Ni Concentration
Concentration (mg/L)
Day
0
2
4
6
8
10
12
5
10
15
20
25
30

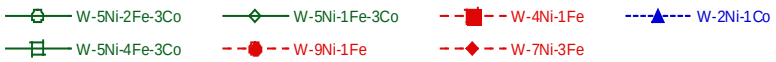

Figure 36. Summary of ICP-OES measurements of concentrations of metals dissolved in PBS for (a) W-2Ni-1Co, (b) W-Ni-Fe alloys and (c) W-Ni-Fe-Co alloys. (d) and (e) compare W and Ni concentrations for all alloys in this study.

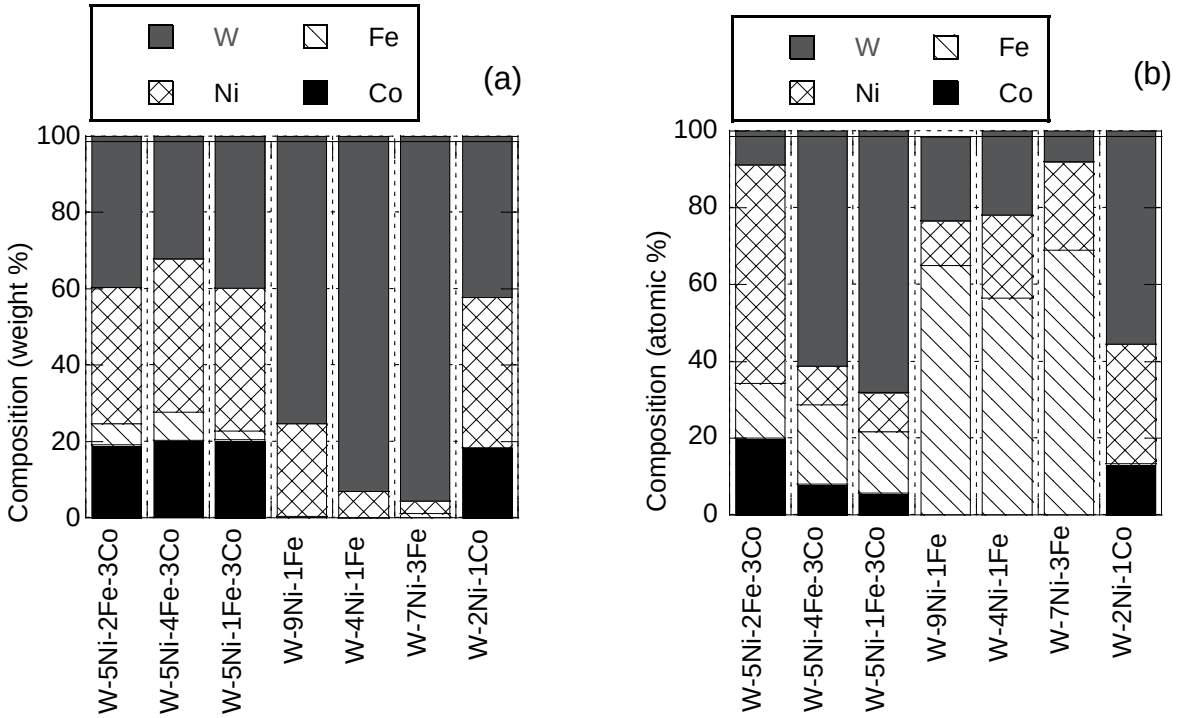

Figure 37. The relative composition of metals, (a) in solution measured for days 21-27 shown in weight %, the surface compositions of corroded samples measured by XPS expressed in atomic %.

All of the W-Ni-Fe-Co alloy samples similarly show evidence of preferential dissolution of the matrix phase (Figure **36**(b)-(d)) and the formation of an oxide layer. While the bulk W-Ni-Fe-Co alloys possess 1-3 wt% of Fe, the corroded surfaces may be as rich as ~20 at% (or 35 wt%) in Fe (graphically shown in Figure **38**(b)). ICP-OES measurements show that the initial concentrations of W in solution were higher than the Fe-free W-2Ni-1Co, though W dissolution decreased with time (Figure **37**(c)-(d)). The addition of Fe appears to have reduced the relatively leaching of Ni however there is not a clear dependence on the Fe concentration (Figure **37**(e)). The dissolved species from the W-Ni-Fe-Co alloys possess proportions of W, Ni and Co (Figure **38**(a)) that are similar to the matrix compositions listed in Table **10**. The composition of dissolved metals is however depleted in Fe relative to the matrix compositions. Concentrations of dissolved Fe are roughly 2-7% while the matrix phases possess 7-25 wt% of Fe, indicating that Fe primarily remained on the surface of the alloy rather than leaching into solution.

SEM micrographs of corroded samples of W-9Ni-1Fe, W-4Ni-1Fe, and W-7Ni-3Fe are shown in Figure **36**(e)-(g), respectively. These SEM micrographs show a dramatic change in the surface morphology. All of the corroded samples are covered in a "cracked-mud" oxide layer usually associated with a hydrated surface oxide which shrinks and cracks upon removal from solution. For W-9Ni-1Fe and W-4Ni-1Fe, there appears to be preferential growth of the oxide layer on the matrix phase rather than on the W particles. However, in other lower magnification micrographs that are not shown, the two-phase microstructure is completely obscured and covered by this oxide layer. The oxide growth appears more aggressive in for the Fe-rich WHA shown in Figure **36**(g). XPS measurements show that the corroded surfaces of the W-Ni-Fe alloys contain more than 60 at% of Fe. The ratios of Fe to W on corroded surfaces increase with Fe concentration in the alloys (Figure **38**(b)). The associated ICP-OES measurements are shown in Figure **37**(b). The highest concentrations of W in solution were associated with corrosion of W-7Ni-3Fe (Figure **37**(b) and (d)). For the W-Ni-Fe alloys, increasing the Fe concentration appears to increase the leaching of W and decrease leaching of Ni (Figure **37**(d)-(e)). The average concentration of Ni in solution was less than 0.8 mg/L for W-7Ni-3Fe and increased to as high as 2 mg/L for W-9Ni-1Fe.

There are several qualitative similarities in the corrosion behavior of WHAs *in-vivo* (8) and in PBS. Galvanic corrosion appears to hold as the predominant corrosion mechanism as has been found in other solutions and conditions (24, 36, 43-45). In PBS, there was aggressive anodic dissolution of the matrix phase in W-2Ni-1Co, as discussed above. Corrosion of Fe-bearing alloys was accompanied by the formation of an Fe-rich oxide layer on the surface. The oxide formation was most apparent in the W-Ni-Fe alloys where XPS measurements and SEM characterization indicate that the "coverage" of the oxide layer increases with increasing Fe concentration for the W-Ni-Fe alloys. In 97W-2Ni-1Fe, formation of a similar oxide layer appeared to essentially halt the operation of the galvanic cell at longer implantation times (7, 8). This oxide appears to have reduced the dissolution rate of Ni in PBS from W-Ni-Fe (compared to W-2Ni-1Co), but did not eliminate the dissolution altogether. However, these experiments have not demonstrated a clear trend in corrosion and dissolution behavior for W-Ni-Fe-Co alloys, although they also demonstrated preferential dissolution of the matrix phase, along with the formation of an Fe-oxide. All of the W-Ni-Fe-Co alloys have dissolution rates that are reduced relative to W-2Ni-1Co.

While a few general trends seem to hold for *in-vivo* and *in-vitro* corrosion of WHAs, care should be used in interpreting the results. Prior work showed that the tumor formation in rats was associated with the bioavailability of hazardous metal cations and appeared to be strongly dependent on the corrosion behavior (8). However, there are no well established threshold values for exposure to an of the alloy constituents (e.g. W, Ni, Co or Fe). The Fe-bearing alloys have lower dissolution rates of Ni, yet it is unclear how this would translate into an animal model.

One important feature from the *in-vivo* work is clearly missing from this study. Corrosion of 97W-2Ni-1Fe appeared to be associated with complete passivation of the galvanic cell during implantation times extending to nearly two years (7, 8). Roszell measured the concentration of metals in urinalysis screenings of rats taken at regular intervals and concentrations of W and Ni associated with implantation of the W-Ni-Fe alloy tended towards background levels at long

implantation times. Here, concentrations of W and Ni remain elevated at all times. Further investigations are required to determine the dependence on time, solution pH and other factors.

6.3.3 CORROSION- SUMMARY AND CONCLUSIONS

WHA alloy specimens were prepared to systematically examine the effect of Fe on the corrosion behavior in a simulated physiological solution (PBS). Corrosion of W-2Ni-1Co is associated with preferential anodic dissolution of the matrix phase, which was confirmed with SEM observations and XPS measurements. Similar examination shows a decrease in the anodic dissolution rate of the matrix phase in W-Ni-Fe alloys. With increasing Fe concentrations in W-Ni-Fe alloys, the dissolution rate of Ni is reduced, while the rate of W dissolution is increased. Corrosion of Fe-bearing alloys was accompanied by the formation of an Fe-rich oxide on the surface. The amount of oxide coverage on corroded surfaces increased with increasing Fe concentration for the W-Ni-Fe system. No clear trend for W-Ni-Fe-Co alloys was found and further investigations are required. Longer immersion times may be required to completely passivate the Fe-bearing alloys and halt dissolution of potentially hazardous metal cations in a biological environment.

7 COST ASSESSMENT

Although fluctuating with raw material costs, the manufacturing costs of conventional WHA projectiles and DU projectiles have been quite comparable through several generations of medium caliber and tank cannon munitions, as the higher processing and machining costs for DU projectiles generally compensates for its lower raw material costs. De-mil costs have not been excessively high for DU rounds as the core materials in older DU projectiles have been re-cycled for use in the latest generation projectiles. Thus to date, life-cycle costs for DU munitions have also been comparable to that of WHA munitions.

More recently however new fixed costs are now associated with DU. Production at the only DU manufacturer currently operating, Aerojet Ordnance of Jonesboro, Tennessee, has been at very low level. Until a decision is made about the penetrator material to be employed in the next generation tank round, the M829 E4, PM-MAS is incurring a cost of approximately $8M per year to keep the facility fully operational. Should the DU production end however, facility shut down costs will exceed $30M [2].

The cost estimates for conventional WHA to replace DU, and the two potential GNP-produced tungsten-based materials are listed in Table **11** below, showing projected costs for production quantities.

Table 11. Cost Model for 1 Kilogram Penetrator Blanks.

Material	Raw Materials	Pre-processing	Consolidation	Post-Process	Cost/Blank	Process Stream
Conventional. WHA	$45	$19	$10	$310	$375	Liquid-Phase Sinter
GNP Nano W	$50	$25-30	$10-15	$50-250	$135-$345	Solid State Sinter
GNP Nano W Composite	$50	$25-30	$225	$500	$800-805	HIP

The costs of the tungsten nanocomposite materials are likely to be significantly higher than conventional tungsten-nickel-iron WHAs. The costs of the nanoscale powder production by GNP, and the consolidation of the metal powders are expected to exceed that of liquid-phase sintered WHAs. The cost differential between the two depends on the specifications of the initial nanocrystalline powder and of the subsequent consolidated product. Current guidelines based on the synthesis of nanocrystalline GNP powders in 10 kg batch sizes for use in solid oxide fuel stacks suggest an increase in cost of 2 to 8 times that of conventionally processed powder. Further increases in cost will occur if a more expensive solid-state consolidation technique, such as Hot Isostatic Pressing (HIP), is required.

8 IMPLEMENTATION ISSUES

The poor ballistic performance of the last lot of pre-alloyed W-Re powders produced by the Battelle combustion synthesis process, and post-processed and consolidated at ARL, is believed to have been caused by the changes to the sintering process required to densify the pre-alloyed Battelle powders, lead to greater grain growth and larger final grain sizes in the consolidated product. Although the program is now at an end, ARL does plan to continue this work on its own in an attempt to refine the consolidation process. The superior performance of prior lots of unalloyed W nanocrystalline powders that were demonstrated, as well as superior performance of nanocrystalline heavy alloy powder materials shows that there is considerable promise for these materials.

Significant increases in the prices of commercially-available nano-crystalline W powders from China, and new restrictions on the use of these powders, have increased interest in Battelle's glycine nitrate combustion process as a US commercial process.

9 REFERENCES

1. Anonymous Kinetic Energy Penetrator Environmental and Health Considerations. Science Applications International Corporation (SAIC).
2. Anonymous Long Term KE Strategy Study. U.S. Army ARDEC: Picatinny Arsenal, NJ.
3. Daneal, M. E. (1990). *Kinetic energy penetrator long term strategy study*. ARMY ARMAMENT MUNITIONS AND CHEMICAL COMMAND ROCK ISLAND IL.
4. Magness, L. S. (2002, September). An overview of the penetration performances of tungsten and depleted uranium alloy penetrators: Ballistic performances and metallographic examinations. In *20th International Symposium on Ballistics* (Vol. 2, p. 1104).
5. Gold, K; Los, M. U.S. Army ARDEC: Picatinny Arsenal, NJ.
6. Kalinich, J. F., Emond, C. A., Dalton, T. K., Mog, S. R., Coleman, G. D., Kordell, J. E., ... & McClain, D. E. (2005). Embedded weapons-grade tungsten alloy shrapnel rapidly induces metastatic high-grade rhabdomyosarcomas in F344 rats. *Environmental Health Perspectives*, 729-734.
7. Roszell, L.E., Bazar, M.A., Beall, P.A. (2008). Assessment of the Health Effects of Tungsten and Tungsten Alloys following Implantation in Rat Muscle Tissue. *Seventh International Conference on Tungsten, Refractory and Hardmaterials*.
8. Schuster, B.E., et al. (2008). Metallographic Analysis of Tungsten and Tungsten Heavy Alloys Following Implantation in Rat Muscle Tissue. *Seventh International Conference on Tungsten, Refractory and Hardmaterials*.
9. Schuster, B.E., Ramirez, D.A., Klotz, B.R., Roszell, L.E., Murr, L.E. In-vivo Corrosion Behavior of Tungsten and Tungsten Heavy Alloys in Rat Muscle Tissue. *Corrosion Science (in preparation)*.
10. Peuster, M., Fink, C., & von Schnakenburg, C. (2003). Biocompatibility of corroding tungsten coils: in vitro assessment of degradation kinetics and cytotoxicity on human cells. *Biomaterials*, *24*(22), 4057-4061.
11. Barrett, J., Wells, I., Riordan, R., & Roobottom, C. (2000). Endovascular embolization of varicoceles: resorption of tungsten coils in the spermatic vein. *Cardiovascular and interventional radiology*, *23*(6), 457-459.
12. Butler, T. J., Jackson, R. W., Robson, J. Y., Owen, R. J., Delves, H. T., Sieniawska, C. E., & Rose, J. D. (2000). In vivo degradation of tungsten embolisation coils. *The British journal of radiology*, *73*(870), 601-603.
13. Brewer, L., Fairbrother, A., Clark, J., & Amick, D. (2003). Acute toxicity of lead, steel, and an iron-tungsten-nickel shot to mallard ducks (Anas platyrhynchos). *Journal of wildlife diseases*, *39*(3), 638-648.
14. Ringelman, J. K., Miller, M. W., & Andelt, W. F. (1993). Effects of ingested tungsten-bismuth-tin shot on captive Mallards. *The Journal of wildlife management*, 725-732.
15. Kraabel, B. J., Miller, M. W., Getzy, D. M., & Ringelman, J. K. (1996). Effects of embedded tungsten-bismuth-tin shot and steel shot on mallards (Anas platyrhynchos). *Journal of wildlife diseases*, *32*(1), 1-8.
16. Kane, M. A., Kasper, C. E., & Kalinich, J. F. (2009). Protocol for the Assessment of Potential Health Effects From Embedded Metal Fragments. *Military medicine*, *174*(3), 265-269.

17. Machado, B. I., Murr, L. E., Suro, R. M., Gaytan, S. M., Ramirez, D. A., Garza, K. M., & Schuster, B. E. (2010). Characterization and cytotoxic assessment of ballistic aerosol particulates for tungsten alloy penetrators into steel target plates. *International journal of environmental research and public health*, *7*(9), 3313-3331.
18. Chick, L. A., Pederson, L. R., Maupin, G. D., Bates, J. L., Thomas, L. E., & Exarhos, G. J. (1990). Glycine-nitrate combustion synthesis of oxide ceramic powders. *Materials Letters*, *10*(1), 6-12.
19. Jia, D., Ramesh, K. T., & Ma, E. (2003). Effects of nanocrystalline and ultrafine grain sizes on constitutive behavior and shear bands in iron. *Acta materialia*, *51*(12), 3495-3509.
20. Magness, L. S., & Farrand, T. G. (1990, May). Deformation behavior and its relationship to the penetration performance of high-density KE penetrator materials. In *Proceedings of the 1990 Army Science Conference, Durham, NC* (p. 149).
21. Rogers, H. C. (1979). Adiabatic plastic deformation. *Annual Review of Materials Science*, *9*(1), 283-311.
22. Magness, L. S., & Kapoor, D. (2000). Tungsten composite materials with alternative matrices for ballistic applications. *Tungsten, Hard Metals, and Refractory Alloys 5*, 15-23.
23. Nersisyan, H. H., Lee, J. H., & Won, C. W. (2005). A study of tungsten nanopowder formation by self-propagating high-temperature synthesis. *Combustion and flame*, *142*(3), 241-248.
24. Chang, Y. H., Wang, H. W., Chiu, C. W., Cheng, D. S., Yen, M. Y., & Chiu, H. T. (2002). Low-temperature synthesis of transition metal nanoparticles from metal complexes and organopolysilane oligomers. *Chemistry of materials*, *14*(10), 4334-4338.
25. Wei, Q., Zhang, H. T., Schuster, B. E., Ramesh, K. T., Valiev, R. Z., Kecskes, L. J., ... & Cho, K. (2006). Microstructure and mechanical properties of super-strong nanocrystalline tungsten processed by high-pressure torsion. *Acta materialia*, *54*(15), 4079-4089.
26. Magness, L.S., et al. (2001). Nanotechnology Workshop, Aberdeen Proving Ground, MD.
27. Lavender, C.A., Gurwell, W.E. (1991). Freeze-Dried Tungsten Alloy Components. *Battelle Columbus Laboratory Report*.
28. McCain, W. C., Crouse, L., Thompson, M., Ruth, A. H., Quinn, M., Bazar, M., ... & Leach, G. (2008). Acute and subacute toxicity of orally administered sodium tungstate in Sprague–Dawley rats. In *47th Annual Meeting of Society of Toxicology poster presentation*.
29. Sachdeva, S., Kushwaha, P., & Flora, S. J. S. (2013). Effects of sodium tungstate on oxidative stress enzymes in rats. *Toxicology mechanisms and methods*, *23*(7), 519-527.
30. Schuster, B. E., Roszell, L. E., Murr, L. E., Ramirez, D. A., Demaree, J. D., Klotz, B. R., ... & Bannon, D. I. (2012). In vivo corrosion, tumor outcome, and microarray gene expression for two types of muscle-implanted tungsten alloys. *Toxicology and applied pharmacology*, *265*(1), 128-138.
31. Standard, A. S. T. M. (2008). F2129-08. *Standard test method for conducting cyclic potentiodynamic polarization measurements to determine the corrosion susceptibility of small implant devices. West Conshohocken, PA: ASTM International*.

32. Harris, R. M., Williams, T. D., Hodges, N. J., & Waring, R. H. (2011). Reactive oxygen species and oxidative DNA damage mediate the cytotoxicity of tungsten–nickel–cobalt alloys *in vitro*. *Toxicology and applied pharmacology*, *250*(1), 19-28.
33. Combes, S. (2008), UK MOD Tungsten Alloys Studies and Understanding Relevant Toxic Mechanisms. *Seventh International Conference on Tungsten, Refractory and Hardmaterials*.
34. Kalinich, J. F., Miller, A. C., & McClain, D. E. (2006). *Carcinogenicity and immunotoxicity of embedded depleted uranium and heavy-metal tungsten alloy in rodents*. HENRY M JACKSON FOUNDATION FOR THE ADVANCEMENT OF MILITARY MEDICINE ROCKVILLE MD.
35. Kalinich, J. F., Vergara, V. B., & Emond, C. A. (2008). Urinary and serum metal levels as indicators of embedded tungsten alloy fragments. *Military medicine*, *173*(8), 754-758.
36. Grosso, R.J. (2008). Occupational Exposure Assessment of Aerosols Generated from Impacts of Tungsten-Based Penetrators Containing Nickel and Cobalt. (U.S. Army Research Laboratory).
37. Zook, J.A., Frank, K., Silsby, G.F. (1992). Terminal Ballistics Test and Analysis Guidelines for the Penetration Mechanics Branch; BRL-MR-3960; U.S. Army Ballistic Research Laboratory: Aberdeen Proving Ground, MD.
38. Grabarek, C., Herr, E.L. (1966). X-ray Multi-Flash System for Measurement of Projectile Performance at the Target; BRL Report No. 1634; U.S. Army Ballistic Research Laboratory: Aberdeen Proving Ground, MD.
39. Lambert, J.P., Jonas, G.H. (1976). Towards Standardization in Terminal Ballistics Testing: Velocity Representation. U.S. Army Ballistic Research Laboratory: Aberdeen Proving Ground, MD.
40. B. Butler, Private communication, 2013
41. German, R.M., *Sintering Theory and Practice*. 1996, New York: Wiley.
42. Kalinich, J.F. *Carcinogenicity of Embedded Tungsten Alloys*. in *Toxicity Risk Assessment Conference*. 2009. Cincinnati, OH.
43. Ogundipe, A., Greenberg, B., Braida, W., Christodoulatos, C., & Dermatas, D. (2006). Morphological characterisation and spectroscopic studies of the corrosion behaviour of tungsten heavy alloys. *Corrosion science*, *48*(10), 3281-3297.
44. Batten, J.J. and B.T. Moore, *Corrosion of high density sintered tungsten alloys. Part 2: Accelerated corrosion testing*. 1988, Department of Defence Materials Research Laboratory Report: Melbourne, Victoria, Australia.
45. Chang, F.C., Beatty, J.H., Kane, M.J., Beck J. (1998). Galvanic Corrosion of Tungsten Coupled With Several Metals/Alloys. U.S. Army Research Laboratory: Aberdeen Proving Ground, MD.

10 APPENDICES

A. POINTS OF CONTACT

POINT OF CONTACT Name	ORGANIZATION Name Address	Phone Fax E-mail	Role in Project
Dr. Lee Magness	Army Research Laboratory, Aberdeen, MD, 21005-5066	(410)278-6022 (410) 278-6564 lee.s.magness.civ@mail.mil	Principal Investigator
Dr. Scott Weil	Battelle Pacific NorthWest Laboratory Richland, WA 99352	(509) 375-6796 (509)-375-4448 Scott.Weil@pnl.gov	Principal Investigator
Dr. Curt Lavendar	Battelle Pacific NorthWest Laboratory Richland, WA 99352	(509)372-6770 Curt.Lavendar@pnl.gov	Principal Investigator
Dr. Brian Schuster	Army Research Laboratory, Aberdeen, MD, 21005-5066	(410)278-6733 (410) 278-6564 brian.e.schuster.civ@mail.mil	Co- Investigator (Toxicity Issues)
Dr. Rick Morgan	Global Tungsten Products Towanda, PA 18848	(570) 268-5293 (570) 268-5157 Rick.Morgan@globaltungsten.com	Industry Partner
Mr. Eric Klier	Army Research Laboratory, Aberdeen, MD, 21005-5066	(410)306-0741 (410) 306-0759 eric.klier.civ@mail.mil	Co-Investigator
Mr. Deepak Kapoor	Army Research, Development & Engineering Center, Picatinny Arsenal, Dover, NJ 07806-5000	(973)724-2596 (973)724-4351 dkapoor@pica.mil	Co-Investigator